The Astrophysical Journal Supplement Series, 256:16 (42pp), 2021 September https://doi.org/10.3847/1538-4365/ac090e

TIMES. I. A Systematic Observation in Multiple Molecular Lines toward the Orion A and Ophiuchus Clouds

Hyeong-Sik Yun[1], Jeong-Eun Lee[1], Yunhee Choi[2], Neal J. Evans, II[2,3,4], Stella S. R. Offner[3], Mark H. Heyer[5], Brandt A. L. Gaches[6,7], Yong-Hee Lee[1], Giseon Baek[1], Minho Choi[2], Hyunwoo Kang[2], Seokho Lee[8], Ken'ichi Tatematsu[9,10], Yao-Lun Yang[11], How-Huan Chen[3], Youngung Lee[2], Jaehoon Jung[2], Changhoon Lee[2], and Jungyeon Cho[12]

[1] School of Space Research, Global Campus, Kyung Hee University, 1732 Deogyeong-daero, Giheung-gu, Yongin-si, Gyeonggi-do, 17104, Republic of Korea
hs-yun@khu.ac.kr, jeongeun.lee@khu.ac.kr
[2] Korea Astronomy and Space Science Institute, 776, Daedeok-daero, Yuseong-gu, Daejeon, 34055, Republic of Korea
[3] Department of Astronomy, The University of Texas at Austin, 2515 Speedway, Austin, TX 78712, USA
[4] Humanitas College, Global Campus, Kyung Hee University, 1732 Deogyeong-daero, Giheung-gu, Yongin-si, Gyeonggi-do, 17104, Republic of Korea
[5] Department of Astronomy, University of Massachusetts Amherst, 710 N. Pleasant Street, Amherst, MA 01003, USA
[6] Physikalisches Institut, Universität zu Köln, Zülpicher Straße 77, D-50937, Köln, Germany
[7] Center of Planetary Systems Habitability, The University of Texas at Austin, 2515 Speedway, Austin, TX 78712, USA
[8] National Astronomical Observatory of Japan, 2-21-1 Osawa, Mitaka, Tokyo 181-8588, Japan
[9] Nobeyama Radio Observatory, National Astronomical Observatory of Japan, National Institutes of Natural Sciences, 462-2 Nobeyama, Minamimaki, Minamisaku, Nagano 384-1305, Japan
[10] Department of Astronomical Science, SOKENDAI (The Graduate University for Advanced Studies), 2-21-1 Osawa, Mitaka, Tokyo 181-8588, Japan
[11] Department of Astronomy, University of Virginia, Charlottesville, VA 22904-4235, USA
[12] Department of Astronomy and Space Science, Chungnam National University, 99 Daehak-ro, Yuseong-gu, Daejeon, 34134, Republic of Korea
Received 2021 February 28; revised 2021 May 20; accepted 2021 June 6; published 2021 September 7

Abstract

We have used the Taeduk Radio Astronomy Observatory to observe the Orion A and Ophiuchus clouds in the $J = 1-0$ lines of ^{13}CO, C^{18}O, HCN, HCO$^+$, and N_2H^+ and the $J = 2-1$ line of CS. The fully sampled maps with uniform noise levels are used to create moment maps. The variations of the line intensity and velocity dispersion with total column density, derived from dust emission maps, are presented and compared to previous work. The CS line traces dust column density over more than one order of magnitude, and the N_2H^+ line best traces the highest column density regime ($\log(N_{H_2}) > 22.8$). Line luminosities, integrated over the cloud, are compared to those seen in other galaxies. The HCO$^+$-to-HCN luminosity ratio in the Orion A cloud is similar to that of starburst galaxies, while that in the Ophiuchus cloud is in between those of active galactic nuclei and starburst galaxies.

Unified Astronomy Thesaurus concepts: Molecular clouds (1072)

1. Introduction

Gas motion in molecular clouds (MCs) is generally turbulent (Larson 1981; Elmegreen & Scalo 2004; Heyer & Brunt 2004). Supersonic turbulence on a large scale acts as an internal pressure against the global gravitational collapse and also produces dense clumps in small scales via shocks (Evans 1999; Padoan et al. 1999, 2001; Mac Low & Klessen 2004). As turbulence dissipates, star formation becomes easier in the clumps (Padoan et al. 2001; Bergin & Tafalla 2007). Thus, turbulence plays a critical role in the evolution of clouds and star-forming regions, and understanding the properties of turbulence is key to understanding its role in star formation, especially for the earliest phase (Bergin & Tafalla 2007). However, the relation between the turbulence and star formation is still controversial.

To obtain the properties of turbulence in MCs, $J = 1-0$ transitions of ^{12}CO and ^{13}CO have been used (Heyer & Brunt 2004; Padoan et al. 2006, 2009; Brunt et al. 2009; Koch et al. 2017) because these transitions can easily trace molecular gas in the interstellar medium. However, these lines become optically thick toward the high column density regions and cannot trace the turbulent motions in a dense environment. The properties of turbulence derived from these optically thick lines might be ineffective for assessing the relation between turbulence and star formation since stars are generally formed in a dense environment. Recent surveys, such as the CARMA Large Area Star Formation Survey (CLASSy; Storm et al. 2014) and the Green Bank Ammonia Survey (GAS; Friesen et al. 2017; Monsch et al. 2018), used optically thin lines and found that the turbulence affects the formation of the kinematical and morphological structures of dense gas (Storm et al. 2014, 2016; Kirk et al. 2017; Chen et al. 2019). However, the CLASSy survey observed small areas limited to clump scale (about 1 pc × 1 pc). The small map size would limit the spatial size of turbulent motion that we can investigate, and the supersonic turbulent motion in large scales would not be probed. The GAS survey, using the NH_3 lines, is only focused on cold and dense gas.

To investigate the gas motions in various densities and spatial scales, it is necessary to map the entire MC in different molecular lines that can trace various density environments. Gaches et al. (2015) simulated a star-forming MC using a hydrodynamic simulation with post-processed three-dimensional photodissociation astrochemistry. They categorized molecular transitions into three groups (*diffuse*, *intermediate*, and *dense* tracers) that trace different density environments. Therefore, the spectral maps in different molecular transitions would represent the turbulent motions in different density environments if we chose the transitions from these three groups (Goodman et al. 1998). This systematic study of MCs can also provide detailed initial properties and constraints for the simulation of turbulent star-forming clouds.

To compare the properties of turbulence in different star-forming environments, we should observe MCs that have different

star-forming environments. The Orion A cloud can be divided into three regions: the integral-shaped filament (ISF), L1641, and L1647 from the north to the south (Lynds 1962; Meingast et al. 2016). Among these regions, the ISF encompasses active massive star-forming regions (Ikeda et al. 2007; Megeath et al. 2012; Furlan et al. 2016), and the other regions include low-mass star-forming regions (Allen & Davis 2008; Megeath et al. 2012; Nakamura et al. 2012; Furlan et al. 2016). In the Ophiuchus cloud, low-mass stars are actively forming in L1688 (Motte et al. 1998; Wilking et al. 2008; Zhang & Wang 2009; Dunham et al. 2015). In this region, many dense cores (Oph-A through L) have been identified using DCO^+ (Loren et al. 1990), N_2H^+ (Pan et al. 2017), and millimeter continuum observations (Johnstone et al. 2004; Pattle et al. 2015). Some of these cores and their substructures were identified as "droplets," which are the pressure-confined coherent cores (Chen et al. 2019, 2020). Also, a filamentary structure that stretches from L1688 to the northeast, L1709, contains one starless core and one protostellar core (Loren et al. 1990; Dunham et al. 2015; Pattle et al. 2015). The star formation in L1709 is less efficient than that in L1688 (Pattle et al. 2015). Because of their various star-forming environments and proximity (389−443 pc and 137 pc for the Orion A and Ophiuchus clouds, respectively; Ortiz-León et al. 2017; Kounkel et al. 2018), these clouds are ideal targets to compare the properties of the turbulence in the different star-forming environments.

The Orion A cloud has been mapped in various lines, including $J = 1-0$ of ^{13}CO (Bally et al. 1987; Tatematsu et al. 1993; Nagahama et al. 1998; Ripple et al. 2013; Shimajiri et al. 2014; Kong et al. 2018), $C^{18}O$ (Shimajiri et al. 2011; Kong et al. 2018), and N_2H^+ (Tatematsu et al. 2008; Nakamura et al. 2019). The Ophiuchus cloud has been mapped in the $J = 1-0$ line of ^{13}CO (Loren 1989a; Ridge et al. 2006), HCN (Shimajiri et al. 2017), HCO^+ (Shimajiri et al. 2017), and N_2H^+ (Pan et al. 2017). However, most of the observations focused on the northern part of Orion A (the ISF and L1641-N; Tatematsu et al. 1993; Shimajiri et al. 2014; Kong et al. 2018) or L1688 in Ophiuchus (Pan et al. 2017; Shimajiri et al. 2017), which are the most active star-forming regions in each cloud. In addition, there are maps of the entire MCs, but these were done with larger beams and/or fewer transitions (Bally et al. 1987; Loren 1989a; Nagahama et al. 1998).

We performed a systematic observation toward the Orion A and Ophiuchus clouds in multiple molecular lines using the Taeduk Radio Astronomy Observatory (TRAO; Roh & Jung 1999; Jeong et al. 2019) 13.7 m telescope. All spectral maps were obtained by the TRAO Key Science Program (KSP) "mapping Turbulent properties In star-forming MolEcular clouds down to the Sonic scale" (TIMES; PI: Jeong-Eun Lee). Our program aims to obtain spectral maps of the entire Orion A and Ophiuchus clouds in multiple molecular lines in order to investigate the properties of turbulence in MCs that have different star-forming environments. This is the first observational study in multiple molecular lines that can trace various density environments (Gaches et al. 2015) toward the entire area of the target clouds with a consistent observational scheme, high velocity resolution, and high sensitivity. We especially designed our observations to achieve uniform noise levels throughout the maps in order to calculate turbulence statistics.

This first paper presents our observations and simple analyses. Further analysis of the turbulence in the clouds will be presented in the second paper. We describe the details of the observation program in Section 2. In Section 3, the method to produce moment 0, 1, and 2 maps with a high signal-to-noise ratio is described. We assess the uniformity of the data quality and morphological/kinematical features of the observed clouds in Section 4, where we also compare the integrated intensities of the observed lines with column densities derived from the dust continuum. Section 5 discusses the physical properties of the line-emitting gas in both clouds, and Section 6 presents a summary.

2. Observations

2.1. The TRAO 13.7 m Telescope

We obtained six molecular line maps toward each cloud using the 13.7 m radio telescope at TRAO in Daejeon, South Korea. The SEQUOIA-TRAO receiver, which has 16 pixels arranged in a 4×4 array, can obtain two molecular lines at 85−100 GHz or 100−115 GHz simultaneously. TRAO also provides the on-the-fly (OTF) observing mode, so that the combination of the simultaneous observation of two lines and the OTF mode with the multibeam receiver makes the TRAO telescope an excellent facility to map multiple molecular transitions toward a large area efficiently.

The back end is an FFT2G spectrometer that can accept the 32 IF outputs from SEQUOIA-TRAO. The FFT2G spectrometer has a bandwidth of 62.5 MHz with 4096 channels. Thus, its spectral resolution is about 15 kHz, corresponding to a velocity resolution of about 0.04 km s^{-1} at 110 GHz. The main beam of the TRAO telescope has an almost circular pattern with a beam size of about 57″ and 49″ at 86 and 110 GHz, respectively (Jeong et al. 2019).

2.2. Mapping the Orion A and Ophiuchus Clouds

The Orion A and Ophiuchus clouds were divided into multiple $20' \times 20'$ areas (submaps). The OTF mapping was performed toward each submap, along with the R.A. and decl. directions. Each OTF datum possibly contains a *scanning noise* (Emerson & Graeve 1988). The *scanning noise* is manifested by noise features along the scanning direction that originate from the variation of weather conditions during the scanning process. We minimize these noise features by combining the OTF maps in R.A. and decl. directions and achieve a uniform noise distribution on the covered area. The observed submaps were combined to build the spectral maps for the entire clouds. During the observation, the pointing uncertainty is less than 10″. The system noise temperature ranges from 250 to 400 K at 110 GHz and varies depending on the weather conditions and elevation of the clouds.

Both clouds were mapped in six molecular lines that can trace the diffuse to dense gas in MCs: ^{13}CO $J = 1-0$, $C^{18}O$ $J = 1-0$, HCN $J = 1-0$, HCO^+ $J = 1-0$, N_2H^+ $J = 1-0$, and CS $J = 2-1$. Two of these lines were observed together; each of the $^{13}CO/C^{18}O$, HCN/HCO^+, and N_2H^+/CS line pairs was simultaneously observed. Table 1 shows the line frequency, velocity resolution (ΔV), critical density (n_{crit}), and main-beam efficiency for each observed line. Note that the main-beam efficiencies are obtained by interpolation of the efficiencies measured by Jeong et al. (2019). All spectral maps were observed from 2016 January to 2019 April.

The observed areas toward the Orion A and Ophiuchus clouds are presented in Figure 1. The $^{13}CO/C^{18}O$ and

Table 1
Properties of the Observation in Each Line

Line	Rest Frequency (GHz)	Velocity Resolution (km s^{-1})	Beam Size[b] (arcsec)	n_{crit}[a] (cm^{-3})	Beam Efficiency[b] (%)
^{13}CO $J=1-0$	110.201	0.0838	49.0	1×10^{3}	46 ± 2
C^{18}O $J=1-0$	109.782	0.0833	49.1	1×10^{3}	46 ± 2
HCN $J=1-0$	88.631	0.1032	56.0	2×10^{6}	45 ± 3
HCO^{+} $J=1-0$	89.188	0.1026	55.7	3×10^{5}	46 ± 3
N_2H^{+} $J=1-0$	93.173	0.0982	54.1	2×10^{5}	47 ± 2
CS $J=2-1$	97.980	0.0934	52.0	3×10^{5}	48 ± 2

Notes.
[a] Critical densities for observed lines; from Ungerechts et al. (1997).
[b] Beam sizes and efficiencies for the observed lines are derived using a linear interpolation method based on those provided by Jeong et al. (2019).

HCN/HCO^{+} lines were mapped within the same area through the entire clouds. We obtained the visual extinction (A_V) maps provided by Dobashi (2011) and selected initially the submaps, which have A_V higher than a certain value. We adopted A_V of 2.0 and 4.0 for the Orion A and Ophiuchus clouds, respectively, which reasonably outline the structures of the clouds. The OTF observation was initially performed toward the selected submaps, and subsequently we extended the observation if the ^{13}CO line had been significantly detected on the boundary of the observed area. Total mapped areas in the ^{13}CO/C^{18}O and HCN/HCO^{+} lines are ~8.7 and ~3.9 deg^2 of the Orion A and Ophiuchus clouds, respectively. For the N_2H^{+}/CS lines, observations were made toward the submaps where the observed C^{18}O map exhibits clump-like structures. The mapped areas are ~4.0 and ~1.6 deg^2 in the Orion A and Ophiuchus clouds, respectively. We observed the N_2H^{+}/CS lines deeper than the other lines because of their weak line intensities. Moreover, we chose representative star-forming regions for each cloud: the selected regions are the ISF and L1641-N cluster in the Orion A cloud and the L1688 region in the Ophiuchus cloud. For these regions, we observed the N_2H^{+}/CS lines even deeper to obtain high-sensitivity spectral maps. The boundaries of the mapped areas are marked in Figure 1. The total observed time to obtain all data was about 1672 hr: 1097 hr for the Orion A cloud and 575 hr for the Ophiuchus cloud.

The obtained maps were processed using the OTFTOOL and GILDAS/CLASS[13] programs with a cell size of 20″ and ΔV of about 0.1 km s^{-1}. Baselines were removed using a least χ^2 fitting method with a first-order polynomial. The baseline fitting is performed for the line-free spectra in the velocity ranges that are outside of the velocity windows (V_{win}). To obtain good baseline, regions in velocity space (V_{space}) that are almost three times broader than V_{win} are used. Some of the observed lines show broad wing structures toward OMC-1, where the energetic outflowing source Orion KL is located (see Section 4.2.1). For these line spectra, we applied velocity windows broader than V_{win} of the other locations in the cloud. The V_{win} and V_{space} values for each spectral map are listed in Table 2.

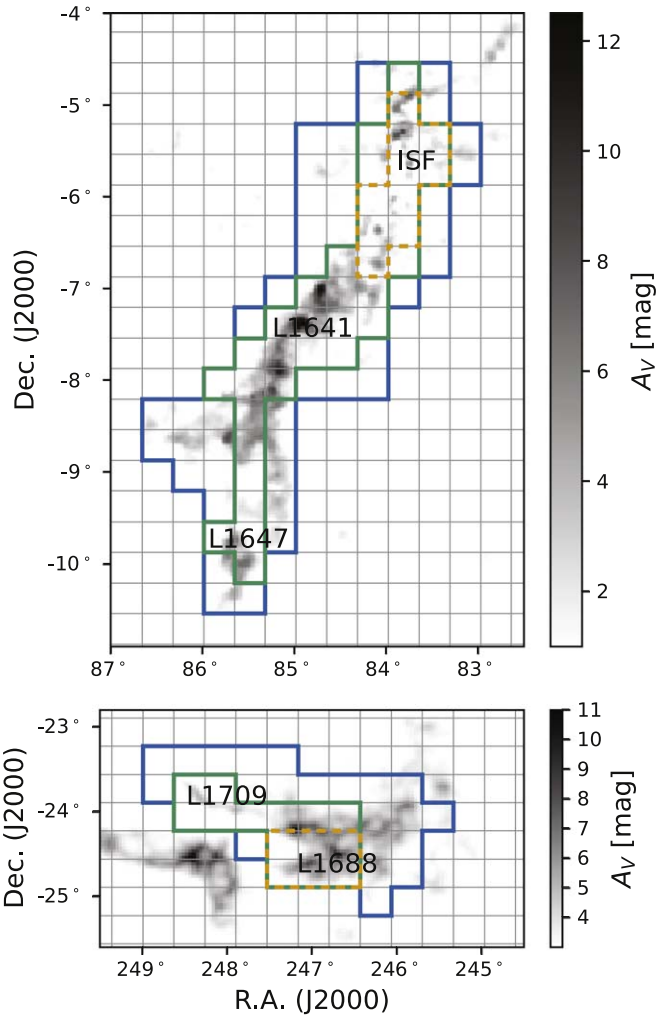

Figure 1. Visual extinction map of the Orion A (top) and Ophiuchus (bottom) clouds provided by Dobashi (2011) overlaid with outlines showing 20′ × 20′ submaps (gray vertical and horizontal lines). The mapped area in ^{13}CO $J=1-0$, C^{18}O $J=1-0$, HCN $J=1-0$, and HCO^{+} $J=1-0$ is presented by the blue solid line. The green solid line shows the area where N_2H^{+} $J=1-0$ and CS $J=2-1$ are mapped. For the active star-forming regions, such as ISF, L1641-N cluster (in the Orion A cloud), and L1688 (in the Ophiuchus cloud), outlined with the orange dotted lines, the N_2H^{+} and CS lines are mapped more deeply.

3. Moment Maps with a Moment-masking Method

We produced the moment 0, 1, and 2 maps for the observed lines, which are equivalent to the maps of integrated intensity (I_{tot}), intensity weighted mean velocity (V_{lsr}), and velocity dispersion (σ_V). In this process, the moment-masking method (Dame 2011) is applied. The moment-masking method is an efficient way to avoid the noise effect, which degrades the signal-to-noise ratio of the moment maps. This method

[13] http://www.iram.fr/IRAMFR/GILDAS

Table 2
Parameters for Data Reduction

Line	V_{win} (km s^{-1})	V_{space} (km s^{-1})
Orion A		
^{13}CO	(0, 20)	(−20, 40)
C^{18}O	(0, 20)	(−20, 40)
HCN	(−10, 30)	(−50, 70)
HCO$^+$	(−5, 25)	(−35, 55)
N_2H^+	(−5, 22)	(−18, 35)
CS	(−5, 17)	(−20, 40)
Ophiuchus		
^{13}CO	(−1, 8)	(−7, 14)
C^{18}O	(−1, 8)	(−10, 17)
HCN	(−8, 13)	(−29, 34)
HCO$^+$	(−1, 8)	(−10, 17)
N_2H^+	(−10, 15)	(−35, 40)
CS	(−1, 8)	(−10, 17)
Near Orion KL[a]		
^{13}CO	(−13, 30)	
C^{18}O	(−5, 25)	
HCN	(−30, 50)	
HCO$^+$	(−20, 40)	
CS	(−15, 38)	

Note.
[a] Velocity windows (V_{win}) for the line spectra with broad wing structures. Velocity spaces (V_{space}) for these lines are the same as that of the Orion A cloud.

identifies emission-free pixels from the smoothed data and removes noise signals within the spectral cube data. The I_{tot} maps of the ^{13}CO line in the Orion A and Ophiuchus clouds are presented in Figures 2 and 3, respectively. The V_{lsr} and σ_V maps for the ^{13}CO line of the Orion A cloud are presented in Figures 4 and 5, while those for the Ophiuchus cloud are presented in Figures 6 and 7, respectively. The other moment maps for the Orion A cloud are exhibited in Appendix A, and those for the Ophiuchus cloud are exhibited in Appendix B.

We also calculated the uncertainties of the I_{tot}, V_{lsr}, and σ_V values (ϵ_{mom0}, ϵ_{mom1}, and ϵ_{mom2}, respectively). The uncertainties were derived via the noise propagation. We measured T_{rms} from the line-free spectra of the regions outside V_{win} and adopted it as an uncertainty of the line intensity. The ϵ_{mom0}, ϵ_{mom1}, and ϵ_{mom2} values are generally dominated by T_{rms} and the number of channels that are included in calculation. The contributions of the velocity uncertainty are minor compared to the other contributions.

For the HCN and N_2H^+ lines that have multiple hyperfine transitions, we consider a single transition line to derive the V_{lsr} and σ_V correctly. For the HCN line, we adopted the strongest line at 88.631 GHz. We initially assumed that V_{lsr} of the 88.631 GHz line is the same as that of the CS line (V_{lsr}^{CS}). The moment values are derived from the velocity range between $V_{lsr}^{CS} - 4$ and $V_{lsr}^{CS} + 3$ km s^{-1}, which separate the hyperfine transitions of HCN. The hyperfine transitions of the HCN line are generally blended in the ISF; therefore, σ_V in the ISF region would be underestimated. For the N_2H^+ line, we adopted an isolated transition at 93.176 GHz and derived the moment values from $V_{lsr}^{CS} - 10.87$ to $V_{lsr}^{CS} + 4.87$ km s^{-1}. Finally, we added 7.87 km s^{-1}, which is the velocity difference between the rest frequency and the isolated hyperfine transition, to the derived V_{lsr}.

4. Results

4.1. Homogeneous Data Quality

One way to obtain the properties of turbulence from spectral cube data is by statistical analyses, such as the probability distribution functions (pdfs), two- or three-dimensional power spectra, and a wavelet transform of density or velocity fields (Gill & Henriksen 1990; Klessen 2000; Ossenkopf & Mac Low 2002; Kowal et al. 2007; Burkhart et al. 2009; Koch et al. 2017). For some of these statistical analyses, it is quite important to have well-characterized uncertainties, so we focus here on the data uniformity.

Figure 8 displays the pdfs of T_{rms}. The T_{rms} pdfs for each of the ^{13}CO, C^{18}O, HCN, and HCO$^+$ lines have a well-defined single Gaussian-like distribution. The mean and standard deviation of T_{rms} are given in Figure 8. For the N_2H^+ and CS lines, the T_{rms} pdfs of the N_2H^+ and CS lines have a pair of Gaussian-like components because of the high-sensitivity maps toward the selected star-forming regions. The filled histograms in the bottom panel are the pdfs for the high-sensitivity maps. The mean T_{rms} values for the N_2H^+ and CS lines range from 0.10 to 0.11 K, and their standard deviations are less than 0.025 K. For the selected star-forming regions, the mean and standard deviation of T_{rms} are ∼0.09 and 0.006 K, respectively.

These small standard deviation values imply a homogeneous T_{rms} in the spectral maps. The ^{13}CO, C^{18}O, HCN, and HCO$^+$ data have similar mean T_{rms} values, and each of them has a uniform T_{rms} distribution across the observed area. Also, the pdfs of T_{rms} for the N_2H^+ and CS data imply that T_{rms} does not significantly vary within each of the selected star-forming regions and the other areas.

4.2. The Morphological and Kinematical Features of the Clouds

4.2.1. The Orion A Cloud

In the Orion A cloud, spatial distributions of the observed lines are generally well correlated. All the lines follow a filamentary structure extending from the north to the south (from ISF to L1647-S). The I_{tot} in all lines are generally strong in the ISF (decl. $> -6.^\circ2$). Otherwise, all the lines in the southern filamentary structure are weaker than those in the ISF. Also the HCN, HCO$^+$, N_2H^+, and CS lines are not detected in the L1647 region (decl. $< -9^\circ$; see Figure 2, where these various regions are identified).

The observed lines reveal various structures within the Orion A cloud. The C^{18}O, HCN, HCO$^+$, N_2H^+, and CS lines are detected toward the regions where the I_{tot} of ^{13}CO is strong. Among these lines, the C^{18}O and N_2H^+ lines show clumpy structures, while the CS line shows relatively extended structures across the Orion A cloud. The HCN and HCO$^+$ lines reveal extended filamentary structures in the ISF, while they reveal clumpy structures in the other regions.

The spatial distributions of the C^{18}O, HCN, HCO$^+$, N_2H^+, and CS lines are well correlated with those of young embedded protostars (Class 0/I young stellar objects (YSOs) and flat-spectrum sources) identified using Spitzer (Megeath et al. 2012) and Herschel observations (Furlan et al. 2016). Especially, the C^{18}O line presents a tight correlation between the spatial distribution of I_{tot} and the embedded protostars (Figure 9). Also, the HCN, HCO$^+$, and CS lines exhibit a similar spatial distribution (Figures A2, A3, and A5). These

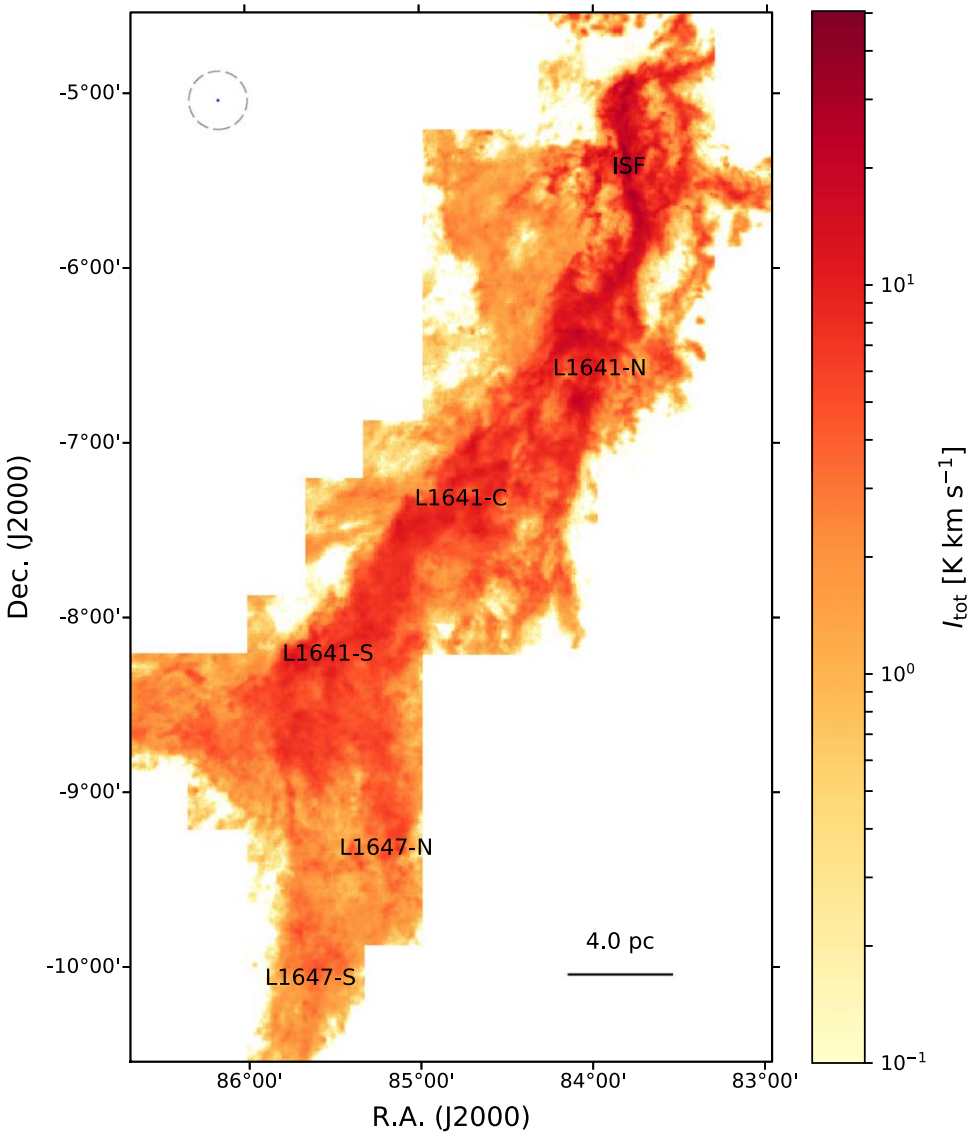

Figure 2. The moment 0 (the equivalent of integrated intensity; I_{tot}) map of the ^{13}CO line toward the Orion A cloud. The blue circle in the gray dashed circle in the upper left corner indicates the beam size of the TRAO telescope at 110 GHz. We annotated the ^{13}CO maps with the names of the subregions (Lynds 1962; Meingast et al. 2016; Großschedl et al. 2018).

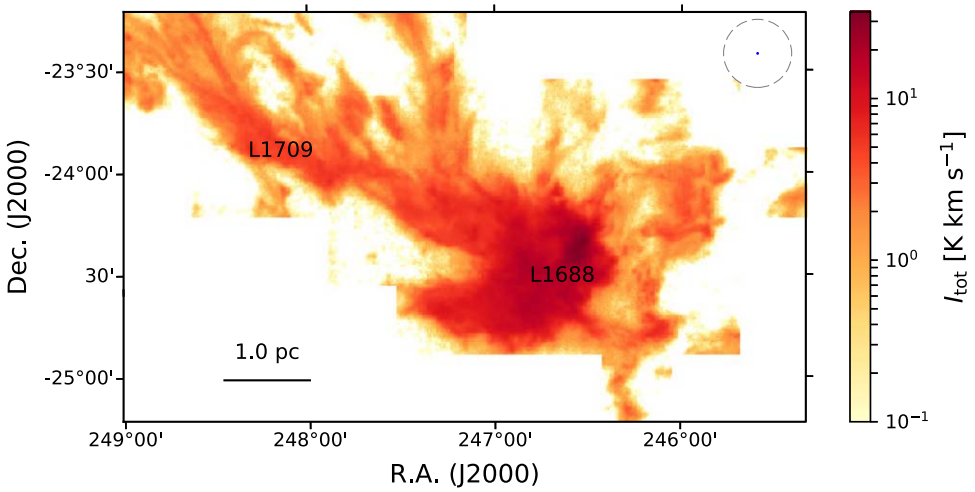

Figure 3. Same as Figure 2, but for the Ophiuchus cloud. The beam size is shown in the upper right corner of the map. The map is annotated with the names of the subregions (Lynds 1962; Loren 1989a).

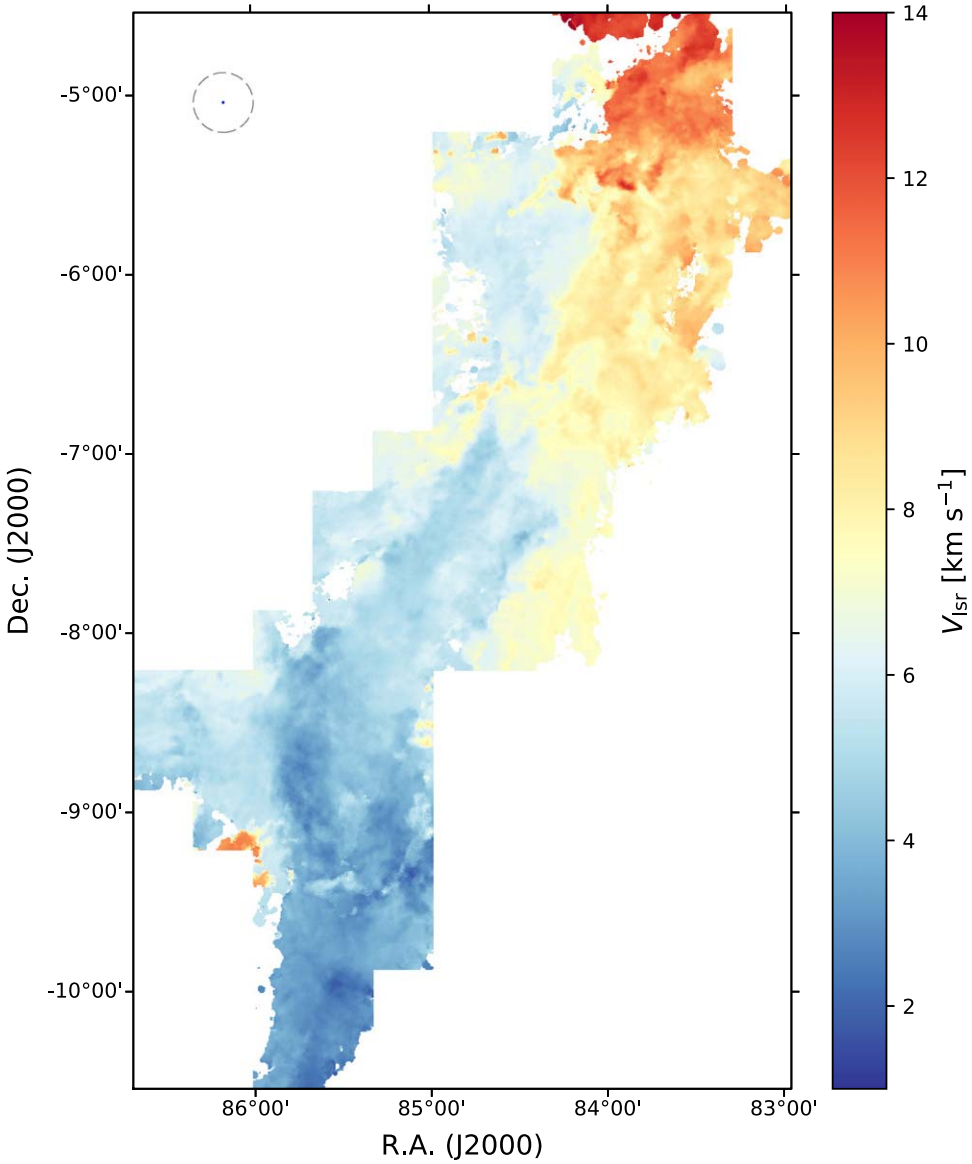

Figure 4. The moment 1 (the equivalent of mean line-of-sight velocity; V_{lsr}) map for the ^{13}CO line in the Orion A cloud.

lines are mainly found in the active star-forming regions (ISF and star-forming clusters) and Herbig-Haro (HH) objects (HH 1, HH 2, and HH 43).

Figures 4 and 5 present the V_{lsr} and σ_V maps of the ^{13}CO line in the Orion A cloud. The V_{lsr} map of the Orion A cloud exhibits a global velocity gradient from the north to the south (Heyer et al. 1992; Tatematsu et al. 1993; Ikeda et al. 2007; Shimajiri et al. 2011; Kong et al. 2018). This global velocity gradient seems to be the motion of the overall Orion A cloud and could represent large-scale rotation (Bally et al. 1987), expansion (Kutner et al. 1977; Maddalena et al. 1986), or gravitational collapse (Hartmann & Burkert 2007). Statistical analyses without considering the overall motion of MC can cause misunderstanding of turbulence. Therefore, we should take the motion of the Orion A cloud into account when investigating the properties of turbulence in future studies. The σ_V ranges from 0.2 to 2.0 km s^{-1} throughout the Orion A cloud, except for some regions with high-σ_V values. These regions are located in the eastern part of ISF and the L1647-N region. In these regions, there are multiple cloud components with different V_{lsr}. We will discuss these high-σ_V regions in Appendix C.

Another notable feature is a broad wing structure in the observed lines toward OMC-1 (Kuiper et al. 1980; Rydbeck et al. 1981; Olofsson et al. 1982; Hasegawa et al. 1984). The ^{13}CO, HCN, HCO$^+$, and CS lines present the blue- and redshifted broad wing structures (see Figure 10). For the HCN, HCO$^+$, and CS lines, the broad wing structures result in very high I_{tot} values: the I_{tot} toward OMC-1 are 241, 71, and 51 K km s^{-1} in the HCN, HCO$^+$, and CS lines, respectively. The σ_V values for the HCO$^+$ and CS lines are also high near OMC-1, while the σ_V value for the HCN line is not significantly high because of the limited velocity range that we adopted.

The C^{18}O and N_2H^+ lines do not present clear wing structures in their spectra toward OMC-1. We compared the integrated intensities of the central peak (I_{center}) and the broad wing structures (I_{wing}) to check whether or not the weak broad structures exist in the C^{18}O and N_2H^+ lines. The velocity ranges that I_{center} and I_{wing} are derived over are summarized in Table 3. The observed lines generally peak at the velocity of 9 km s^{-1}. We

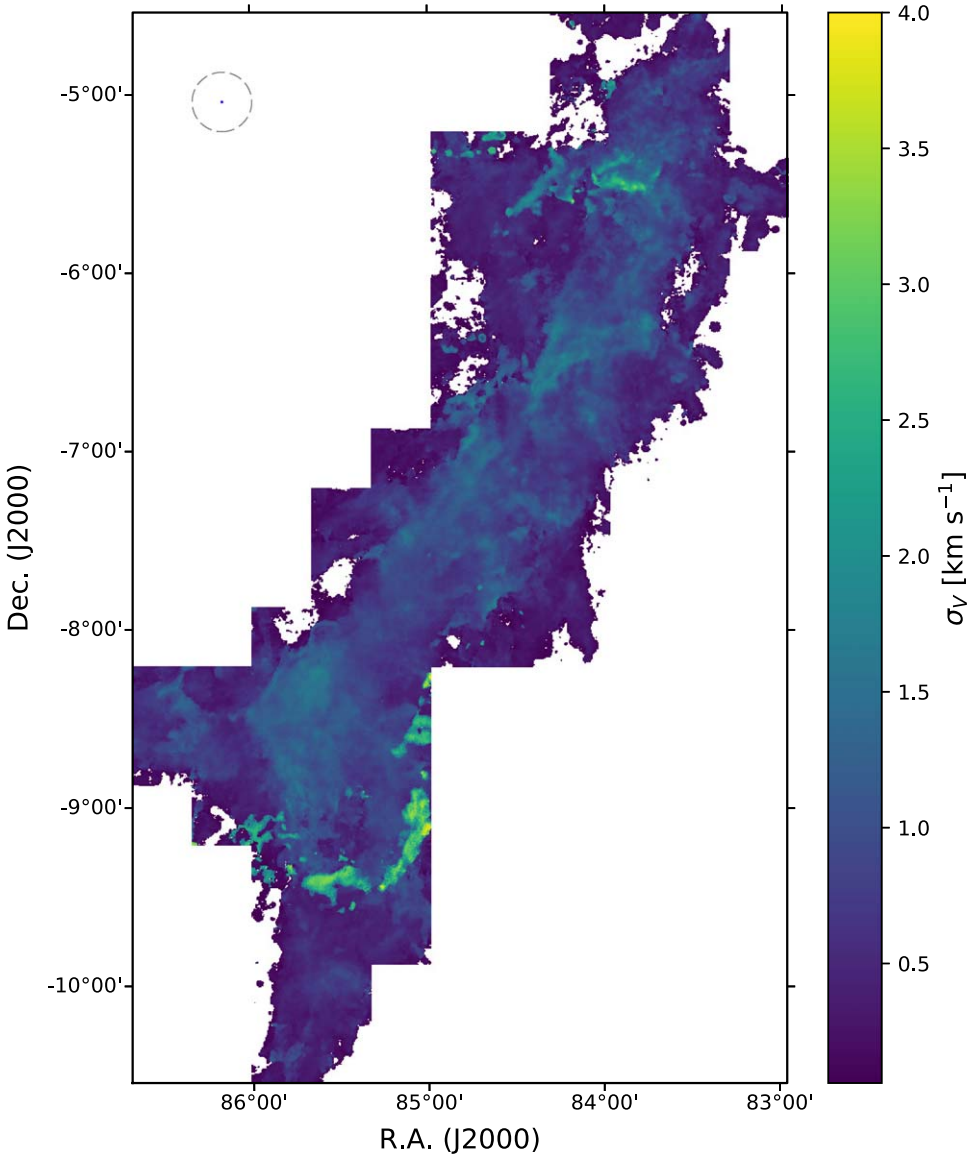

Figure 5. The moment 2 (the equivalent of velocity dispersion; σ_V) map for the ^{13}CO line in the Orion A cloud.

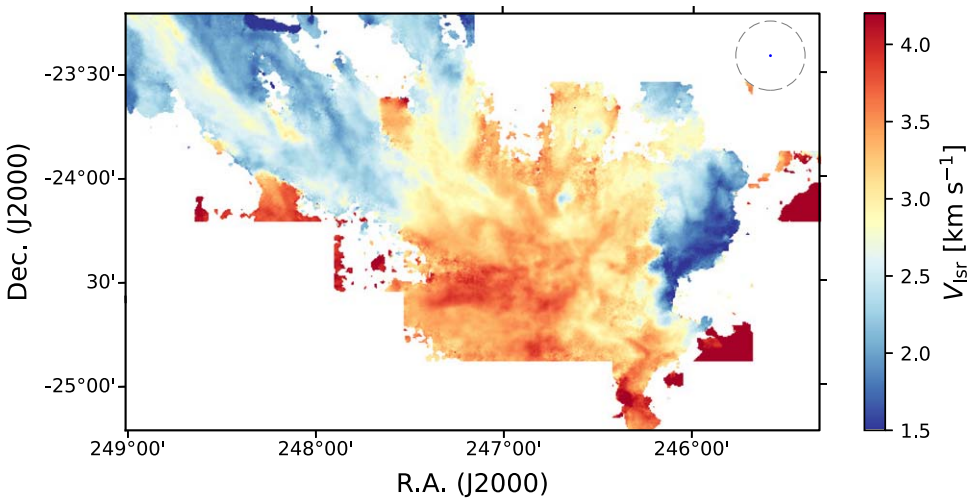

Figure 6. Same as Figure 4, but for the Ophiuchus cloud.

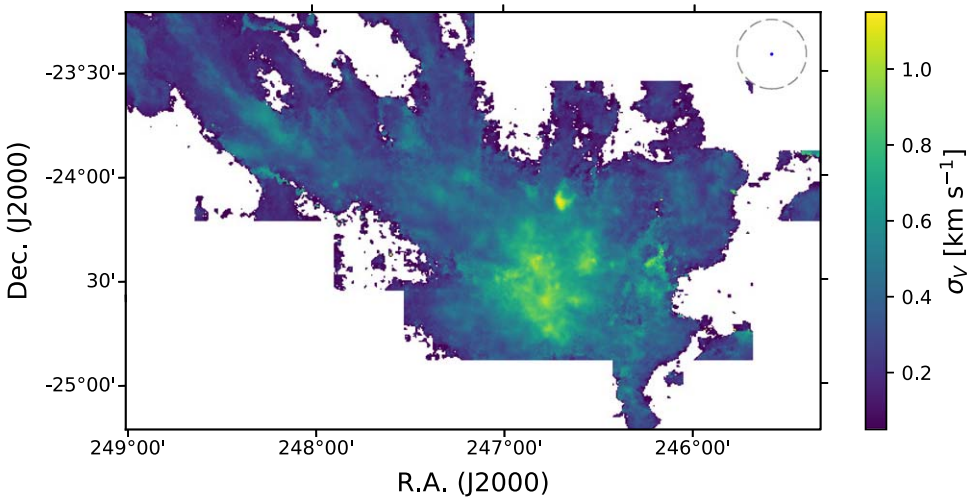

Figure 7. Same as Figure 5, but for the Ophiuchus cloud.

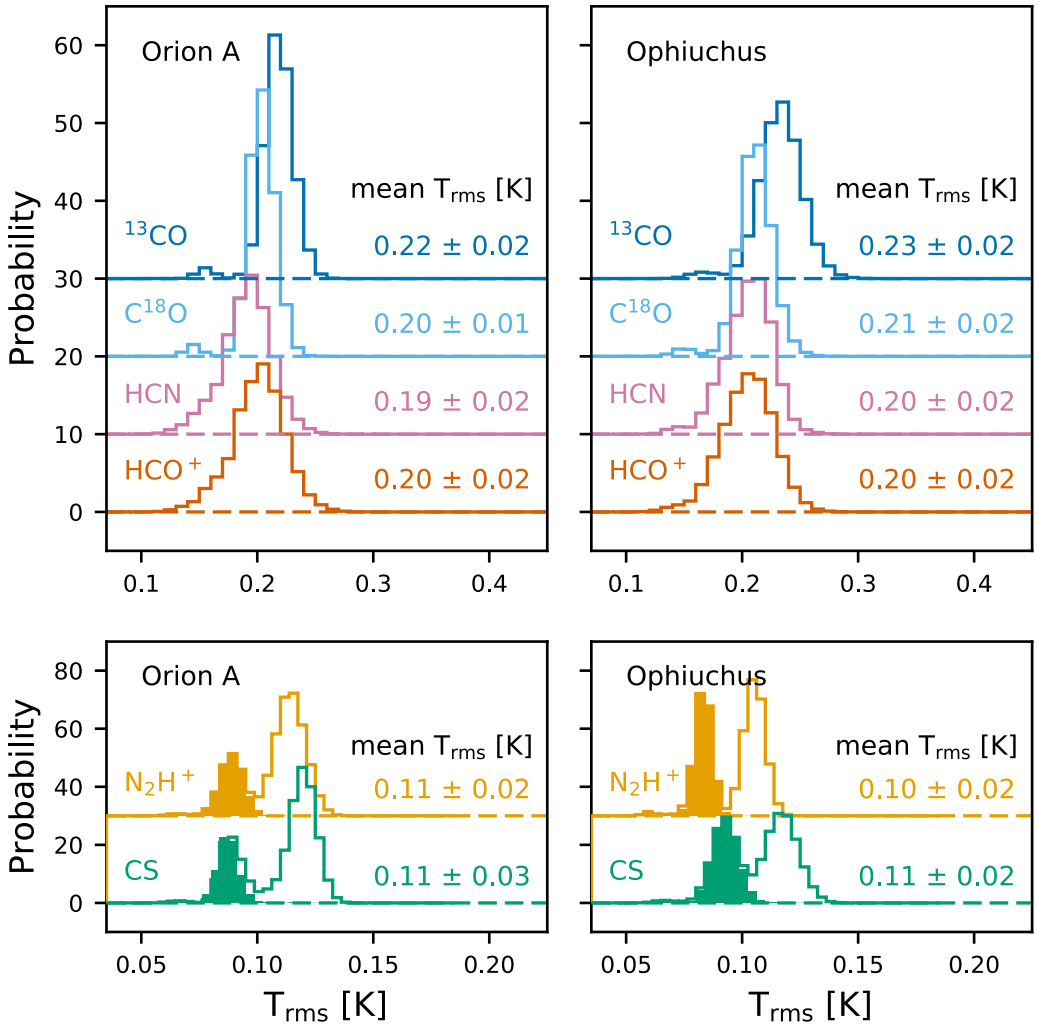

Figure 8. The pdfs of the T_{rms} for the observed maps in the Orion A (left panels) and Ophiuchus (right panels) clouds. The top panels show the pdfs for the ^{13}CO, $C^{18}O$, HCN, and HCO^+ maps, and the bottom panels show those for the N_2H^+ and CS maps. The T_{rms} pdfs for the N_2H^+ and CS lines toward the representative star-forming regions (orange dotted lines in Figure 1) are presented with the filled histograms. The mean and standard deviation for each pdf are summarized on the right side of each pdf.

thus derived I_{center} over a velocity range from 5 to 13 km s^{-1} assuming that the central peak extends up to ±4 km s^{-1} from the line center. I_{wing} was calculated over the velocity ranges from −11 to 5 km s^{-1} and from 13 to 29 km s^{-1} assuming that the wings extend up to ±20 km s^{-1} from the line center. For the HCN and N_2H^+ lines, the velocity ranges for obtaining I_{center} were set to

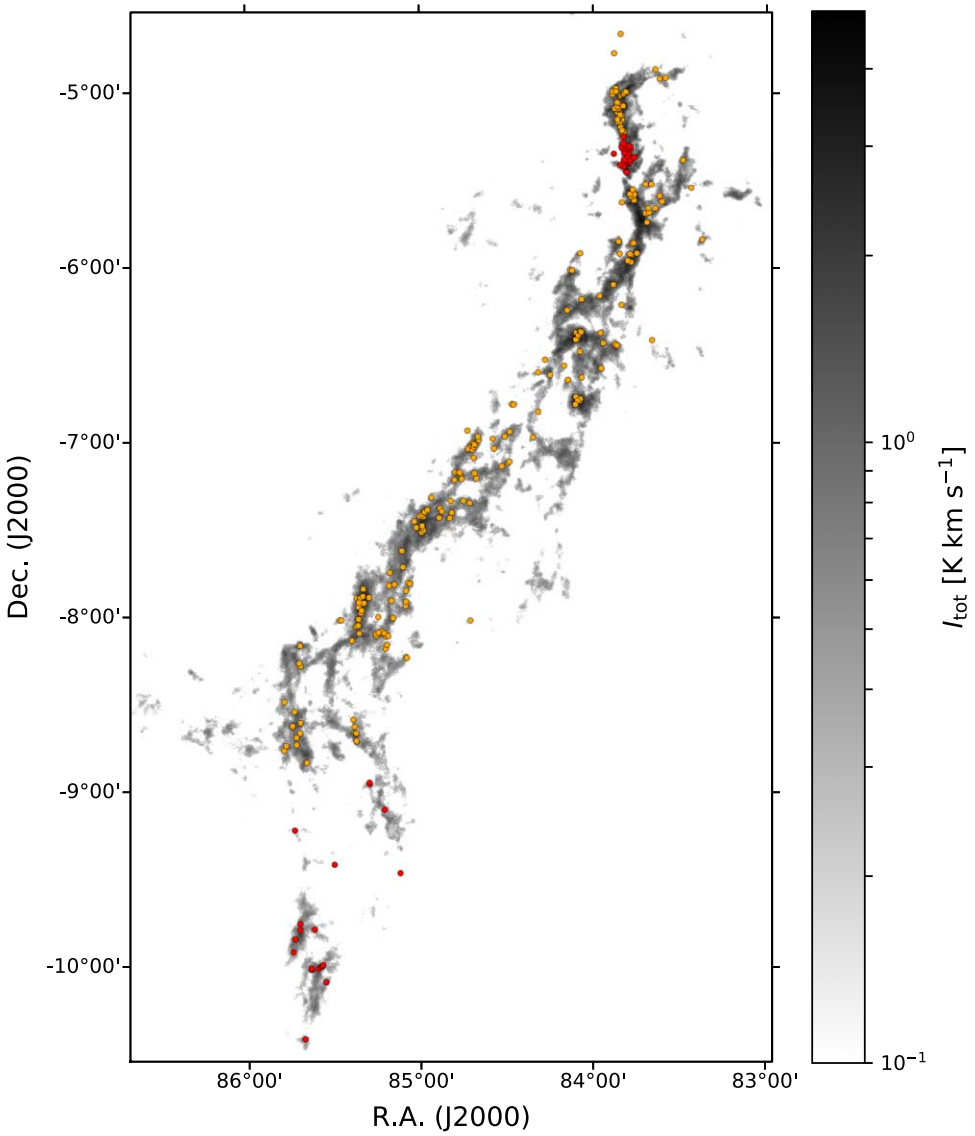

Figure 9. Distribution of young embedded protostars in the Orion A cloud. The background image is the I_{tot} map of $C^{18}O$. The Class 0/I YSOs and flat-spectrum sources, identified with Herschel space observatory (Furlan et al. 2016), are presented with orange circles. Since Furlan et al. (2016) did not provide YSOs near the Orion Nebula and the southernmost part of the cloud, we adopt the Spitzer YSO catalog provided by Megeath et al. (2012) (red circles).

cover all hyperfine components. Also, we set the velocity ranges of the wing structures to consider the broad emission features at the outermost parts of the observed lines.

Figure 11 presents the I_{center} and I_{wing} for each line. I_{wing} values are generally proportional to I_{center}. The ^{13}CO, HCN, HCO^+, and CS lines have relatively strong I_{wing} values that are higher than 10 K km s^{-1}. I_{wing} of $C^{18}O$ is barely detected (1.1 ± 0.3 K km s^{-1}). Only the N_2H^+ line is not detected with a value of -0.16 ± 0.17 K km s^{-1}. Figure 12 presents the distributions of the broad wing emission in ^{13}CO, $C^{18}O$, HCN, HCO^+, and CS. Note that the distribution of wing emission in $C^{18}O$ is indistinguishable from the noise.

4.2.2. The Ophiuchus Cloud

In the Ophiuchus cloud, the observed lines exhibit spatial distribution trends that are similar to those in the Orion A cloud. The ^{13}CO line traces extended cloud structures from the L1688 to L1709 regions (the regions of the cloud are identified in Figure 3). The other lines mainly trace small and clumpy structures in the cloud. The line intensities are generally strong in L1688 (R.A. < 247.5), which is the most active star-forming region in this cloud. Also, the spatial distribution of the $C^{18}O$ line emission is well correlated with that of the young embedded protostars identified using Spitzer (Dunham et al. 2015; see Figure 13).

In L1688, the observed lines are generally strong toward the star-forming cores (Oph-A through L; see Figure B4). But their relative strengths change depending on the lines. The star-forming cores have nonuniform conditions (Pattle et al. 2015; Punanova et al. 2016). Oph-A and Oph-C are affected by the external heating from the B2V star HD 147889 (Pattle et al. 2015; Punanova et al. 2016). Oph-B1 and Oph-B2 cores are the coldest among the cores (Pattle et al. 2015); Oph-B1 is one of the quiescent cores, while Oph-B2 is the most turbulent core (Punanova et al. 2016). Oph-E and Oph-F cores are the most evolved regions in L1688 (Pattle et al. 2015); Oph-E is strongly pressure confined, while Oph-F is marginally pressure confined. Also, Oph-F has a similar temperature to that of Oph-A without any external heating. These different environments result in the different relative strengths of the observed lines.

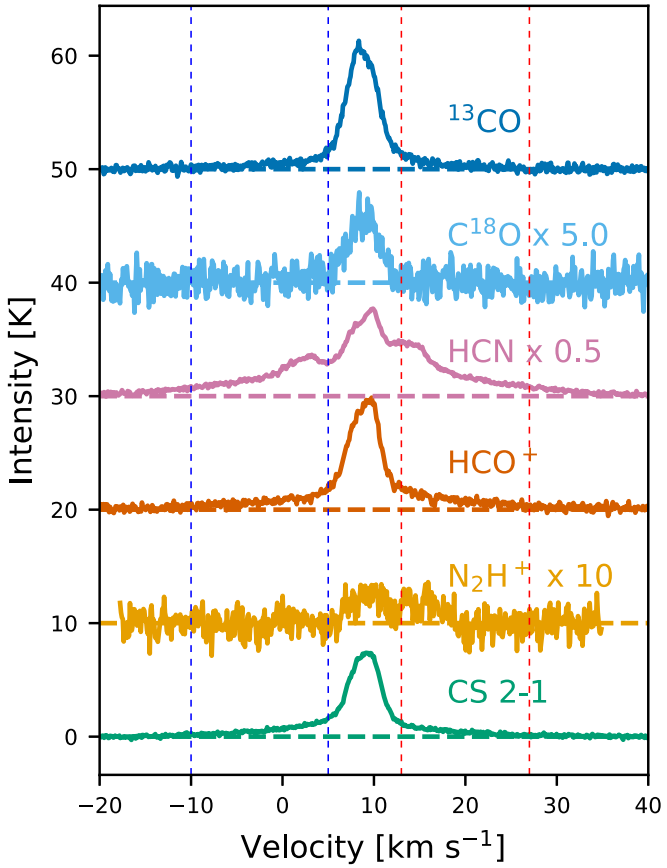

Figure 10. Observed lines toward Orion KL. The red and blue dotted vertical lines indicate the velocity ranges where the red (from −10 to +5 km s^{-1}) and blue (from +13 to +27 km s^{-1}) wing structures are presented.

Table 3
The Velocity Ranges for the Central Peak and Broad Wings

Line	Central Peak (km s^{-1})	Blue/Red Wings (km s^{-1})
^{13}CO	(5.0, 13.0)	(−11.0, 5.0)/(13.0, 29.0)
C^{18}O	(5.0, 13.0)	(−11.0, 5.0)/(13.0, 29.0)
HCN	(0.2, 20.1)	(−15.8, 0.2)/(20.1, 36.1)
HCO$^+$	(5.0, 13.0)	(−11.0, 5.0)/(13.0, 29.0)
N_2H^+	(−1.7, 21.2)	(−17.7, −1.7)/(21.2, 37.2)
CS	(5.0, 13.0)	(−11.0, 5.0)/(13.0, 29.0)

The $I_{\rm tot}$ of the ^{13}CO line in Oph-A is stronger than that in Oph-C, while that of C^{18}O in Oph-A is similar to that in Oph-C. Lada & Wilking (1980) found that ^{13}CO $J=1-0$ is optically thick with a self-absorption feature in some positions. We thus investigated the ^{13}CO and C^{18}O lines toward the dense cores, where the ^{13}CO line can probably be optically thick. Figure 14 presents the ^{13}CO and C^{18}O line spectra toward the 13 cores in L1688 (Pan et al. 2017) and two DCO$^+$ cores in L1709 (Loren et al. 1990). Some of the dense cores present self-absorption features in their ^{13}CO line spectra.

Figures 6 and 7 show the $V_{\rm lsr}$ and σ_V maps for the ^{13}CO line in the Ophiuchus cloud. The $V_{\rm lsr}$ value varies from +1.5 to +4.0 km s^{-1} across the Ophiuchus cloud. The $V_{\rm lsr}$ map shows that the L1688 and L1709 regions have different $V_{\rm lsr}$. The $V_{\rm lsr}$ values of L1688 are around 3.5 km s^{-1}, while that in L1709 is around 2.5 km s^{-1}. From this result, Loren (1989b) suggested that L1709 may be separate from L1688. Neither L1688 nor L1709 regions have any overall motions in the ^{13}CO line. We also checked the optically thinner C^{18}O line, but there is no overall motion in each region (see Appendix D). The σ_V is about 0.5 km s^{-1} across the Ophiuchus cloud.

The moment maps of the ^{13}CO line imply that the kinematic features of the Ophiuchus cloud are quite different from those of the Orion A cloud. The systematic variation of the $V_{\rm lsr}$ in the Ophiuchus cloud is relatively small compared to that in the Orion A cloud. Also, the typical σ_V value in the Ophiuchus cloud is smaller than that in the Orion A cloud. The small variation of $V_{\rm lsr}$ and small σ_V values imply that the Ophiuchus cloud is kinematically quiescent compared to the Orion A cloud (Loren 1989b).

The difference between the spatial distributions of the HCN and HCO$^+$ lines is striking (see Figures B2 and B3). The HCN line is mainly detected toward Oph-A, Oph-B1, Oph-B2, and Oph-B3 cores, while the HCO$^+$ line is predominantly detected toward Oph-A, Oph-C, Oph-E, and Oph-F cores. The peak $I_{\rm tot}$ of the HCN and HCO$^+$ lines also appear in different cores. This result indicates that the HCN and HCO$^+$ lines trace different physical or chemical conditions in the Ophiuchus cloud.

4.3. Column Density Maps and I_{tot} Variations with Column Density

Unbiased mapping toward two MCs in multiple molecular lines provides a good opportunity to assess how the line intensities respond to the physical parameters within clouds. Therefore, we investigated the variation of $I_{\rm tot}$ as a function of column density ($N_{\rm H_2}$).

We derived $N_{\rm H_2}$ from the observations of dust continuum emission that can trace the amount of gas in a cloud (Goodman et al. 2009). The $N_{\rm H_2}$ maps were derived by fitting a modified blackbody (MBB) into the spectral energy distribution (SED) of the continuum emission from cold dust. Archival Herschel PACS (160 μm) and SPIRE (250, 350, and 500 μm) continuum observations that were obtained as part of the Herschel Gould Belt Survey (André et al. 2010) are adopted. Note that the PACS 100 and 70 μm observations are not included in the SED fitting. The 100 μm continuum observation was not covered by the Herschel Gould Belt Survey (André et al. 2010). For the 70 μm band, the MBB fitting with a single temperature cannot fit the observed emission in some cases because of the contamination due to nonequilibrium emission from small dust grains (Roy et al. 2013). Even if the detailed dust model is applied to the SED fitting including the 70 μm data, the derived column density is not significantly different from that derived using the single-temperature MBB fitting without the 70 μm data (Bianchi 2013).

The continuum emission maps were calibrated using Planck observations of the same regions via the method in Chen et al. (2019). Using the calibrated data, the column density maps were derived in two steps (Friesen et al. 2017; Chen et al. 2019): (1) dust temperature ($T_{\rm d}$) and optical depth (τ_{ν_0}) maps were found via the SED fitting, and (2) the $N_{\rm H_2}$ maps were obtained from the τ_{ν_0} map by multiplying by a conversion factor assuming a gas-to-dust mass ratio of 100,

$$\frac{N_{\rm H_2}}{\tau_{\nu_0}} = \frac{1}{100\ \kappa_{\nu_0}\ \mu_{\rm H_2}\ m_{\rm H}}, \quad (1)$$

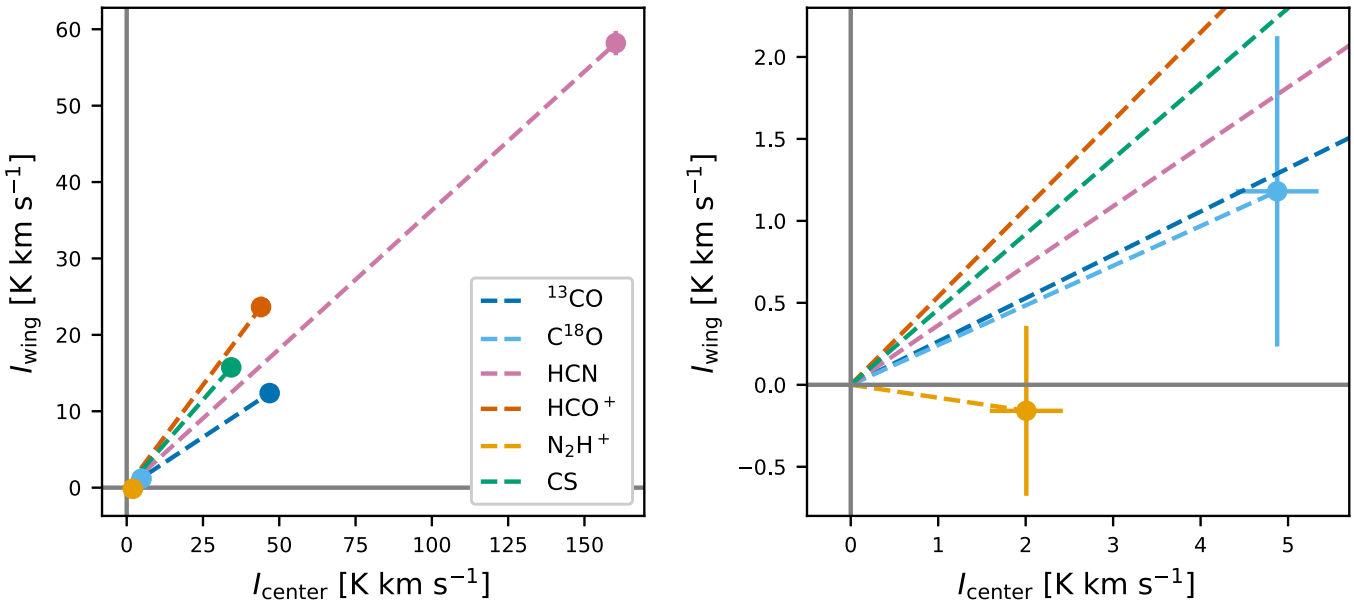

Figure 11. Left: comparison between the integrated intensities for the central peak (I_{center}) and broad wing structures (I_{wing}) of the Orion KL line spectra presented in Figure 10. The 3σ error ranges are presented in the error bars; however, their sizes are similar to or smaller than the symbol size. The gray solid lines indicate the position of the origin, and each dashed line presents the straight line from the origin to each data point. Right: zoom-in on the origin of the diagram.

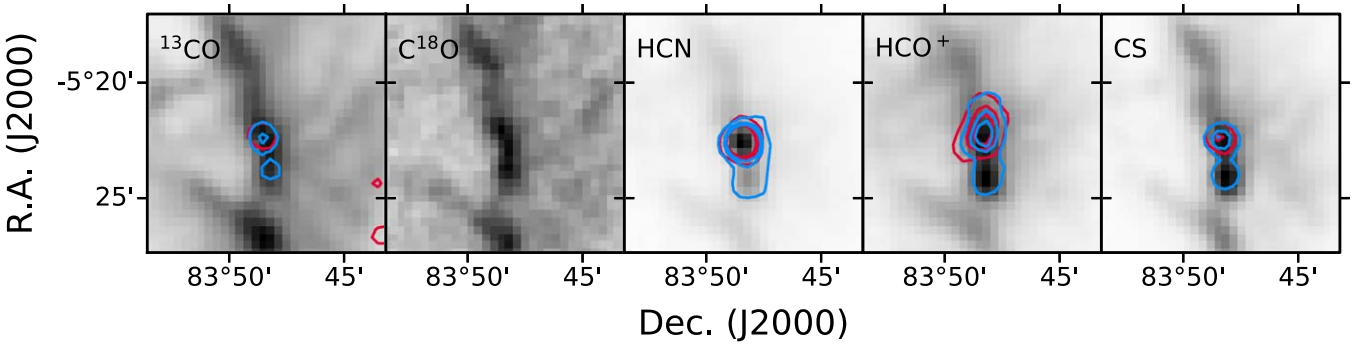

Figure 12. Spatial distributions of the broad wing emission. In each panel, the red and blue contours indicate the integrated intensities for the red- and blueshifted wings. The contour levels are 2, 6, and 9 K km s^{-1}. The background image exhibits the map of I_{center}.

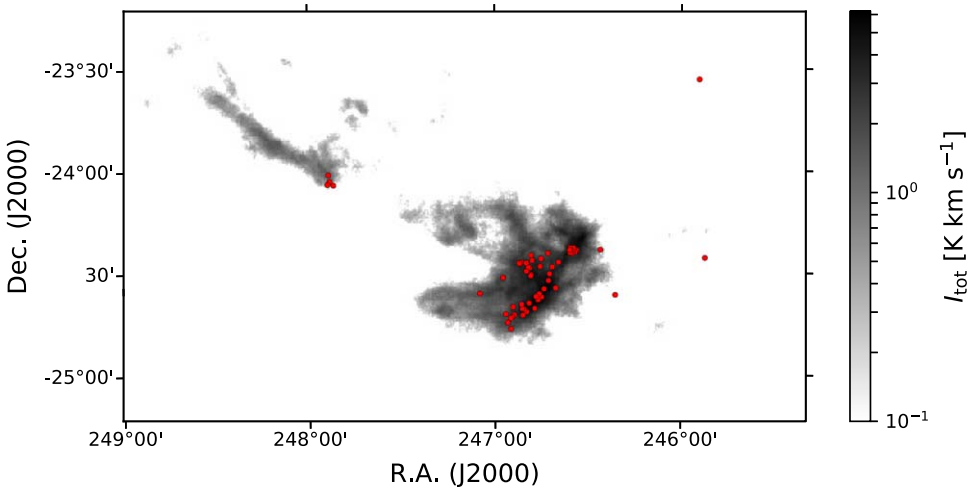

Figure 13. Distribution of young embedded protostars in the Ophiuchus cloud. The background image is the I_{tot} map of C^{18}O, and the YSO catalog provided by Dunham et al. (2015) is presented with red circles.

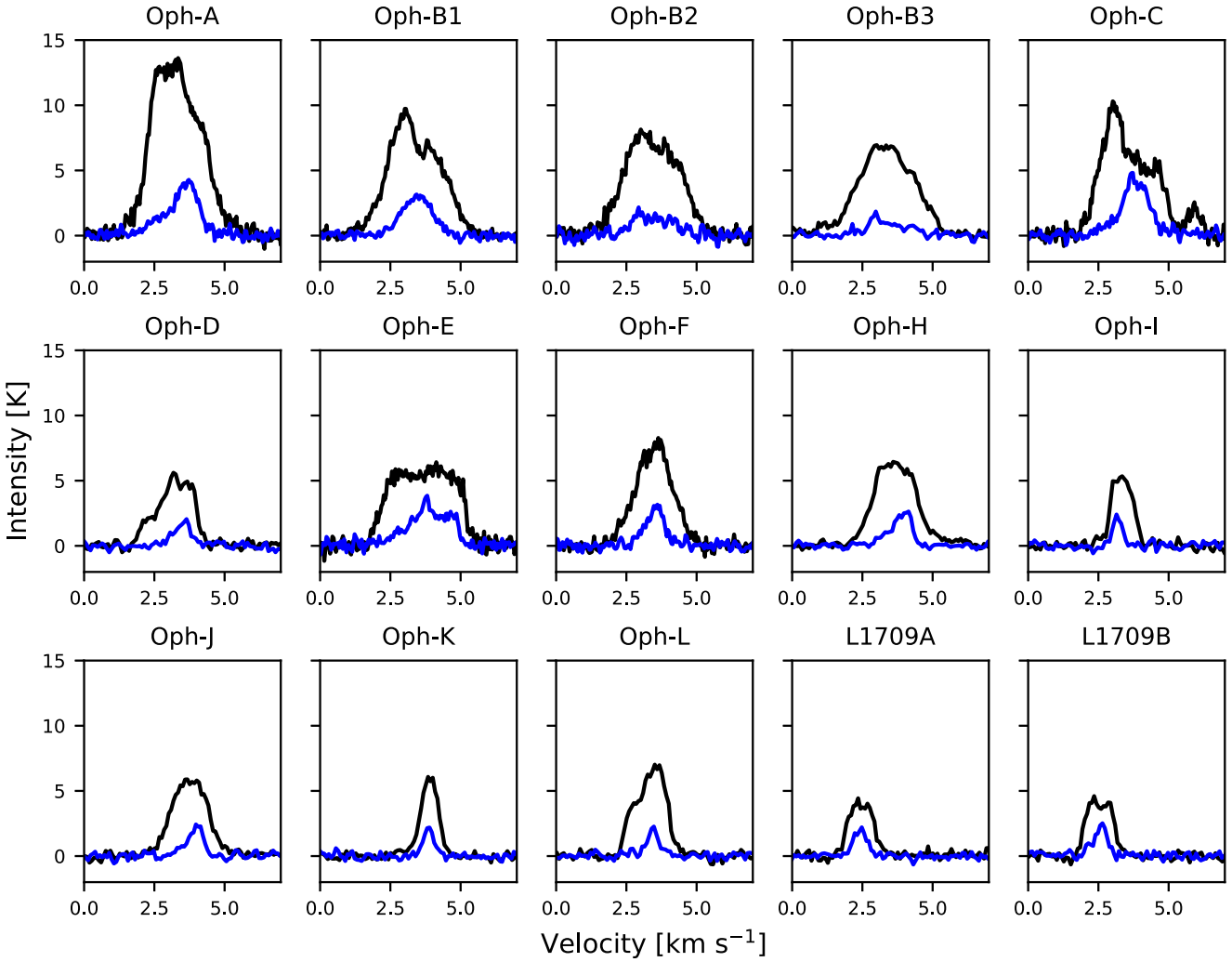

Figure 14. Observed ^{13}CO (black) and C^{18}O (blue) lines toward the dense cores (Loren et al. 1990; Pan et al. 2017).

where κ_{ν_0} is the opacity of 0.1 cm^2 g^{-1} at ν_0 of 1000 GHz (Hildebrand 1983), μ_{H_2} is a mean molecular weight per H_2 molecule of 2.8, and m_H is the mass of a hydrogen atom. The final map has a beam size of 36″, which is the resolution of the SPIRE 500 μm data. We thus convolved the N_{H_2} map to have a resolution of 50″, which is comparable to the beam sizes of the TRAO maps (see Table 1).

The I_{tot} of each observed line generally increases as N_{H_2} increases up to a certain N_{H_2} and remains relatively constant after that certain N_{H_2} (see Figures 15 and 16 for the Orion A and Ophiuchus clouds, respectively). We fit the I_{tot} variation with a power-law relation to characterize how I_{tot} of a molecular line changes as N_{H_2} increases. In this process, we divide the Orion A cloud into two subregions, the ISF region (decl. $> -6°$) and the rest of the cloud (decl. $< -6°$), because ISF is more likely to be affected by the photon-dominated region (PDR; Shimajiri et al. 2014). Hereafter, ISF, the other regions in the Orion A cloud, and the Ophiuchus cloud are referred to as the ISF, L1641, and Ophiuchus regions.

For each line in each of the ISF, L1641, and Ophiuchus regions, the mean values of the I_{tot}, peak temperature (T_{peak}), T_d, and σ_V for a given N_{H_2} are investigated. The line spectra were separated into regularly spaced $\log(N_{H_2})$ bins with a size of $\Delta \log(N_{H_2}) = 0.1$. We derived the mean values of I_{tot} and σ_V for each bin, weighting the values by the inverse of the square of the uncertainty. For the T_{peak} and T_d, the arithmetic mean values are adopted. Note that the variation of T_d seems to be relatively constant because it generally varies from 12 to 20 K in most areas except near the heating sources (such as OMC-1 and NGC 1977 in the Orion A cloud and HD 147889 in the Ophiuchus cloud).

We investigated the power-law indices, which can explain the variation of the mean I_{tot} values ($\bar{I}_{tot}$). We fitted the data with a power law: $\log I_{fit} = \log b + \alpha \log N_{H_2}$. The χ^2 minimization technique was used to obtain the fit parameters. The χ^2 value is defined as follows:

$$\chi^2 = \sum \left(\frac{\bar{I}_{tot} - I_{fit}}{\bar{\epsilon}_{mom0}} \right)^2, \quad (2)$$

where the sum is over the bin numbers, I_{fit} is an expected I_{tot} value from the power-law fit, and $\bar{\epsilon}_{mom0}$ is the uncertainty of $\bar{I}_{tot}$. For C^{18}O, HCN, HCO$^+$, N_2H^+, and CS, there are several data points with very weak and relatively constant I_{tot} at a low-N_{H_2} regime ($N_{H_2} < 2 \times 10^{21}$ cm^{-2}). These data points are the weighted means of a few pixels. Their line spectra are generally dominated by the noise, although the moment-masking method identified them as emission lines. Therefore, we excluded these

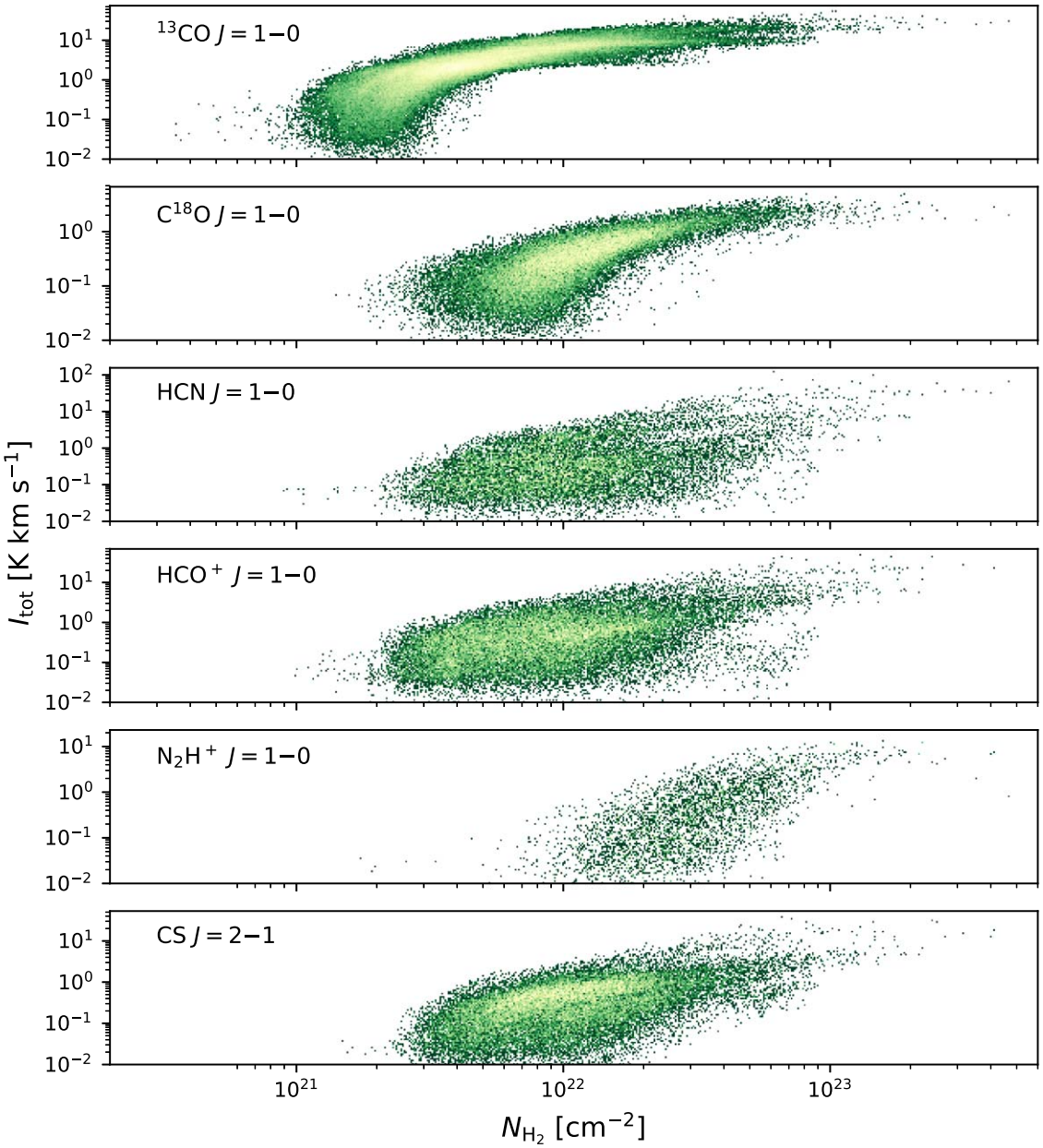

Figure 15. Comparison of I_{tot} and column density (N_{H_2}) in the Orion A cloud. From the top to bottom panels, the diagrams show the ^{13}CO, C^{18}O, HCN, HCO$^+$, N$_2$H$^+$, and CS lines.

data points from the power-law fitting. The N_{H_2} ranges for power-law fits were visually defined. The N_{H_2} ranges for the fitting and the best-fit power-law indices (α) are listed in Table 4.

Figure 17 shows the I_{tot} variation of the ^{13}CO and C^{18}O lines. For these lines, we divided the N_{H_2} range into three regimes: (1) the low-N_{H_2} regime, where I_{tot} steeply increase ($\alpha > 2.0$); (2) the intermediate-N_{H_2} regime, where I_{tot} is proportional to N_{H_2} ($\alpha \sim 1.0$); and (3) the high-N_{H_2} regime, where I_{tot} becomes relatively constant ($\alpha < 1.0$). The detailed N_{H_2} ranges are different depending on the lines and regions; however, their I_{tot} variations are similar.

Figure 18 shows the I_{tot} variations in HCN, HCO$^+$, and CS lines. The variations of I_{tot} are quite different depending on the lines and regions and cannot be explained with a single trend. Their I_{tot} variations should be interpreted individually. The I_{tot} variation of the N$_2$H$^+$ line is presented in Figure 19. The N$_2$H$^+$ line is only detected at the high-N_{H_2} regions, where N_{H_2} is higher than 10^{22} cm^{-2}. We will discuss these results in Sections 5.2 and 5.3.

5. Discussion

5.1. Broad Wing Structures in the Orion KL Spectra

As noted above, the Orion KL region shows wide line wings in ^{13}CO, HCN, HCO$^+$, and CS; marginally in C^{18}O; and not in N$_2$H$^+$. Wannier & Phillips (1977) suggested that ^{12}CO $J = 1-0$ is optically thin in the wings. The ^{13}CO and C^{18}O lines thus would be optically thinner at the line wings. In this case, the intensity ratio between the ^{13}CO and C^{18}O lines is probably close to their abundance ratio (Wannier & Phillips 1977). The ratio between I_{wing} of the ^{13}CO and C^{18}O lines is 10.5 ± 2.8.

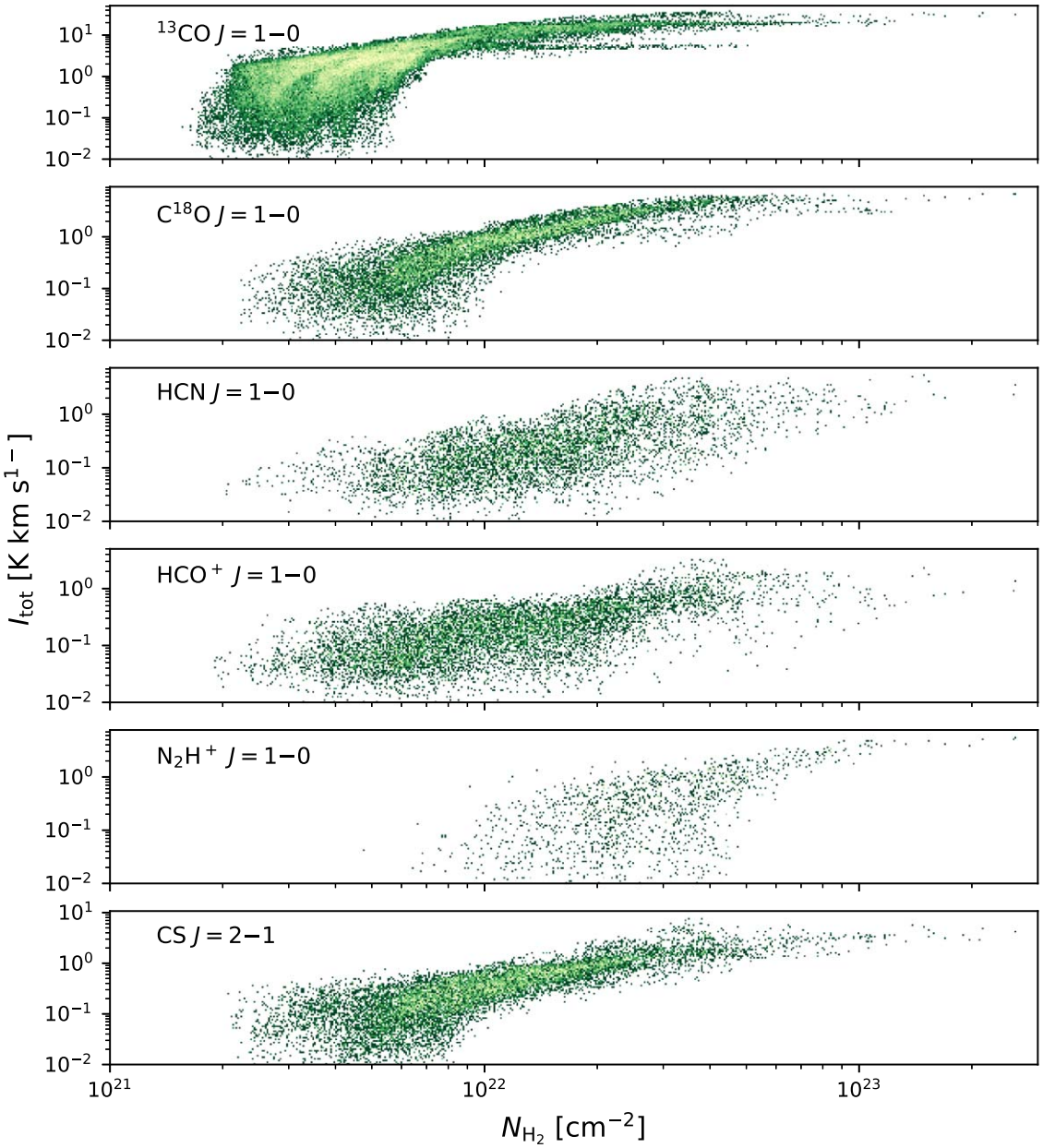

Figure 16. Same as Figure 15, but for the Ophiuchus cloud.

This value is close to the abundance ratio determined by Shimajiri et al. (2014) ($X_{^{13}CO}/X_{C^{18}O} = 12.14$) within a 1σ range.

The ratios between I_{wing} and I_{center} for the HCN, HCO$^+$, and CS lines are slightly different. The origins of the broad wing structures were discussed in previous works (Kuiper et al. 1980; Rydbeck et al. 1981; Olofsson et al. 1982; Hasegawa et al. 1984). The bipolar outflows aligned with the line of sight are suggested as the origin of the high-velocity wings (Olofsson et al. 1982). In this case, the high-velocity emission is spatially confined close to Orion KL. For the HCO$^+$ line, the contribution of the shocked gas is also suggested (Rydbeck et al. 1981; Olofsson et al. 1982; Johansson et al. 1984). In addition, the abundance enhancement of HCN and HCO$^+$ in the high-velocity components is also reported (Rydbeck et al. 1981; Johansson et al. 1984). Hasegawa et al. (1984) analyzed the CS line and suggested the existence of a large gas disk around the Orion KL nebula. They also mentioned that the high-velocity emission corresponding to the bipolar outflows was not observed in CS. These results may be related to the differences in ratios between I_{wing} and I_{center}.

5.2. Variation of I_{tot} as a Function of N_{H_2}

If *all* the following assumptions are true (the lines are optically thin, stimulated radiative processes can be ignored, excitation temperatures are much lower than the kinetic temperature (T_K), and the abundance of the species is constant), the line intensity is proportional to n^2 because every collision leads to a photon. If the line-of-sight depth is constant, the line intensity is also proportional to $N_{H_2}^2$, as is generally true for optical or infrared emission lines. All these conditions are rarely met for millimeter-wave molecular emission lines. The fact that the excitation temperature is limited below by the radiation temperature and above by the kinetic temperature constrains the regime of densities over which every collision

Table 4
Power-law Fitting Results

Region	Line	$\log(N_{H_2})$	α	$\log(b)$
ISF	^{13}CO	21.0–21.7	2.79 ± 0.24	−59.99 ± 5.22
ISF	^{13}CO	21.7–22.3	0.87 ± 0.06	−18.30 ± 1.36
ISF	^{13}CO	22.3–23.3	0.31 ± 0.03	−5.86 ± 0.58
L1641	^{13}CO	21.0–21.6	2.80 ± 0.14	−60.18 ± 3.00
L1641	^{13}CO	21.6–22.2	0.98 ± 0.09	−20.92 ± 1.89
L1641	^{13}CO	22.2–23.2	0.28 ± 0.03	−5.43 ± 0.64
Ophiuchus	^{13}CO	21.3–21.9	3.09 ± 0.21	−66.78 ± 4.59
Ophiuchus	^{13}CO	21.9–22.3	0.82 ± 0.07	−17.17 ± 1.55
Ophiuchus	^{13}CO	22.3–23.2	0.28 ± 0.04	−5.11 ± 0.79
ISF	C^{18}O	21.5–22.2	1.73 ± 0.14	−38.57 ± 3.12
ISF	C^{18}O	22.2–22.8	0.94 ± 0.08	−21.01 ± 1.78
ISF	C^{18}O	21.8–23.3	0.11 ± 0.12	−2.21 ± 2.72
L1641	C^{18}O	21.6–22.2	1.90 ± 0.16	−42.60 ± 3.45
L1641	C^{18}O	22.2–22.7	0.99 ± 0.06	−22.14 ± 1.38
L1641	C^{18}O	22.7–23.2	0.49 ± 0.04	−10.95 ± 0.89
Ophiuchus	C^{18}O	21.6–22.2	2.53 ± 0.18	−55.99 ± 3.92
Ophiuchus	C^{18}O	22.2–22.7	0.87 ± 0.06	−19.20 ± 1.40
Ophiuchus	C^{18}O	22.7–23.2	−0.14 ± 0.16	3.83 ± 3.74
ISF	HCN	21.5–22.3	0.69 ± 0.11	−15.86 ± 2.32
ISF	HCN	22.3–22.9	2.24 ± 0.14	−50.47 ± 3.10
ISF	HCN	22.9–23.3	1.21 ± 0.15	−26.84 ± 3.45
L1641	HCN	21.4–22.3	0.59 ± 0.03	−13.95 ± 0.72
L1641	HCN	22.3–22.8	0.81 ± 0.11	−18.95 ± 2.38
L1641	HCN	22.8–23.2	3.50 ± 0.83	−80.52 ± 19.07
Ophiuchus	HCN	21.7–22.3	0.89 ± 0.03	−20.63 ± 0.56
Ophiuchus	HCN	22.3–23.0	1.31 ± 0.09	−29.88 ± 2.00
ISF	HCO$^+$	21.5–22.4	1.44 ± 0.04	−31.87 ± 0.94
ISF	HCO$^+$	22.4–23.0	1.02 ± 0.04	−22.46 ± 0.96
ISF	HCO$^+$	23.0–23.3	0.60 ± 0.11	−13.01 ± 2.44
L1641	HCO$^+$	21.3–22.0	0.55 ± 0.03	−12.91 ± 0.69
L1641	HCO$^+$	22.0–22.6	0.74 ± 0.05	−17.06 ± 1.03
L1641	HCO$^+$	22.7–23.2	3.55 ± 0.70	−81.47 ± 16.08
Ophiuchus	HCO$^+$	21.7–22.3	0.84 ± 0.07	−19.52 ± 1.44
Ophiuchus	HCO$^+$	22.3–22.6	1.68 ± 0.18	−38.17 ± 4.13
Ophiuchus	HCO$^+$	22.6–23.0	0.21 ± 0.20	−4.91 ± 4.64
ISF	CS	21.4–22.0	2.59 ± 0.08	−57.12 ± 1.75
ISF	CS	22.0–23.3	0.89 ± 0.02	−19.67 ± 0.47
L1641	CS	21.4–22.7	1.19 ± 0.03	−27.10 ± 0.68
L1641	CS	22.7–23.2	1.48 ± 0.28	−33.80 ± 6.40
Ophiuchus	CS	21.6–22.1	2.49 ± 0.13	−55.23 ± 2.83
Ophiuchus	CS	22.1–22.6	1.26 ± 0.04	−28.25 ± 0.93
Ophiuchus	CS	22.6–23.2	0.63 ± 0.02	−13.90 ± 0.53
ISF	N_2H^+	22.0–22.6	2.01 ± 0.11	−45.76 ± 2.55
ISF	N_2H^+	22.8–23.3	0.99 ± 0.05	−22.01 ± 1.14
L1641	N_2H^+	22.0–22.4	0.75 ± 0.05	−18.08 ± 1.10
L1641	N_2H^+	22.4–22.8	2.16 ± 0.10	−49.65 ± 2.26
L1641	N_2H^+	22.8–23.2	2.76 ± 0.46	−63.10 ± 10.58
Ophiuchus	N_2H^+	22.1–22.6	1.02 ± 0.19	−23.87 ± 4.17
Ophiuchus	N_2H^+	22.8–23.2	1.10 ± 0.24	−24.85 ± 5.44

leads to a photon. Optical depth increasing with N_{H_2} also leads intensity to increase more slowly with N_{H_2}. For lines that reach optical depth near unity and excitation temperatures near the kinetic temperature, the intensity should plateau with $T_{peak} \approx T_K$. The dependence of I_{tot} on N_{H_2} is a complicated function of density, temperature, abundance, and velocity field.

Examination of Figures 17 and 18 and the fits in Table 4 show broad agreement with these predictions. At low N_{H_2}, the fits to intensity versus $\log(N_{H_2})$ are superlinear, but they become closer to linear at higher N_{H_2} before reaching plateaus at levels that depend on T_K. The middle plots of Figures 17 and 18 show T_{peak} and T_d from Herschel. For densities above a few times 10^4 cm^{-3}, $T_K \approx T_d$. For ^{13}CO, T_{peak} indeed levels off near T_d, as predicted for optically thick, thermalized lines. None of the other transitions reach this point, so the fits to their slopes indicate that they lie primarily in the intermediate zone between growing like $N_{H_2}^2$ and the plateau. N_2H^+ is the exception, with slope near the predicted value of 2 over a substantial range of N_{H_2} in the ISF, where T_K is relatively high.

Kauffmann et al. (2017) analyzed the ^{13}CO, C^{18}O, HCN, and N_2H^+ lines in the northern part of ISF and presented the normalized line-to-mass ratio as a function of the visual extinction (A_V) derived from Herschel column density. Figure 2 in Kauffmann et al. (2017) showed that there is a certain A_V regime where the line-to-mass ratios remain relatively constant, which means that the I_{tot} is proportional to N_{H_2}. Table 5 shows the A_V regimes where the line-to-mass ratio remains constant and corresponding N_{H_2} values for each line for the lines studied by Kauffmann et al. (2017) and the corresponding values for our study.

For the ^{13}CO, C^{18}O, and N_2H^+ lines, the N_{H_2} regime with α of about 1.0 is generally consistent with that from Kauffmann et al. (2017). The N_{H_2} regimes for $\alpha \sim 1.0$ that are derived in this study are larger than those of Kauffmann et al. (2017). For the HCN line, the N_{H_2} regime is quite different from what Kauffmann et al. (2017) presented. Kauffmann et al. (2017) only adopted a small region north of −5:10:00 decl. (J2000) to avoid the effect of radiation that is emitted from the Orion Nebula. However, the whole region north of −6:00:00 decl. (J2000), including OMC-1, is included in this study. The different results for column density regimes might be caused by the difference in the areas that are included in each analysis.

5.2.1. ^{13}CO J = 1–0

The ^{13}CO line has $\alpha > 2$ where $N_{H_2} < 10^{22}$ cm^{-2}. The uncertainty of α in these regimes is larger than that in the other regimes. Thus, detailed interpretation of I_{tot} variation using α could be uncertain. The α values in intermediate-N_{H_2} regimes are close to 1.0 and become shallower in the high-N_{H_2} regime ($\alpha \sim 0.3$). This result indicates that the ^{13}CO lines in both clouds are optically thick toward high-N_{H_2} regions and cannot trace all the gas along the line of sight. In the Ophiuchus cloud, self-absorption features appear in the ^{13}CO line spectra toward the star-forming cores. These results are consistent with previous studies showing that the ^{13}CO line can be optically thick in the Orion A (Shimajiri et al. 2014) and Ophiuchus (Lada & Wilking 1980) clouds.

In this analysis, we neglected the effect of abundance variation within MCs. In fact, the I_{tot} variation of the ^{13}CO line also can be affected by the chemical difference between the subregions. The ISF region is also affected by the PDRs heated by the Trapezium stars (Shimajiri et al. 2014). In cold dense regions, ^{13}CO can freeze onto dust grains.

5.2.2. $C^{18}O$ J = 1–0

The observed C^{18}O lines preferentially trace regions of higher column density than are traced by the ^{13}CO line. This is understood as the effect of lower abundance (Wilson & Rood 1994), which translates into lower optical depth and less radiative trapping. When N_{H_2} is smaller than 3×10^{22} cm^{-2}, only a few weak emission lines were detected. If we observe both clouds more deeply, the I_{tot} variation in very low N_{H_2} regimes would be accessible.

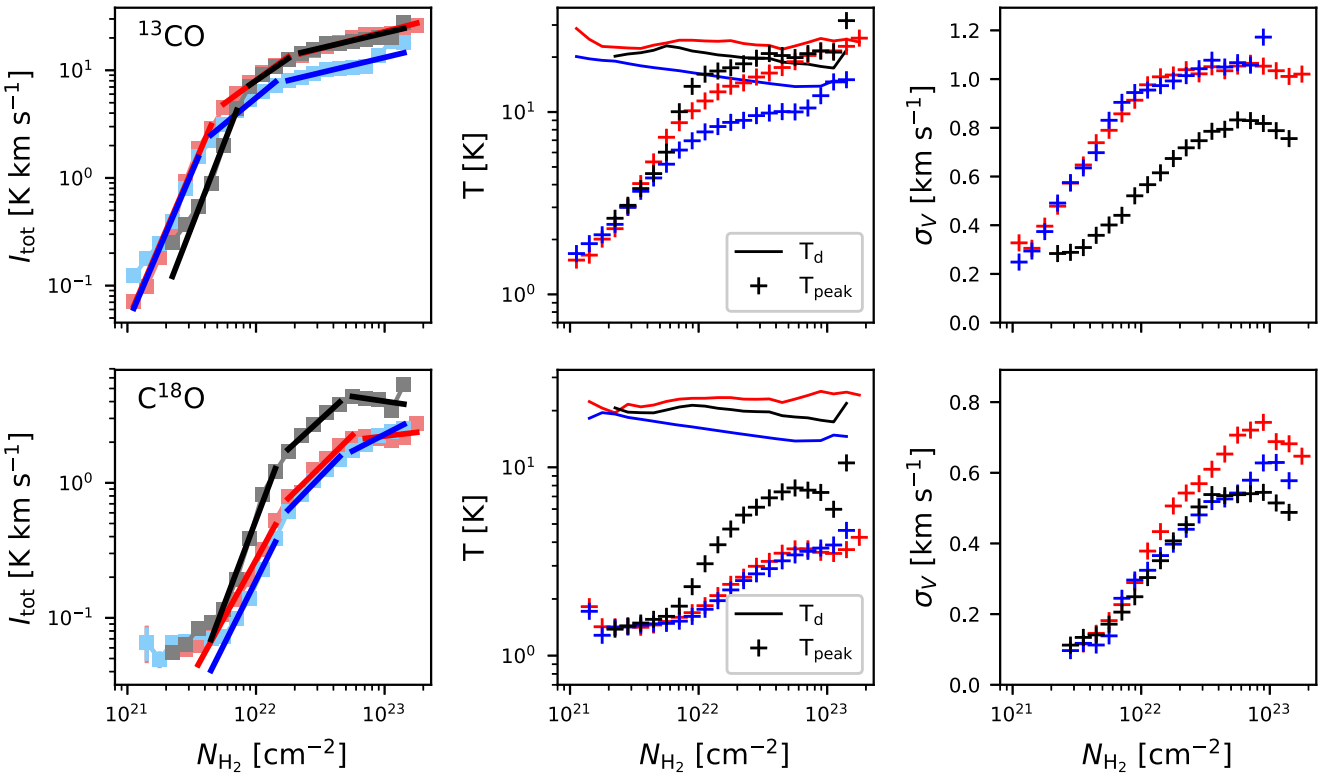

Figure 17. Variation of means of I_{tot} (left), T_{peak} (middle), and σ_V (right) for the ^{13}CO (top) and C^{18}O (bottom) lines. The red, blue, and black colors indicate the results for the ISF, L1641, and Ophiuchus regions. The mean I_{tot} values and their 1σ error ranges are presented with square symbols and error bars with weak colors. The red, blue, and black solid lines indicate the power-law fitting results. In the middle panel, the mean T_{peak} values are presented with the plus signs, and the variations of mean T_d values are also exhibited in solid lines.

In the intermediate-N_{H_2} regime, where N_{H_2} is between 1.6×10^{22} cm^{-2} and 5.0×10^{22} cm^{-2}, the α values are ~1. If N_{H_2} exceeds 5.0×10^{22} cm^{-2}, the slopes become shallower. In the ISF and Ophiuchus regions, α becomes comparable to zero. For the ISF region, Shimajiri et al. (2014) found that C^{18}O $J = 1-0$ is optically thin, and the abundance of C^{18}O would be affected by the selective photodissociation in PDR chemistry. Abundance variations caused by photodissociation or freezeout (Caselli et al. 1999) can also affect the line emission. In the Ophiuchus region, I_{tot} sharply increases beyond N_{H_2} of 10^{23} cm^{-2}. This increase results from a selection bias; the highest N_{H_2} bin originates only from the Oph-A core that has the highest N_{H_2} and T_d within the Ophiuchus region.

5.2.3. *HCN* J = 1–0 *and* *HCO$^+$* J = 1–0

The I_{tot} for the HCN and HCO$^+$ lines shows different variation depending on the lines and regions. Also, the α for a given line and region changes in different ways depending on the N_{H_2} regimes. Only the I_{tot} variation for the HCO$^+$ line in the ISF region is similar to what the ^{13}CO and C^{18}O lines exhibited. This difference seen in the HCO$^+$ and HCN lines may be due to different star formation activities in different regions. HCO$^+$ and HCN have been known as good tracers of star formation activities because they become abundant in the gas affected by shocks and high-energy UV photons.

5.2.4. *CS* J = 1–0

The I_{tot} variation of the CS line shows that α decreases as N_{H_2} increases, similar to what was seen for ^{13}CO and C^{18}O lines. However, the α values are generally greater than or similar to 1. Only the Ophiuchus cloud has α significantly smaller than 1 ($\alpha = 0.63$) when $\log(N_{H_2})$ exceeds 22.6.

Table 4 shows that the I_{tot} variation of CS can be explained with α of about 1.0 across the large N_{H_2} regime. In the ISF and L1641 regions, the N_{H_2} regimes with $\alpha \sim 1.0$ are extended over one order of magnitude. This result indicates that the I_{tot} of CS is proportional to N_{H_2} over the broad range of N_{H_2} in the Orion A cloud. Pety et al. (2017) also mentioned that CS $J = 2-1$ is one of the more useful column density tracers in the Orion B cloud.

5.2.5. *N$_2$H$^+$* J = 1–0

The N$_2$H$^+$ line increases superlinearly at low column densities before approaching a more linear growth at higher column densities. This behavior reflects the low abundance of this species in gas of low column density and high CO abundance. It makes it a good probe of gas column density for regions of relatively high column density.

The dominant formation mechanism of the N$_2$H$^+$ molecule is

$$H_3^+ + N_2 \rightarrow N_2H^+ + H_2. \quad (3)$$

When the CO abundance is close to 10^4, which is a typical value in MCs (Wilson & Rood 1994; van Dishoeck et al. 1995), H_3^+ mainly combines with CO to form HCO$^+$. Also, N$_2$H$^+$ is destroyed by combining with CO,

$$N_2H^+ + CO \rightarrow N_2 + HCO^+. \quad (4)$$

Therefore, the N$_2$H$^+$ line can be abundant in dense gas where CO is depleted from the gas phase (Bergin & Langer 1997;

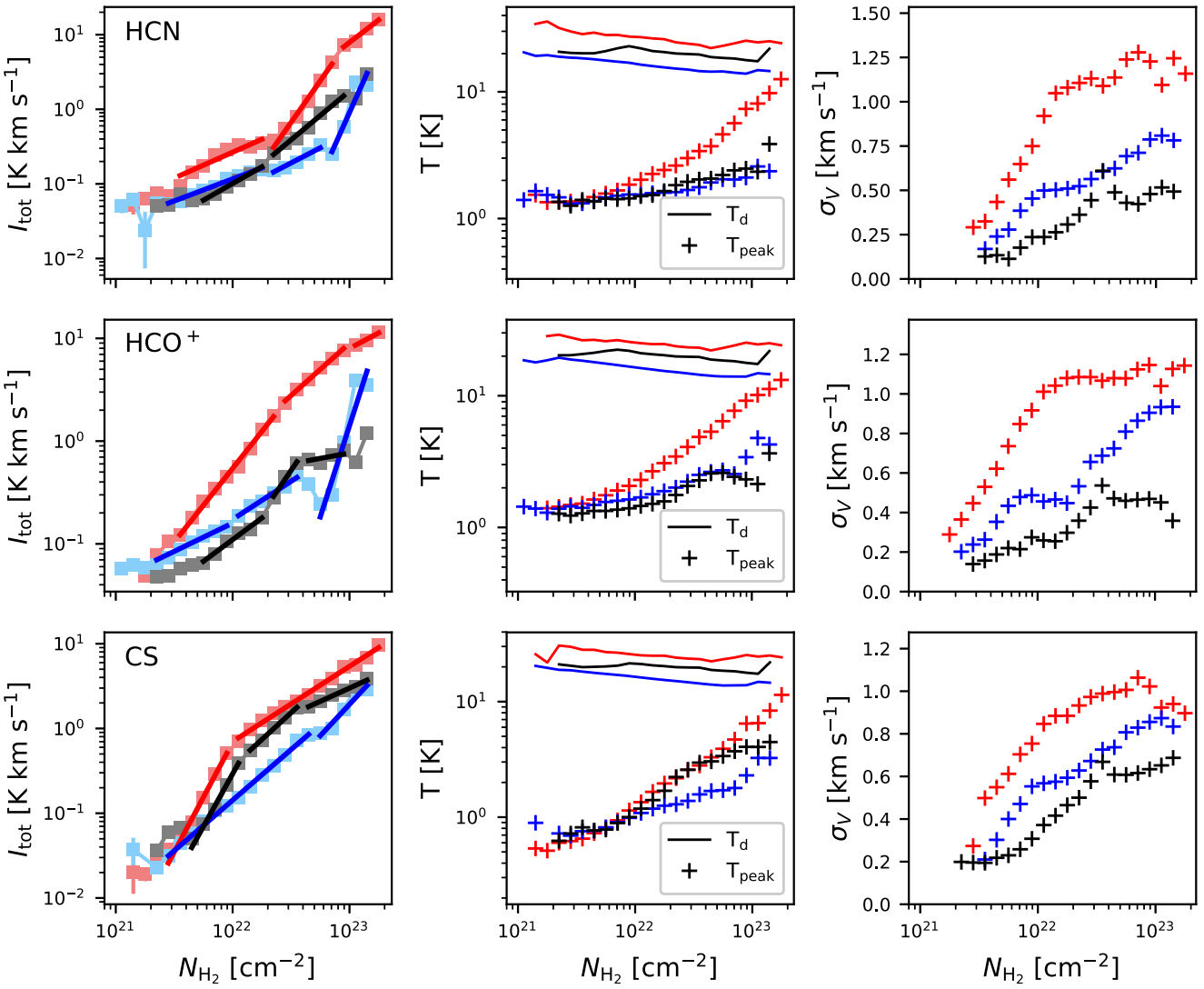

Figure 18. Same as Figure 17, but for the HCN (top), HCO^+ (middle), and CS (bottom) lines.

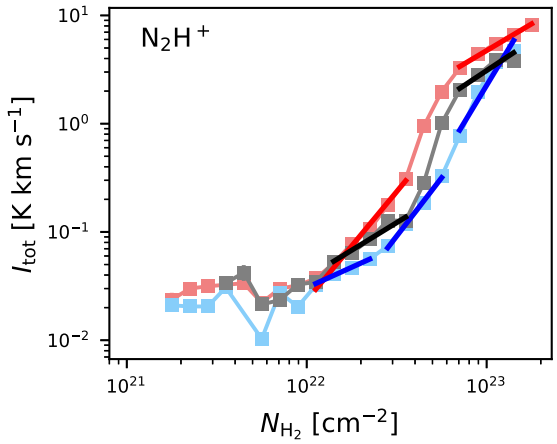

Figure 19. Same as the left panel of Figure 17, but for the N_2H^+ line.

Aikawa et al. 2001; Lee et al. 2003, 2004; Tatematsu et al. 2008). Therefore, I_{tot} of the N_2H^+ line represents the column density of the dense gas if we assume that the N_2H^+ line is optically thin.

Table 5
The N_{H_2} Regimes with $\alpha \sim 1.0$ in the ISF

Line	From Kauffmann et al. (2017)		This Work
	$\log(A_V)$ (mag)	$\log(N_{H_2})$[a] (cm^{-2})	$\log(N_{H_2})$[b] (cm^{-2})
^{13}CO	0.7–1.0	21.7–22.0	21.7–22.3
$C^{18}O$	1.0–1.3	22.0–22.3	22.2–22.8
HCN	0.7–1.4	21.7–22.4	22.9–23.3
N_2H^+	1.8–2.0	22.8–23.0	22.8–23.3

Notes.
[a] The column density is derived via an equation, $A_V/\mathrm{mag} = N_{H_2}/9.4 \times 10^{20}\,\mathrm{cm}^{-2}$ (Kauffmann et al. 2017).
[b] The N_{H_2} regimes in Table 4 are repeated for comparison.

The I_{tot} of the N_2H^+ line is proportional to the amount of cold and dense gas along the line of sight if the N_2H^+ line is optically thin. The mean I_{tot} value at a given N_{H_2} in the ISF region is slightly higher than that of the L1641 and Ophiuchus regions. This result implies that the amount of dense gas along the line of sight in the ISF region is slightly larger than that in

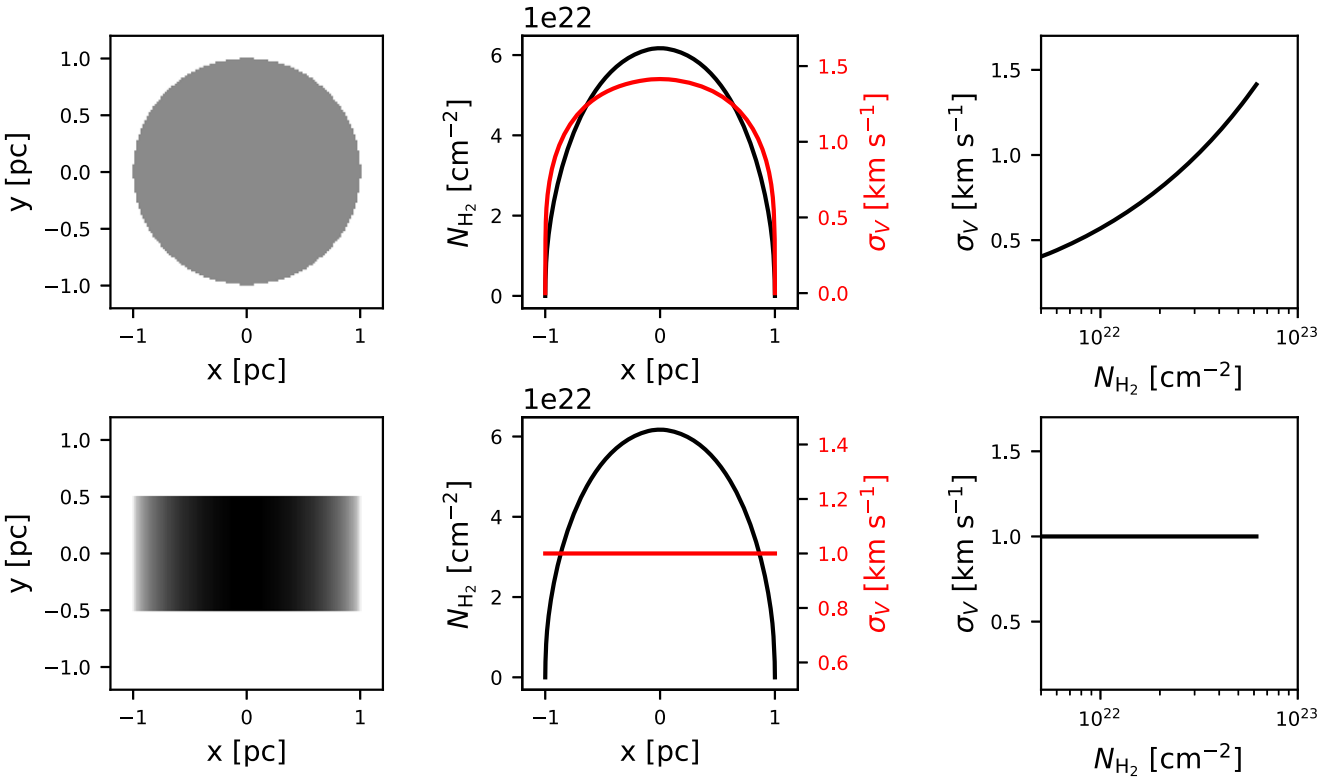

Figure 20. Cloud models with varying N_{H_2}. The top and bottom panels describe the cylindrical and the slab-like cloud models, respectively. The z-axis in the model clouds is located along the plane of sky, and thus the y-axis is the line of sight. The left panels show the cross sections of the model clouds assuming that we observe the clouds along the y-axis. The middle panels present the variation of N_{H_2} (black) and σ_V (red) along the x-axis. The right panels show the relation between σ_V and N_{H_2} for the model clouds. A uniform density of 10^4 cm^{-3} is assumed for the cylindrical model. The density structure within the slap-like model is adjusted to have the N_{H_2} distribution the same as that of the cylindrical model (see the middle panels). The σ_V for a given x is derived assuming the burger spectrum ($\sigma_V \propto l^{0.5}$), which describes the velocity field of shock-dominated turbulence.

the L1641 and Ophiuchus regions. Tatematsu et al. (2008) also mentioned that the abundance of N_2H^+ decreases toward the south in the ISF. Therefore, the difference in I_{tot} of N_2H^+ also can be explained with an abundance difference between the regions.

5.3. Variation of Velocity Dispersion with Column Density

The right panels of Figures 17 and 18 display the rms velocity dispersion (moment 2; σ_V) versus N_{H_2}. The dispersion depends strongly on N_{H_2}, increasing by factors of 3–5, depending on the lines and regions. Weak lines can produce unrealistically small values of σ_V, but we have tried to avoid that by using the moment-masking method to make the σ_V map and by adopting the average values weighted by the inverse of the square of the uncertainty. Consequently, we believe that the strong trends in σ_V versus N_{H_2} are real.

Two simple cloud models can be adopted to describe the increasing N_{H_2} toward the center from the outer region: (1) a structure with a varying depth, like a cylinder with a uniform density located along the sky plane, and (2) a structure with a uniform depth, such as a slab with varying density, as illustrated in Figure 20. The observed line width is determined by sampling a turbulent velocity field along the line of sight (y-direction). If the line width correlates with path length, as expected from the turbulent velocity field (Larson 1981; Solomon et al. 1987; Heyer & Schloerb 1997; Klessen 2000), the σ_V increases with N_{H_2} in the cylindrical model, while that remains constant in the slab-like model. This result suggests that the cylinder cloud model can explain the low-N_{H_2} edges of the cloud with low σ_V, unlike the slab-like cloud model.

5.4. Line Luminosities and Luminosity Ratios

The line luminosity of each line in the Orion A and Ophiuchus clouds is calculated by

$$L_{line} = D^2\ \theta_{pix}^2 \sum_{I_{tot.pix}}^{N_{pix}}, \quad (5)$$

where D, θ_{pix}, N_{pix}, and $I_{tot.pix}$ are the distance, angular size of a pixel (20″), number of pixels, and line-integrated intensity per pixel, respectively. The $I_{tot.pix}$ is defined as

$$I_{tot.pix} = \frac{\theta_{pix}^2}{2\pi \left(\frac{\theta_{beam}}{2\sqrt{2\ln(2)}}\right)^2} I_{tot}, \quad (6)$$

where θ_{beam} is the beam size. The distance to the Orion A cloud is assumed to be 416.3 pc, which is the average of the distances to the Orion nebular cluster, L1641, and L1647 (389, 417, and 443 pc, respectively; Kounkel et al. 2018). For the Ophiuchus cloud, we adopted 137 pc (Ortiz-León et al. 2017).

The value of N_{pix} requires discussion. We have done the summation in two ways. In the first, only the pixels that in the moment-masked map of each line were included. Very weak emission extended over large areas can, however, contribute substantially to the line luminosity (Evans et al. 2020). For a

Table 6
Total Line Luminosities Relative to $L_{^{13}CO}$ and Luminosity Ratios

Cloud	$L_{^{13}CO}$	$L_{C^{18}O}$	L_{HCN}	L_{HCO^+}	$L_{N_2H^+}$	L_{CS}	$L_{^{13}CO}/L_{C^{18}O}$	L_{HCO^+}/L_{HCN}
Orion A	1.000	0.039	0.025	0.036	0.005	0.030	25.673	1.458
Orion A (unbiased)	1.000	0.049	0.030	0.036	0.005	0.040	20.475	1.179
Ophiuchus	1.000	0.076	0.009	0.009	0.004	0.029	13.180	0.987
Ophiuchus (unbiased)	1.000	0.089	0.055	0.056	−0.001	0.035	11.236	1.007

comparison to other galaxies where all the emission is included in a beam, we need to include that emission. We did that by including all pixels in the original spectral maps. The resulting values are denoted by "unbiased" in Table 6. The comparison of the two values confirms that regions where individual lines are not clearly detected nonetheless add substantial luminosity to some lines, especially HCN and HCO^+ in Ophiuchus. The drawback of including all pixels is that baseline subtraction must be very good to avoid systematic offsets; an example is the negative luminosity of N_2H^+ from the unbiased method. That line is clearly very concentrated with no contribution from very extended regions.

Table 6 presents the ratios of the total line luminosities to that of the ^{13}CO line, which has the highest line luminosity in both clouds; the total line luminosities of the ^{13}CO line in the Orion A and Ophiuchus clouds are 290.3 and 10.9 K km s^{-1} pc^2, respectively. The total line luminosities of the $C^{18}O$, HCN, HCO^+, and CS lines are all lower than 10% of the ^{13}CO luminosity. The line ratios follow similar patterns in the two clouds. However, as mentioned above, the luminosities derived from the moment-masked maps of HCO^+ and HCN are much smaller than those from unbiased maps, indicative of the extended weak HCO^+ and HCN emission.

The ^{13}CO-to-$C^{18}O$ and HCO^+-to-HCN luminosity ratios are also given in Table 6. The ^{13}CO-to-$C^{18}O$ and HCO^+-to-HCN luminosity ratios have been used to study the properties of galaxies (Krips et al. 2008; Jiménez-Donaire et al. 2017; Méndez-Hernández et al. 2020). The ^{13}CO-to-$C^{18}O$ ratios are much larger than those for starburst (3.4 ± 0.9) and normal spiral galaxies (6.0 ± 0.9; Jiménez-Donaire et al. 2017). Méndez-Hernández et al. (2020) found a ^{13}CO-to-$C^{18}O$ ratio of 2.5 ± 0.6 with the stacked spectra of 24 galaxies. The weak detection of the $C^{18}O$ line could cause a large uncertainty in the ratio. The observation of the $C^{18}O$ line in galaxies with better sensitivities is needed to confirm this difference.

The HCO^+-to-HCN ratio for galaxies has been used to distinguish the phenomena in galaxies, such as an active galactic nucleus (AGN) and starburst. The HCO^+-to-HCN ratios for the AGN-dominated galaxies that were studied by Krips et al. (2008) are about 0.66, increasing to about 1.5 as the contribution of the starburst increases. The ratio in Orion A (1.2–1.5) is similar to that for starbursts, while that in Ophiuchus (1.0) is intermediate between those of AGNs and those of starbursts.

6. Summary

We obtained large and homogeneous line maps of the Orion A and Ophiuchus clouds in six different molecular transitions as one of the TRAO-KSPs, TIMES. Both clouds were mapped in ^{13}CO $J = 1-0$/$C^{18}O$ $J = 1-0$, HCN $J = 1-0$/HCO^+ $J = 1-0$, and N_2H^+ $J = 1-0$/CS $J = 2-1$ using the TRAO 13.7 m telescope. The areas of mapped regions were 8.7 and 3.9 deg^2 toward the Orion A and Ophiuchus clouds, respectively, with $\sim 50''$ beam size. We discussed the physical and chemical environments traced by the observed lines in both clouds. The main results are summarized as follows:

1. The observed ^{13}CO line traces relatively diffuse gas in the MCs. For the Orion A cloud, there are a large-scale north–south velocity gradient and complex velocity structures. For the Ophiuchus cloud, the L1688 and L1709 regions have different velocities and generally show random motions. The Ophiuchus cloud is kinematically quiescent compared to the Orion A cloud.
2. The $C^{18}O$ line traces high column density regions, which are potentially the birthplace of the stars. The emission-line maps show clumpy structures, and their spatial distribution is well correlated with that of the young embedded protostars.
3. The N_2H^+ line traces cold and dense clumps/cores in the observed clouds. These clumps/cores seem to be embedded in the clumps that are revealed by the $C^{18}O$ line.
4. The CS $J = 2-1$ line traces the broadest range of the column density (over one order of magnitude), making it a good probe of column density in MCs.
5. The HCN and HCO^+ lines trace the gas affected by the active star-forming activities. In the Orion A cloud, both emission lines coexist in the ISF, the active star-forming clusters (L1641-N, L1641-C, L1641-S cluster), and nearby the HH objects. In the Ophiuchus cloud, however, the HCN line is mainly detected toward Oph-A and Oph-B, while the HCO^+ line is emitted from Oph-C, Oph-E, and Oph-F.
6. The high-velocity wing structures are marginally detected in the $C^{18}O$ line spectrum obtained toward the OMC-1. The N_2H^+ lines do not have high-velocity wings.
7. The velocity dispersions all increase strongly with column density, suggesting that the edges of the cloud are largely defined by small path length, not just low volume density.
8. The ^{13}CO-to-$C^{18}O$ line luminosity ratios for the Orion A and Ophiuchus clouds are much larger than that of starburst galaxies, while the HCO^+-to-HCN ratios are comparable to that of the starburst galaxies.

In a companion paper (Yun et al. 2021), we use the TIMES data to explore the relationship between turbulence and star formation activity in MCs. We apply principal component analysis (PCA; Heyer & Schloerb 1997; Brunt & Heyer 2013), which is one of the statistical methods used to derive the low-order velocity structure function, to the spectral maps presented in this paper. The uniform coverage, sensitivity, and range of

gas tracers included in the TIMES program are ideal for studying MC kinematics and turbulence.

This work was supported by the National Research Foundation of Korea (NRF) grant funded by the Korean government (MSIT) (grant No. 2021R1A2C1011718). S.L. was also supported by NAOJ ALMA Scientific Research grant No. of 2018-10B.

Appendix A
Moment 0, 1, and 2 Maps for the Orion A Cloud

We generated the moment maps for each of the $C^{18}O$, HCN, HCO^+, N_2H^+, and CS lines in the Orion A cloud through the method described in Section 3. Figures A1–A5 present the I_{tot} maps, and Figures A6–A15 present the V_{lsr} and σ_V maps of each line.

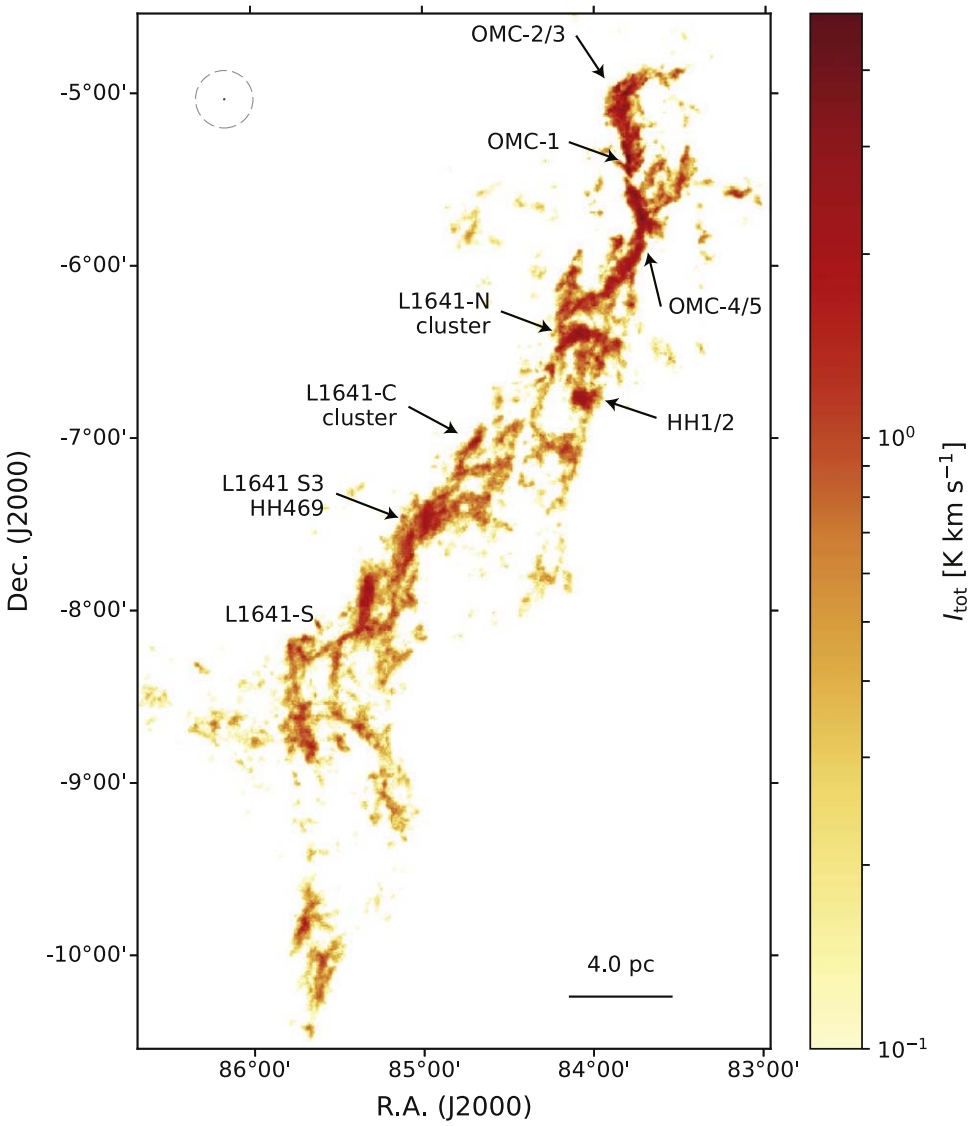

Figure A1. Same as Figure 2, but for the $C^{18}O$ line. We annotated the $C^{18}O$ map with the names of the associated sources (Davis et al. 2009; Mairs et al. 2016; Meingast et al. 2016).

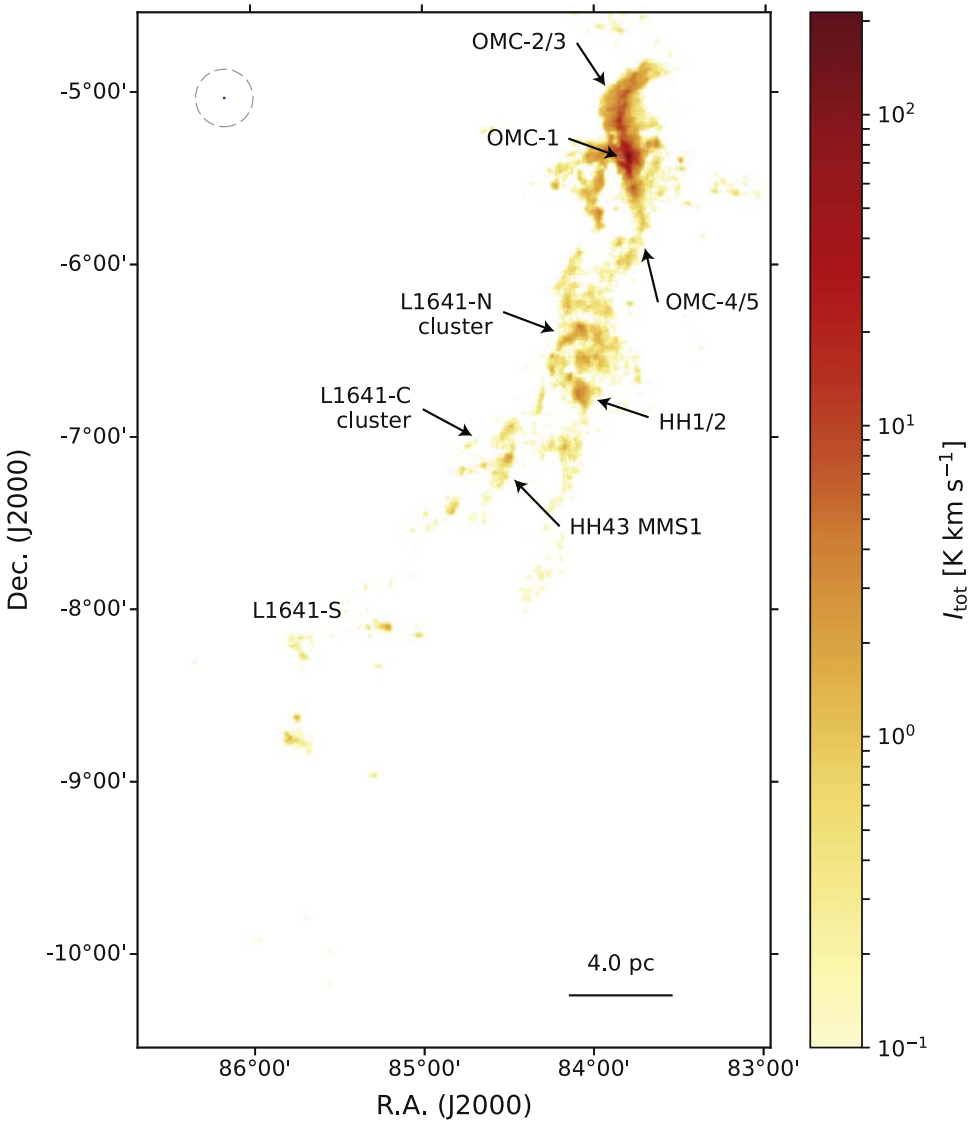

Figure A2. Same as Figure 2, but for the HCN line. We annotated the map with the names of the associated sources (Davis et al. 2009; Mairs et al. 2016; Meingast et al. 2016).

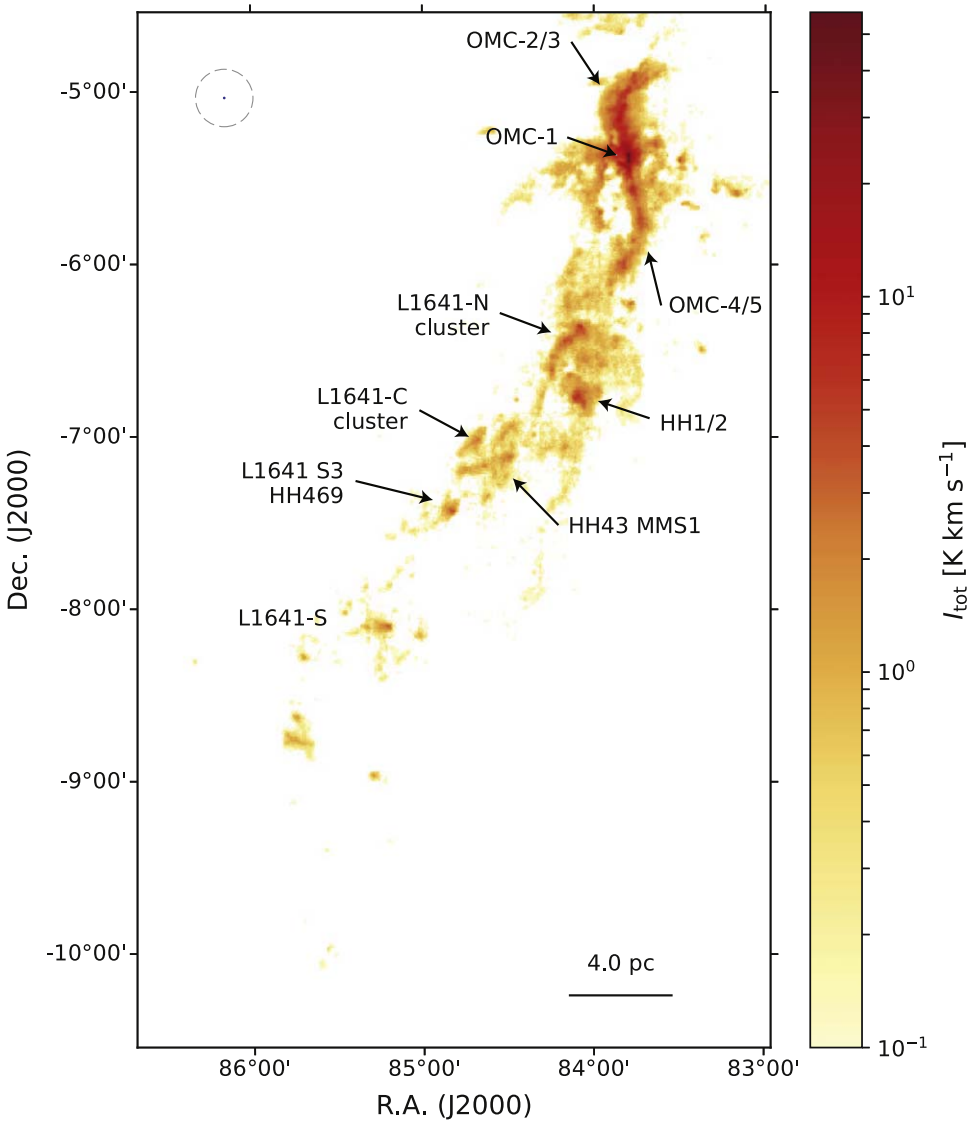

Figure A3. Same as Figure 2, but for the HCO^+ line. We annotated the map with the names of the associated sources (Davis et al. 2009; Mairs et al. 2016; Meingast et al. 2016).

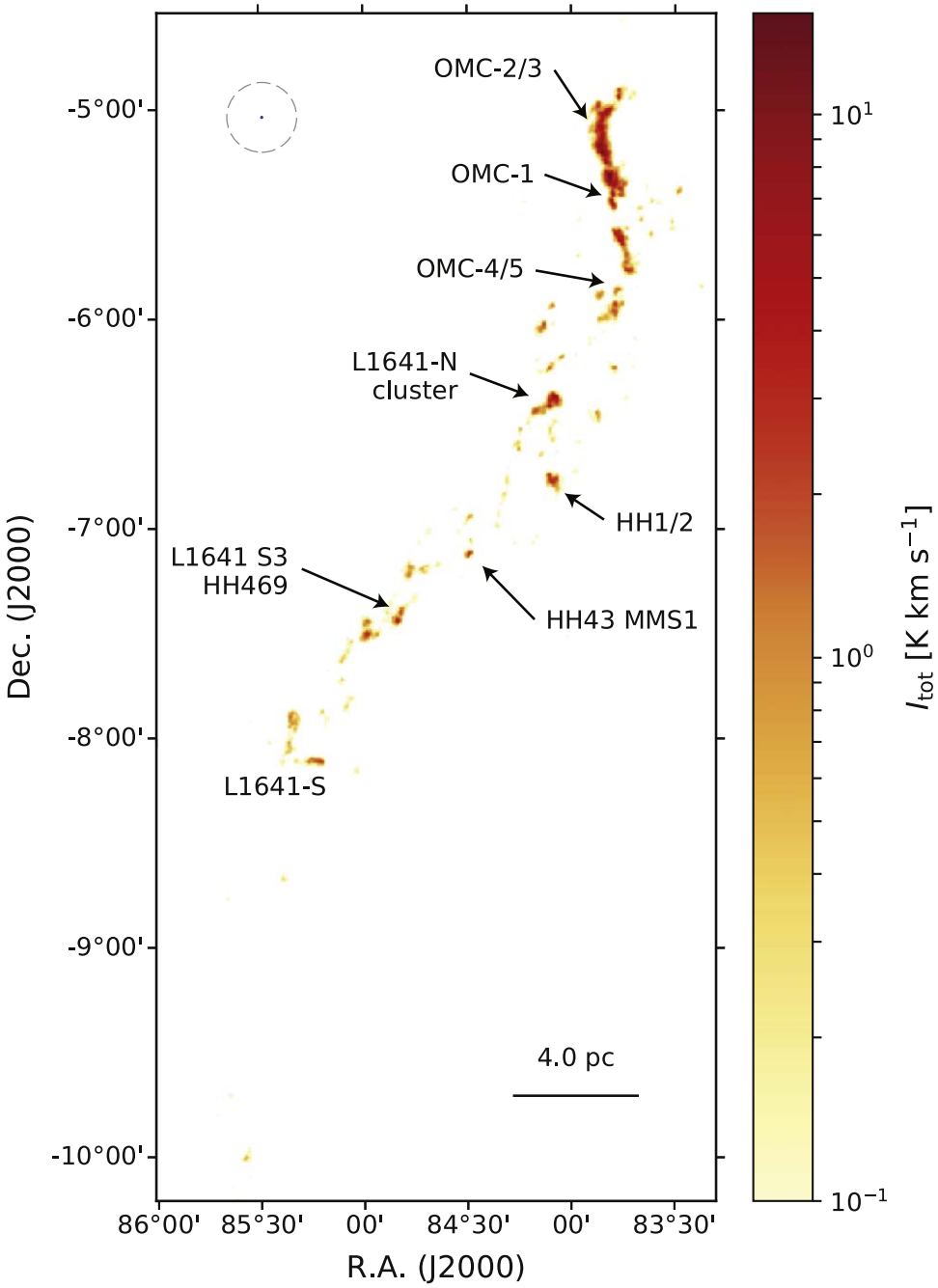

Figure A4. Same as Figure 2, but for the N_2H^+ line. We annotated the map with the names of the associated sources (Davis et al. 2009; Mairs et al. 2016; Meingast et al. 2016).

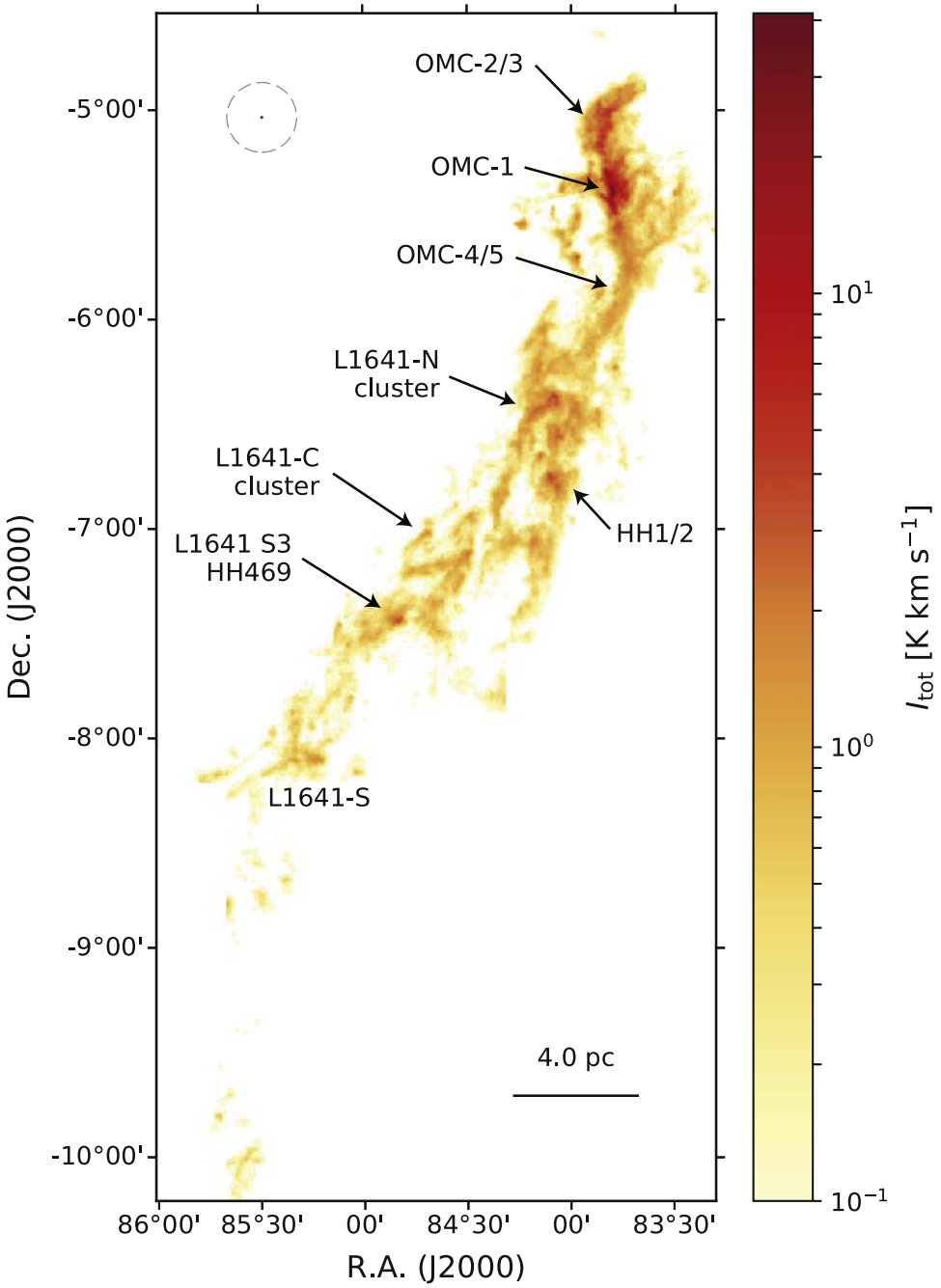

Figure A5. Same as Figure 2, but for the CS line. We annotated the map with the names of the associated sources (Davis et al. 2009; Mairs et al. 2016; Meingast et al. 2016).

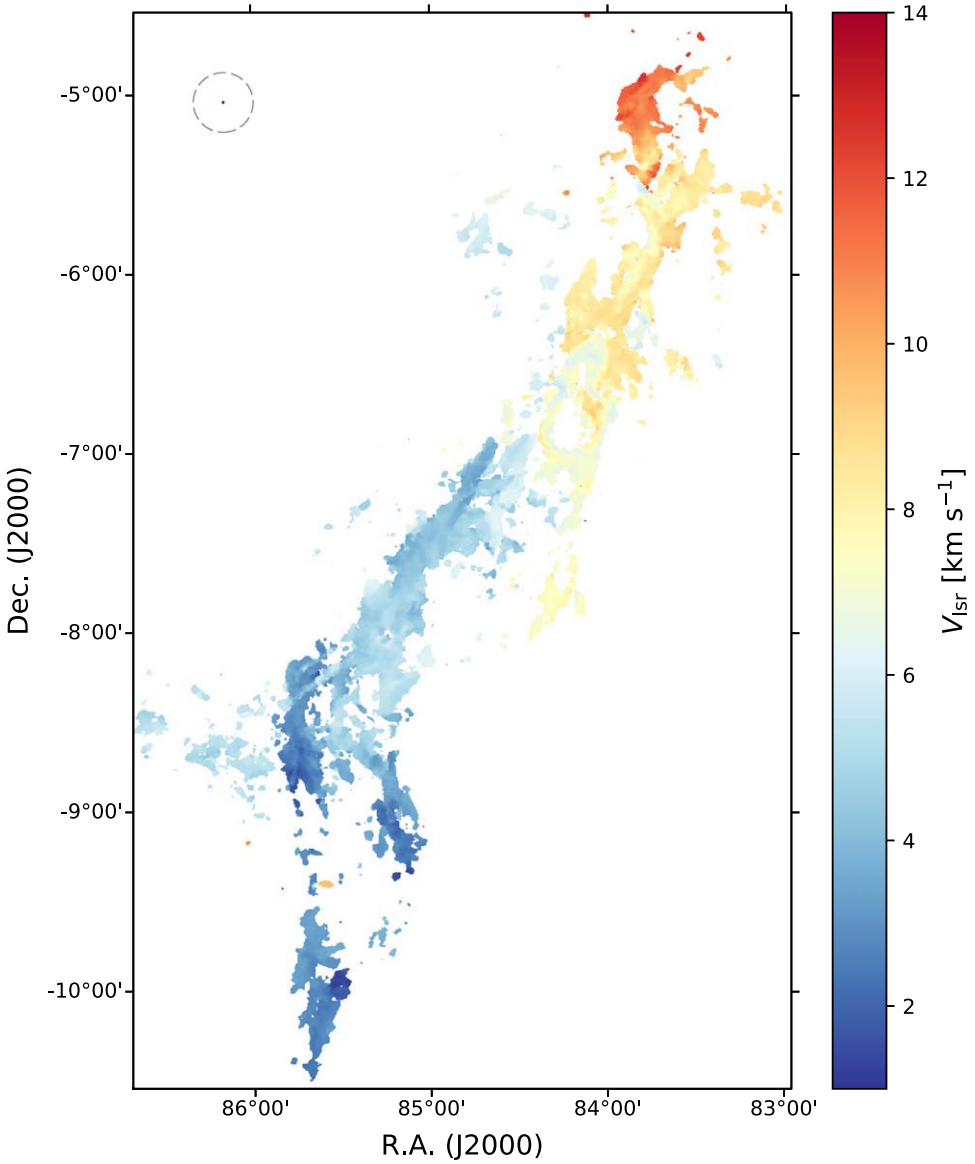

Figure A6. Same as Figure 4, but for the C^{18}O line. The color scale of the V_{lsr} map is the same as that of the ^{13}CO line (Figure A6).

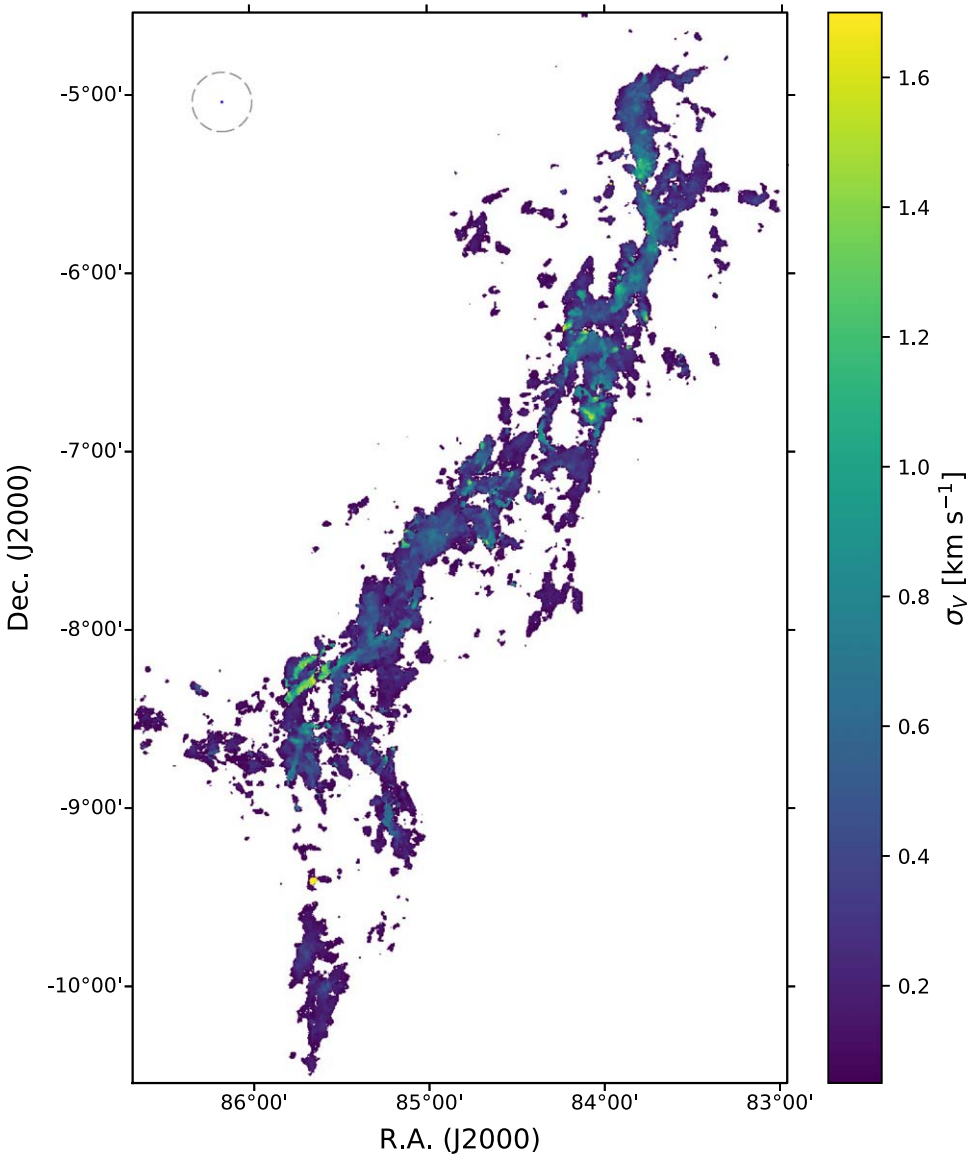

Figure A7. Same as Figure 5, but for the $C^{18}O$ line.

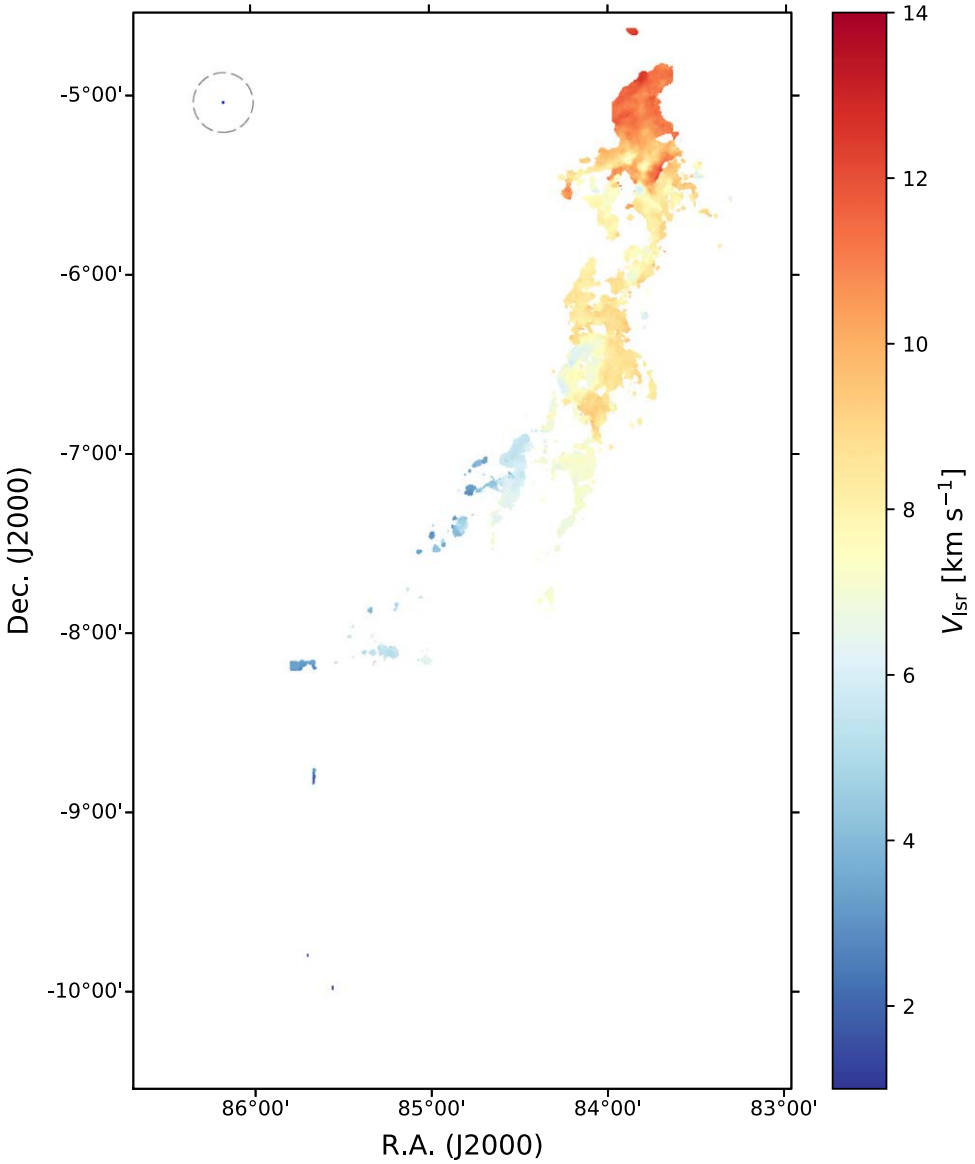

Figure A8. Same as Figure 4, but for the HCN line.

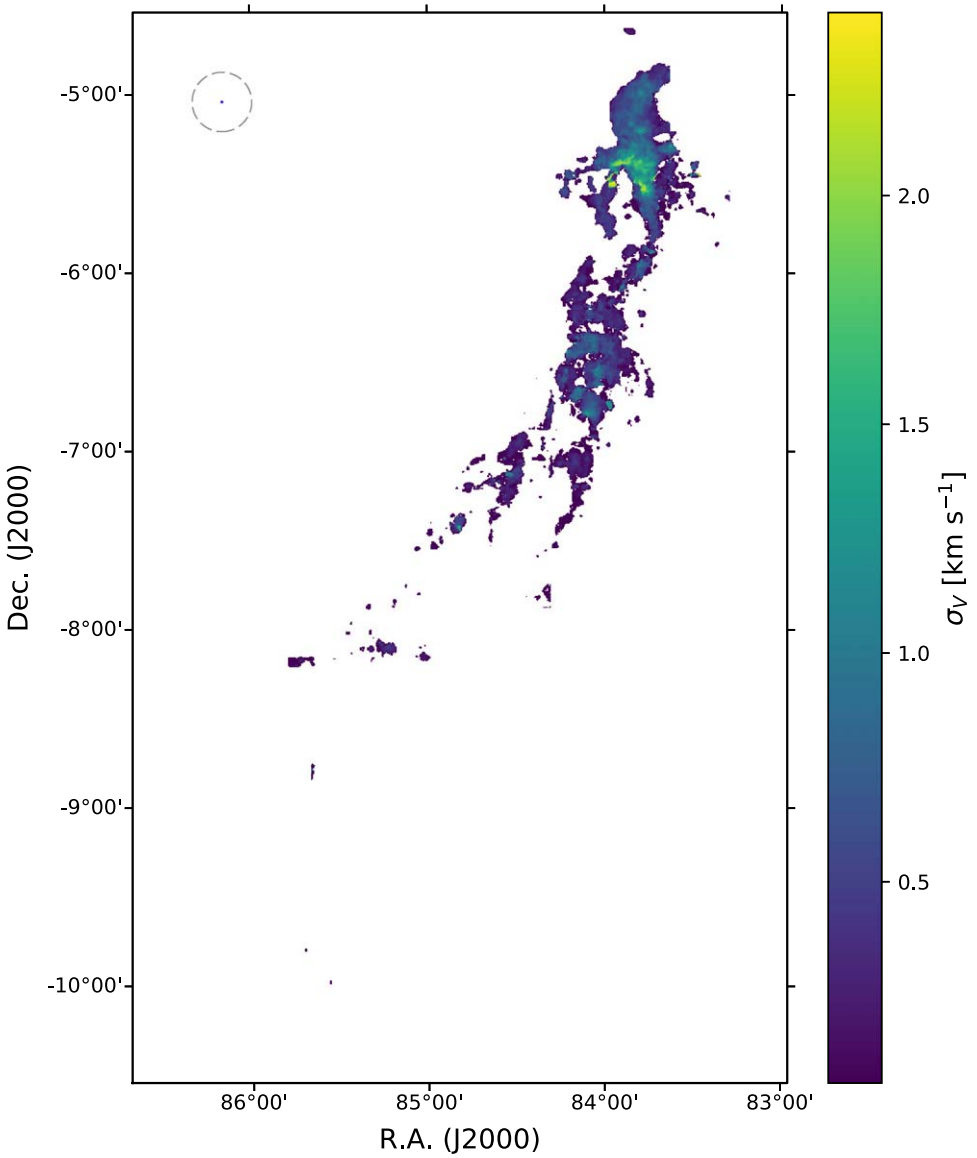

Figure A9. Same as Figure 5, but for the HCN line. Note that the σ_V of the HCN line near the ISF would be underestimated (see Section 3 for more details).

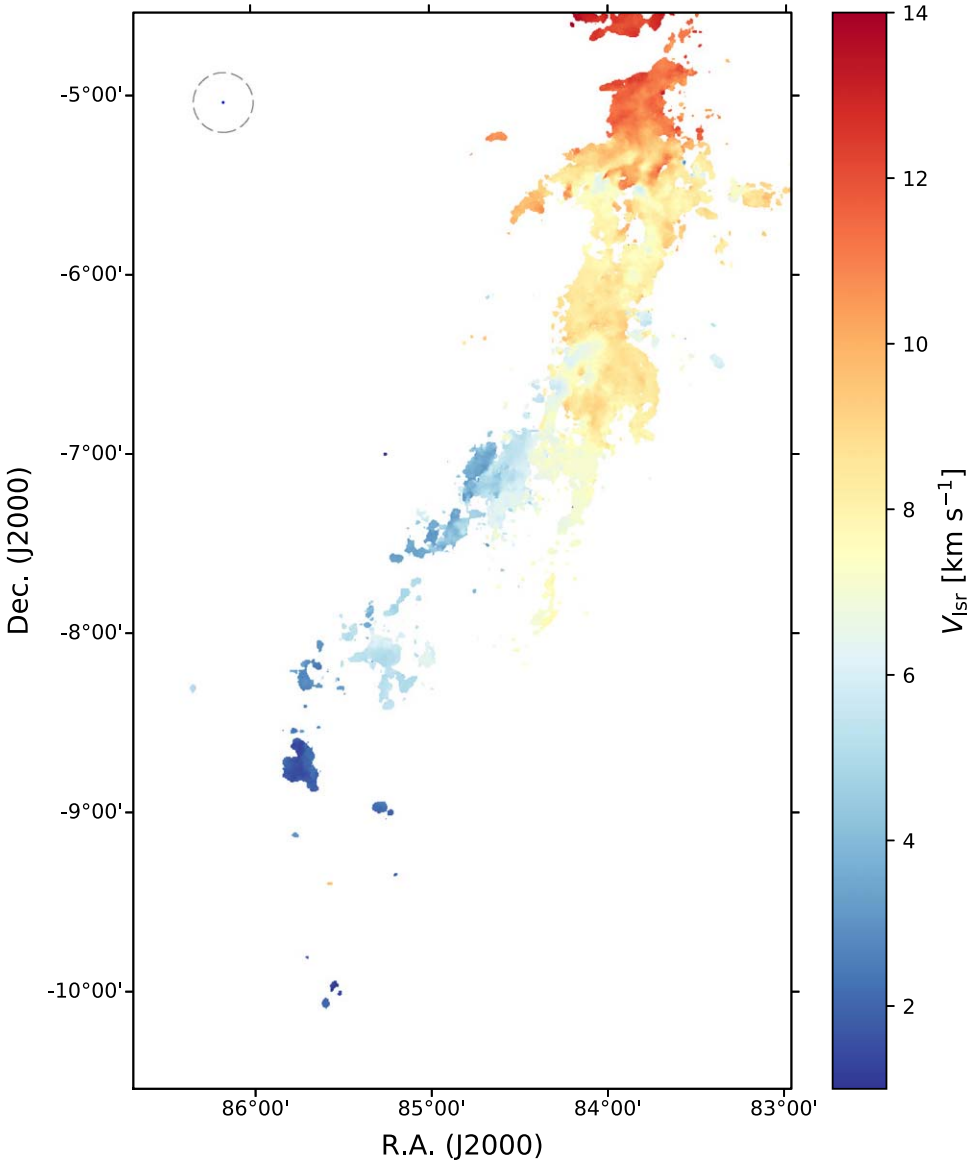

Figure A10. Same as Figure 4, but for the HCO^+ line.

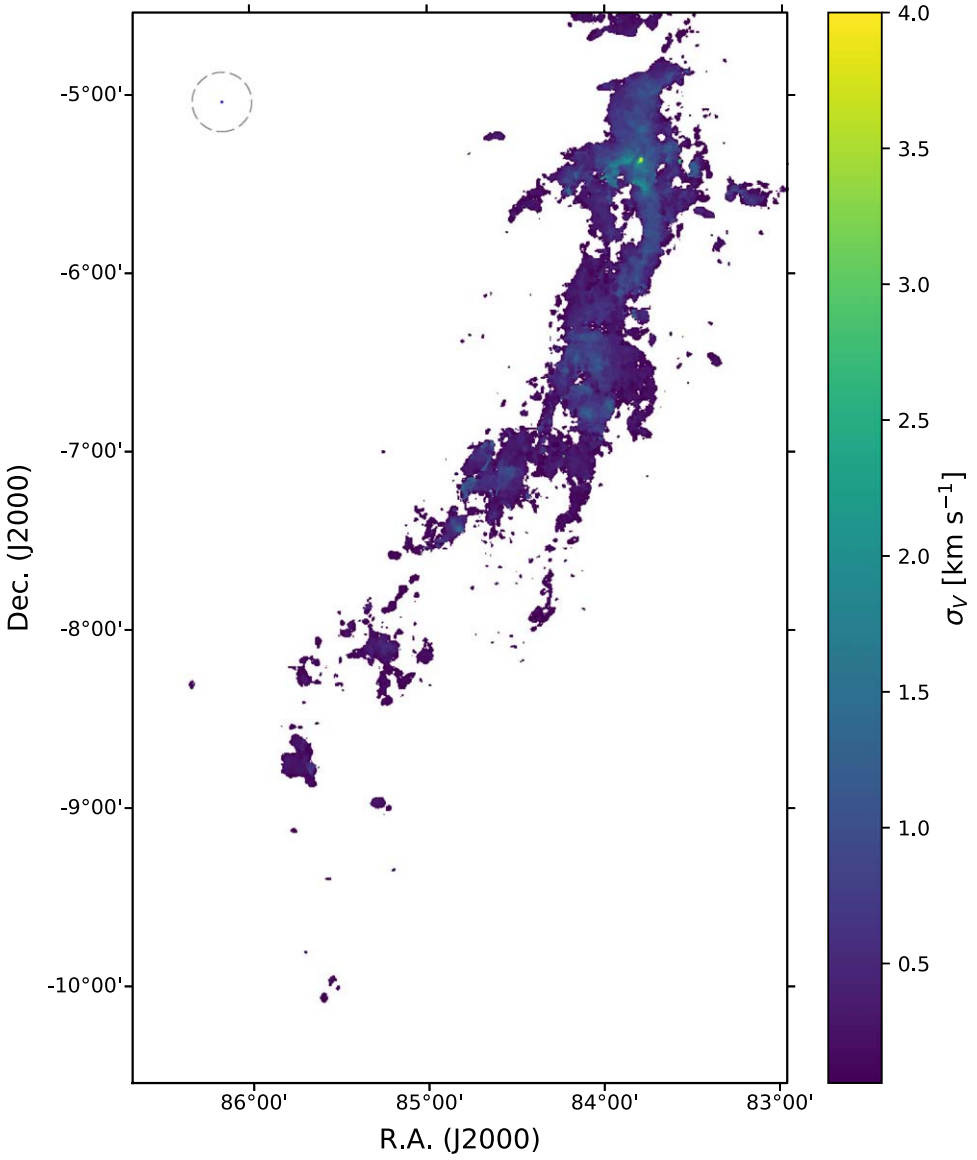

Figure A11. Same as Figure 5, but for the HCO^+ line.

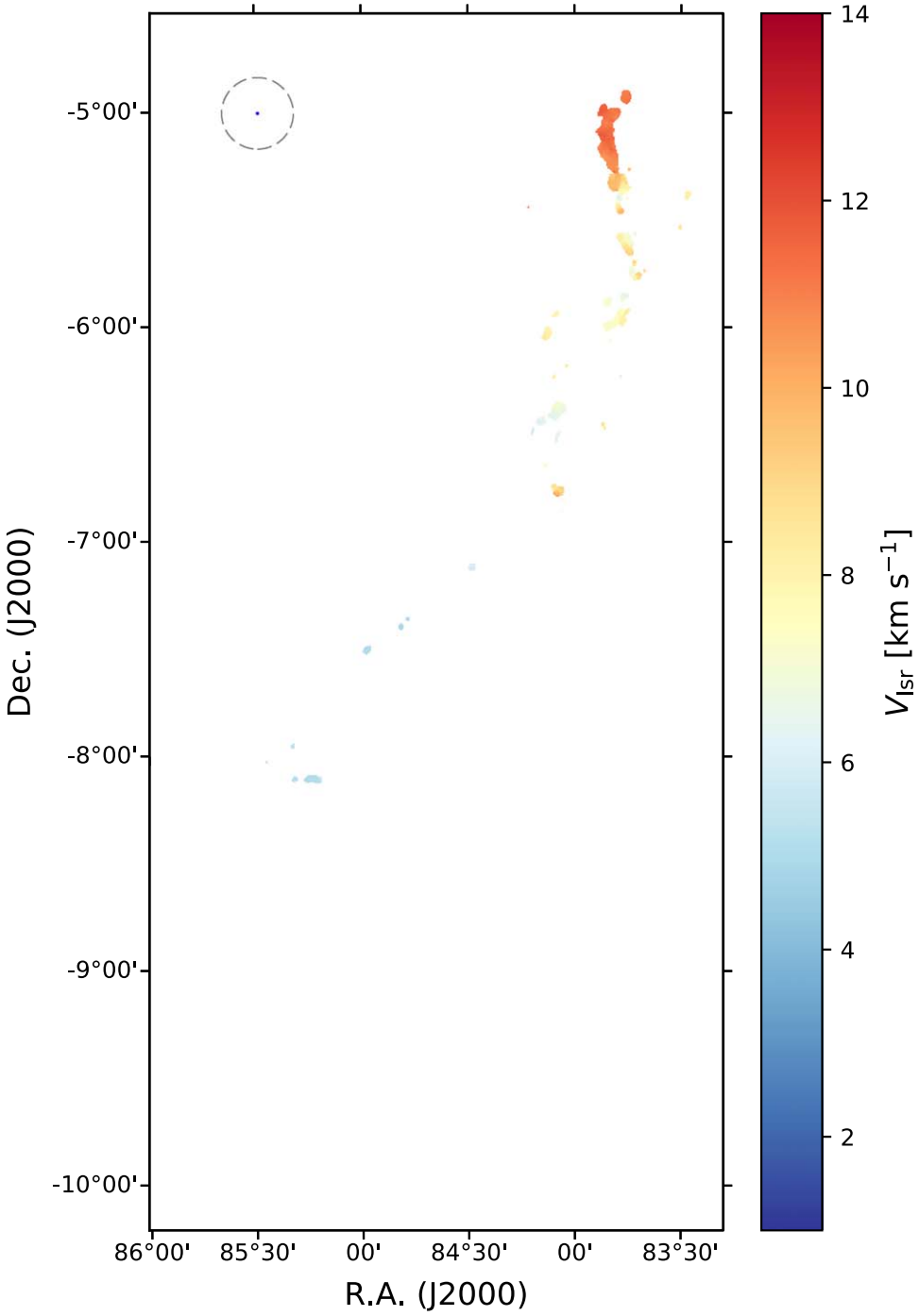

Figure A12. Same as Figure 4, but for the N_2H^+ line.

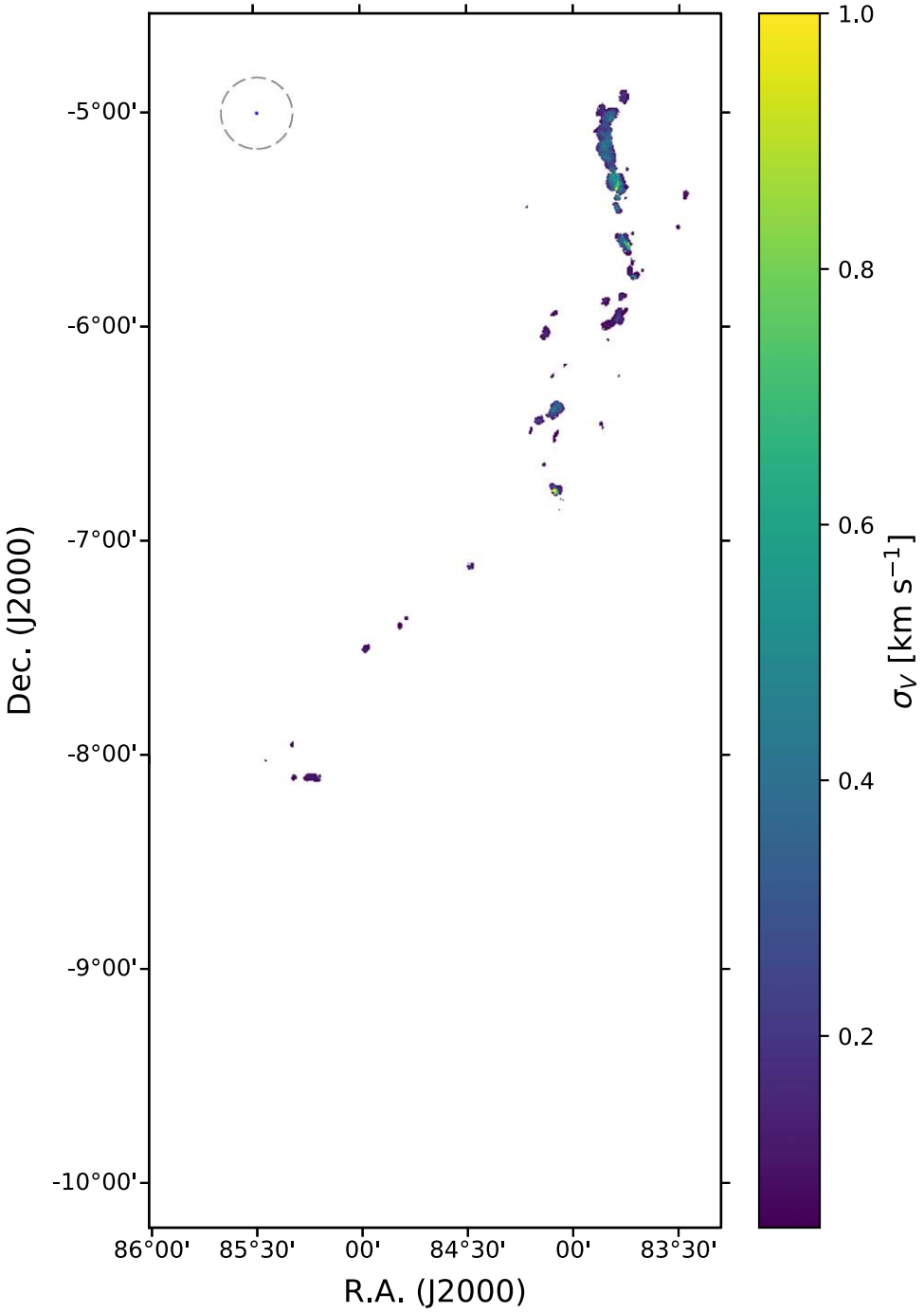

Figure A13. Same as Figure 5, but for the N_2H^+ line.

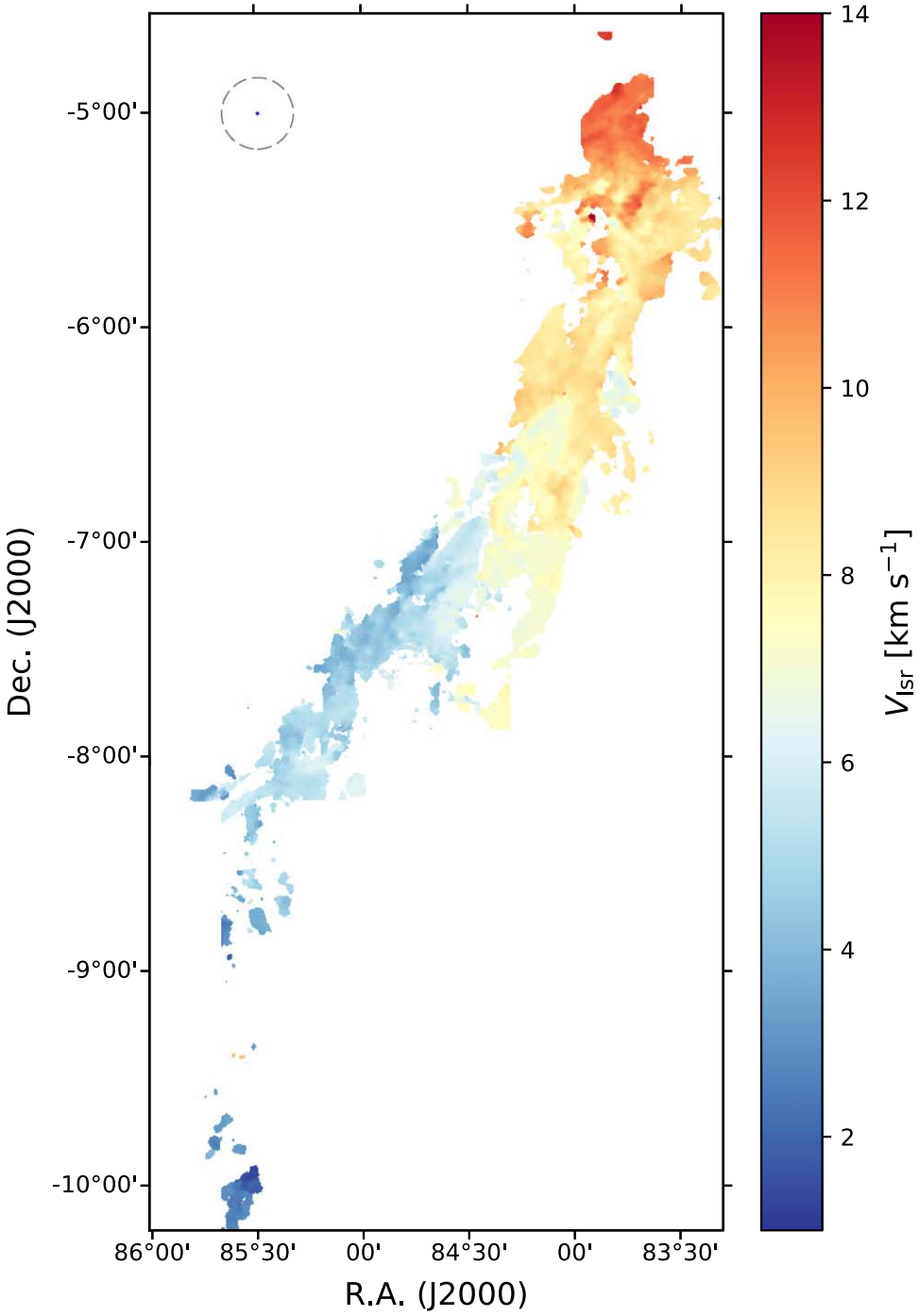

Figure A14. Same as Figure 4, but for the CS line.

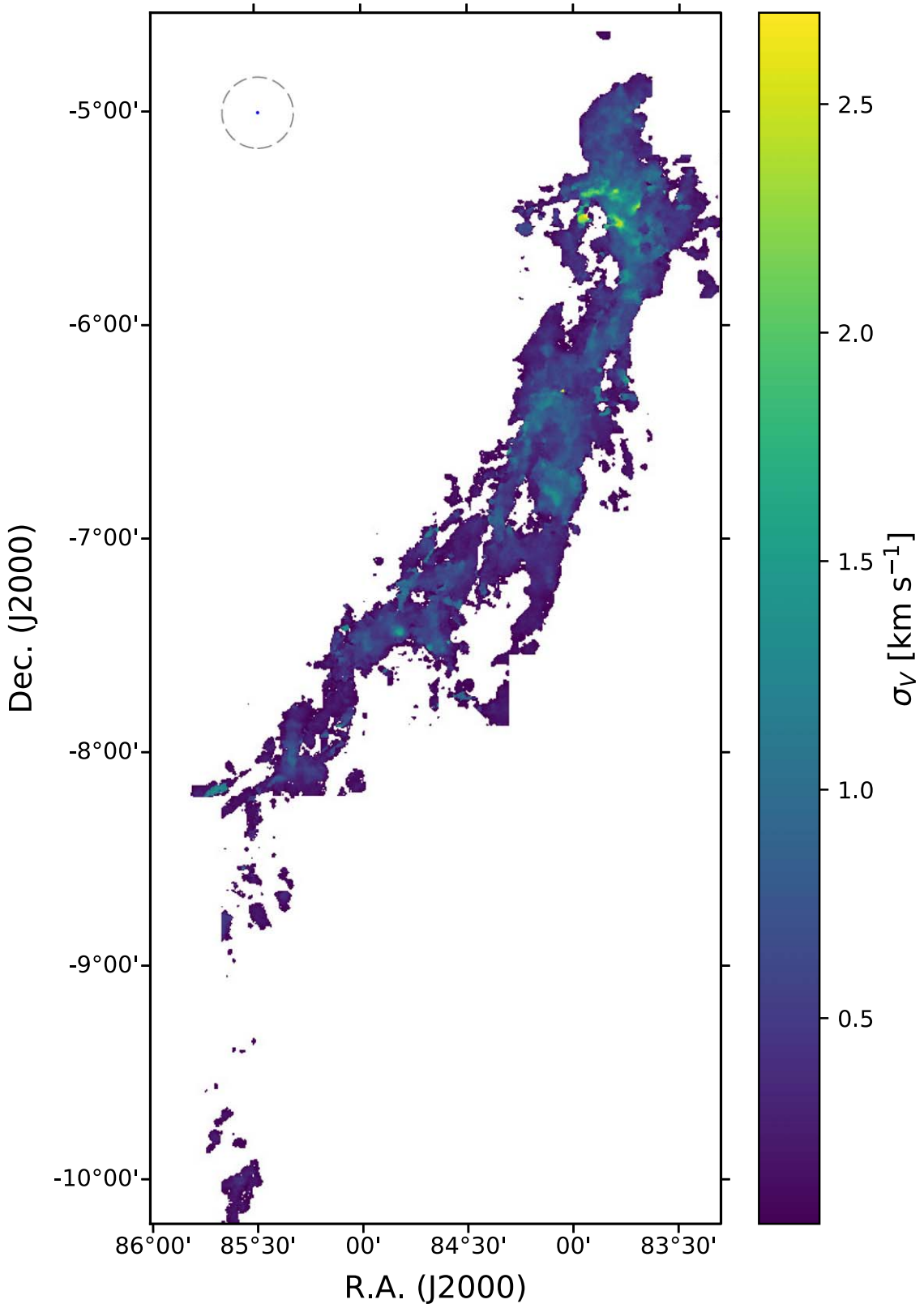

Figure A15. Same as Figure 5, but for the CS line.

Appendix B
Moment 0, 1, and 2 Maps for the Ophiuchus Cloud

The moment maps of the $C^{18}O$, HCN, HCO^+, N_2H^+, and CS lines in the Ophiuchus cloud were generated through the same method that was applied to the Orion A data. Figures B1–B5 present the I_{tot} maps, and Figures B6–B15 present the V_{lsr} and σ_V maps of each line.

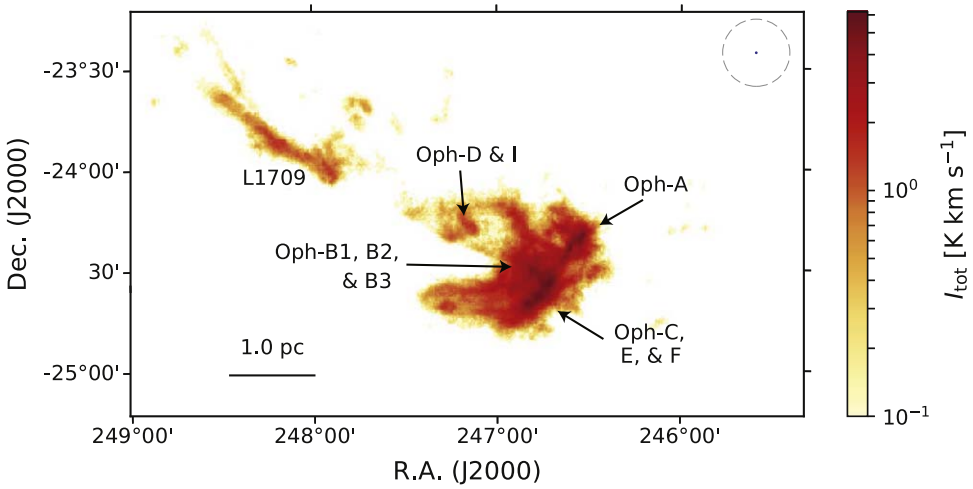

Figure B1. Same as Figure 3, but for the $C^{18}O$ line. The sources associated with the observed line are marked (Lynds 1962; Loren 1989a; Loren et al. 1990; Pan et al. 2017).

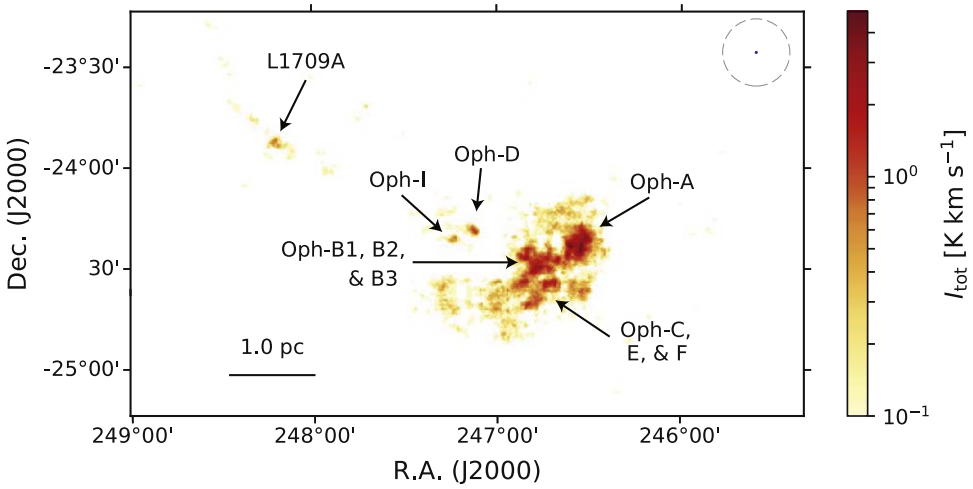

Figure B2. Same as Figure 3, but for the HCN line. The sources associated with the observed line are marked (Lynds 1962; Loren 1989a; Loren et al. 1990; Pan et al. 2017).

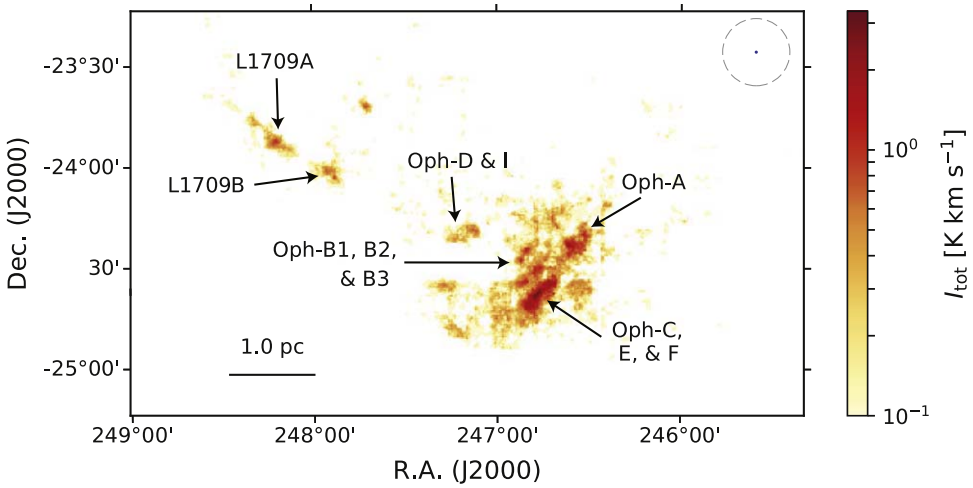

Figure B3. Same as Figure 3, but for the HCO^+ line. The sources associated with the observed line are marked (Lynds 1962; Loren 1989a; Loren et al. 1990; Pan et al. 2017).

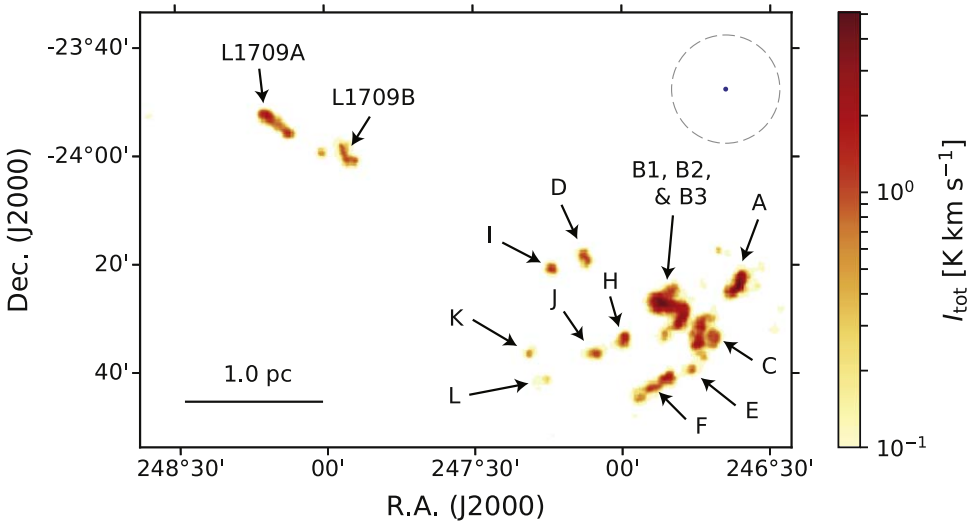

Figure B4. Same as Figure 3, but for the N_2H^+ line. The names of the associated cores are marked (Lynds 1962; Loren 1989a; Loren et al. 1990; Pan et al. 2017).

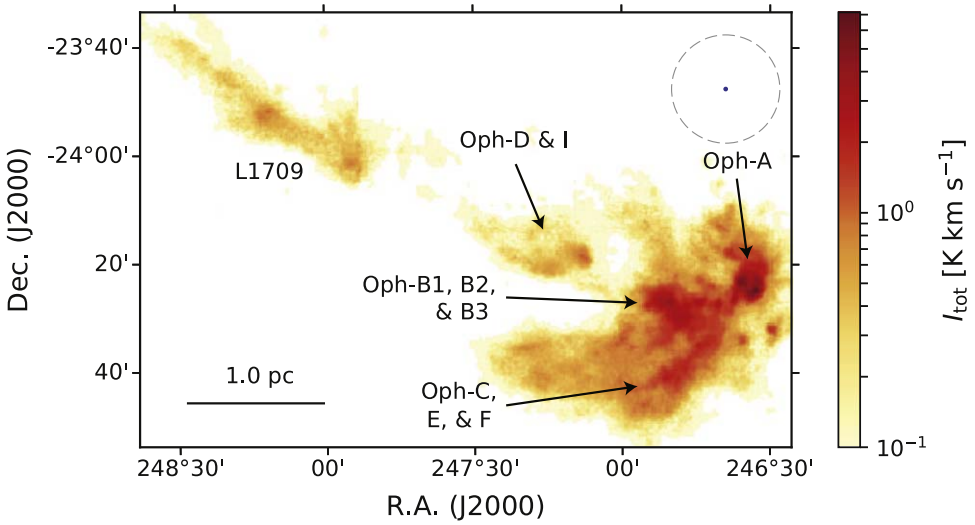

Figure B5. Same as Figure 3, but for the CS line. The sources associated with the observed line are marked (Lynds 1962; Loren 1989a; Loren et al. 1990; Pan et al. 2017).

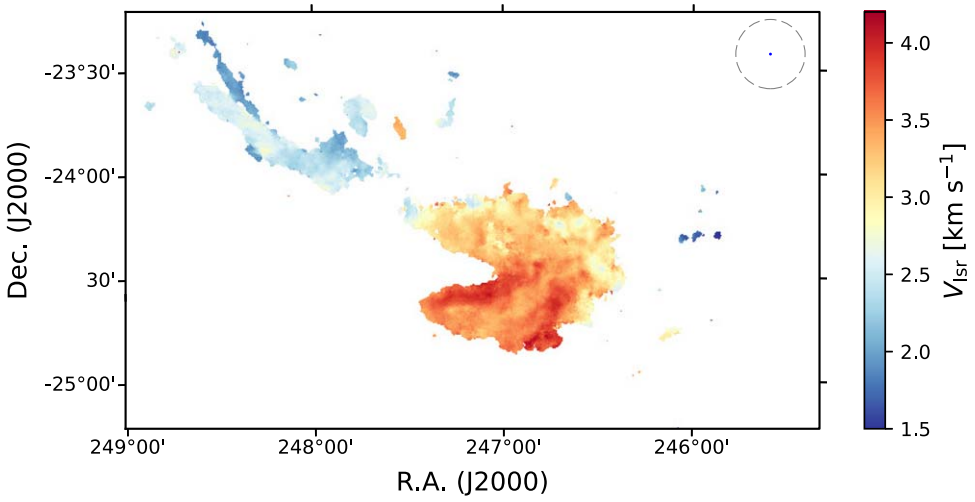

Figure B6. Same as Figure 6, but for the $C^{18}O$ line. The color scale of the map is the same as that of the ^{13}CO line (Figure 6).

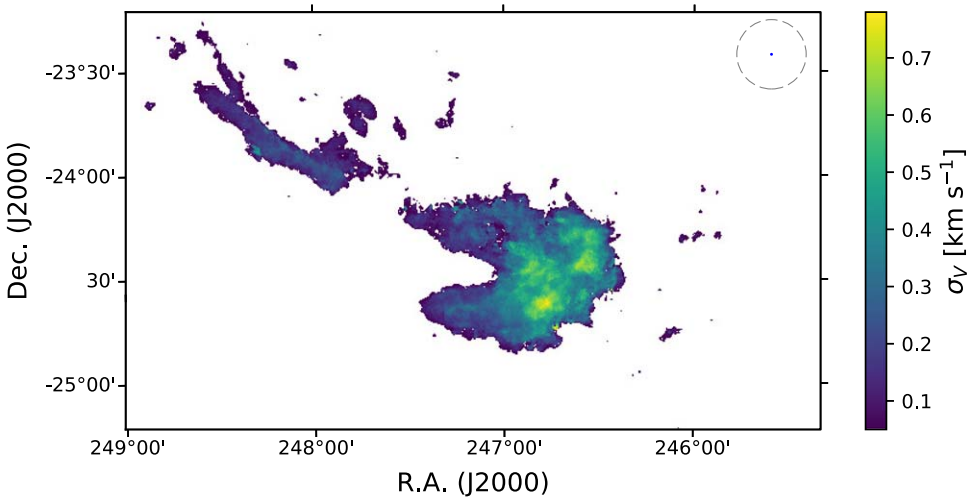

Figure B7. Same as Figure 7, but for the $C^{18}O$ line.

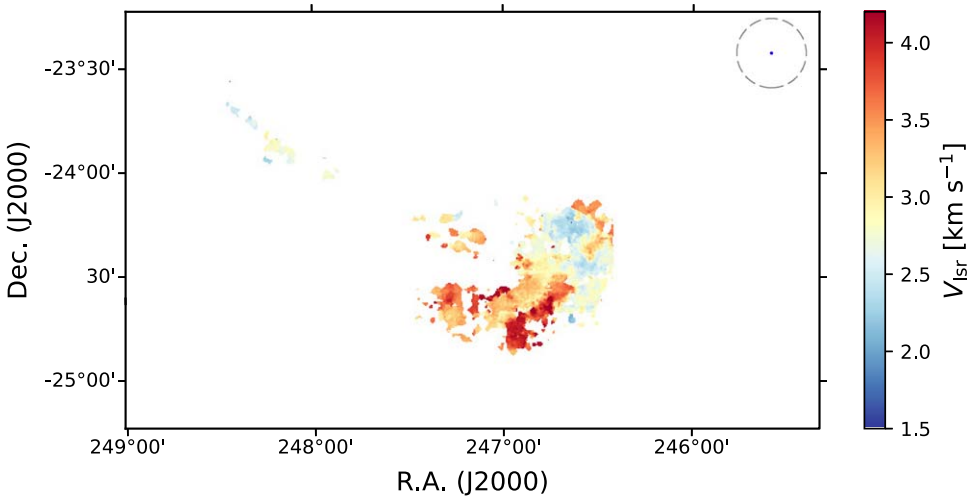

Figure B8. Same as Figure 6, but for the HCN line.

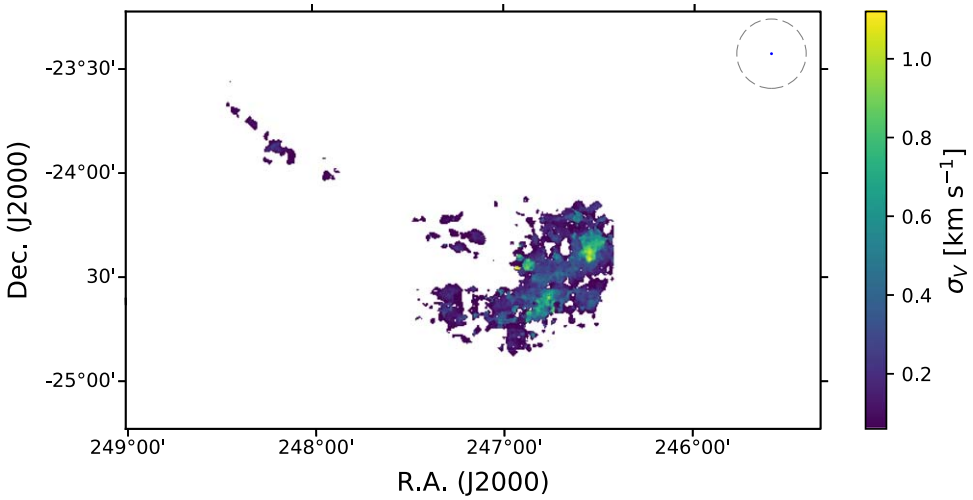

Figure B9. Same as Figure 7, but for the HCN line.

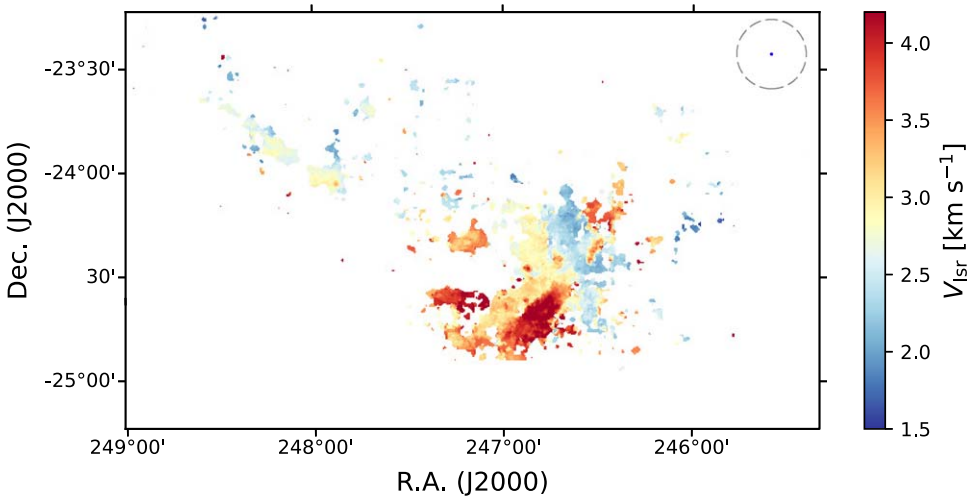

Figure B10. Same as Figure 6, but for the HCO^+ line.

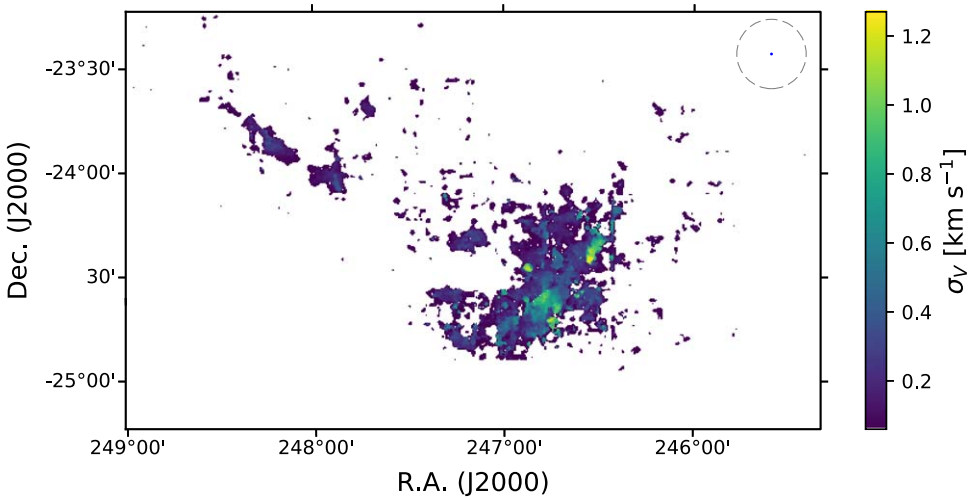

Figure B11. Same as Figure 7, but for the HCO^+ line.

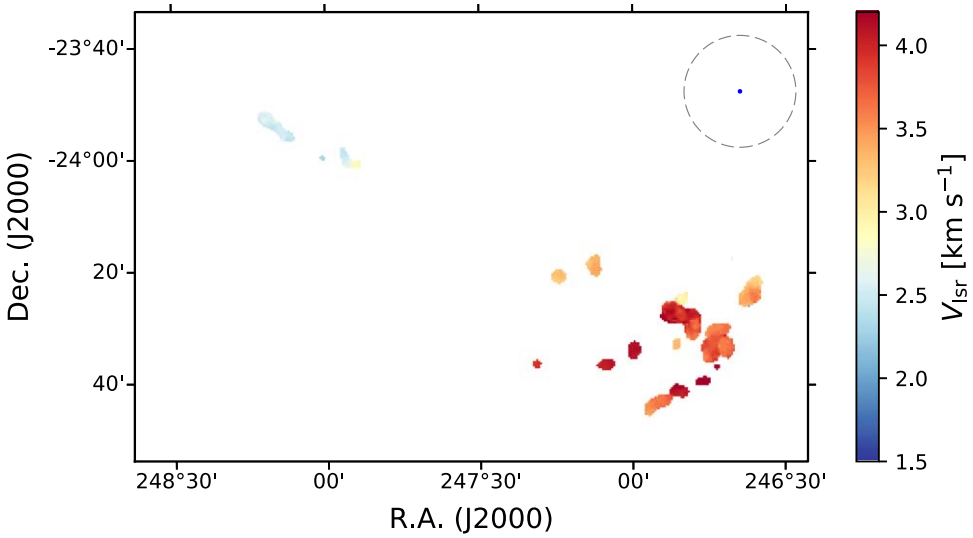

Figure B12. Same as Figure 6, but for the N_2H^+ line.

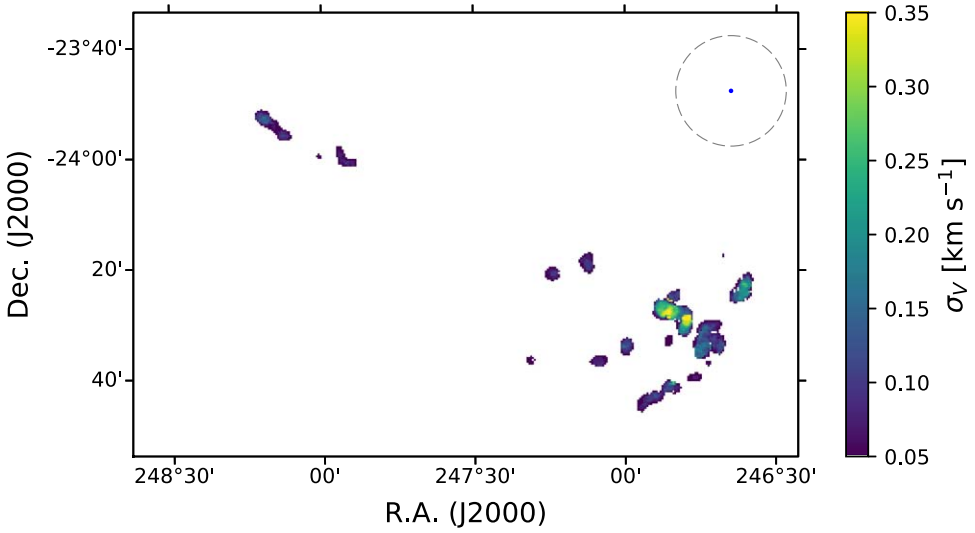

Figure B13. Same as Figure 7, but for the N_2H^+ line.

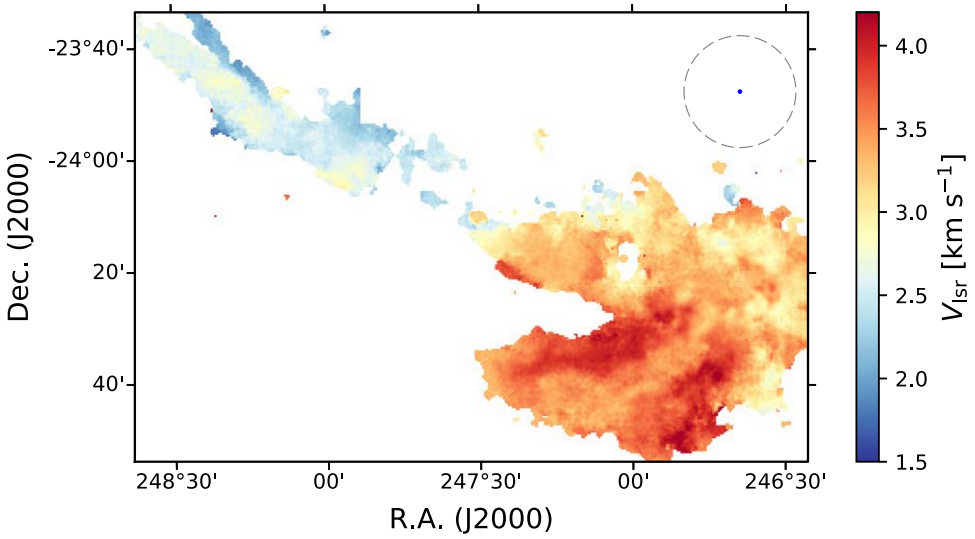

Figure B14. Same as Figure 6, but for the CS line.

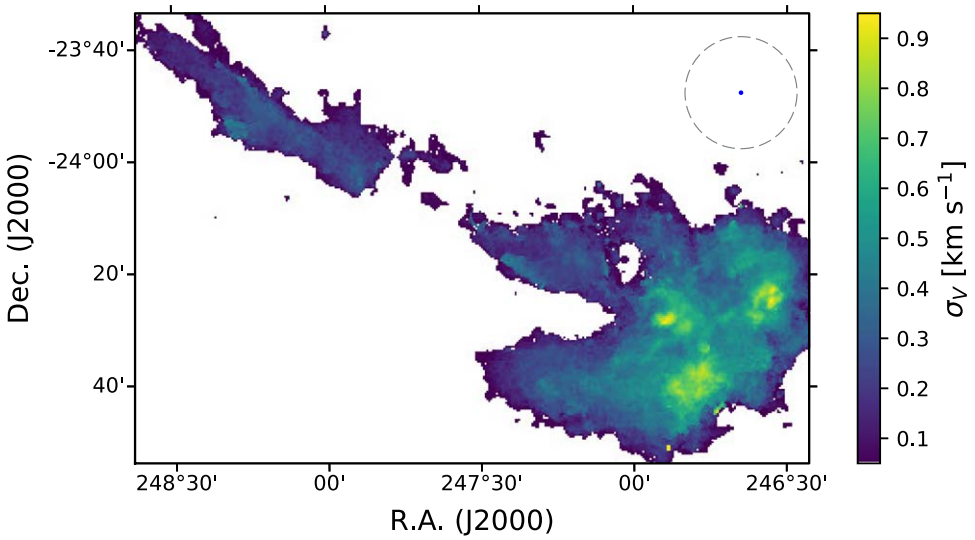

Figure B15. Same as Figure 7, but for the CS line.

Appendix C
Multiple Cloud Components along the Line of Sight in the Orion A Cloud

Figures 5 and 7 exhibit several small high-σ_V regions. There are high-σ_V regions in the ISF and L1647 of the Orion A cloud. In the Ophiuchus cloud, there is a small high-σ_V region in the northern part of L1688. In each cloud, these regions have σ_V that are higher than the typical value of σ_V in the other part of the cloud.

Figures C1 and C2 show the position–velocity (PV) diagrams for these high-σ_V regions in the Orion A cloud, and Figure C3 presents the PV diagram for the high-σ_V region in the Ophiuchus cloud. The PV diagrams demonstrate that there are two cloud components along the lines of sight at the high-σ_V regions. Thus, the high-σ_V values are caused by multiple gas components with different line-of-sight velocities. In the ISF region, the interactions between the MC and nearby sources, such as a foreground expending nebula and protostellar outflows, seem to produce these multiple cloud components (Shimajiri et al. 2014; Kong et al. 2018). In the L1647 and L1688 regions, there might be foreground or background cloud components with different line-of-sight velocities.

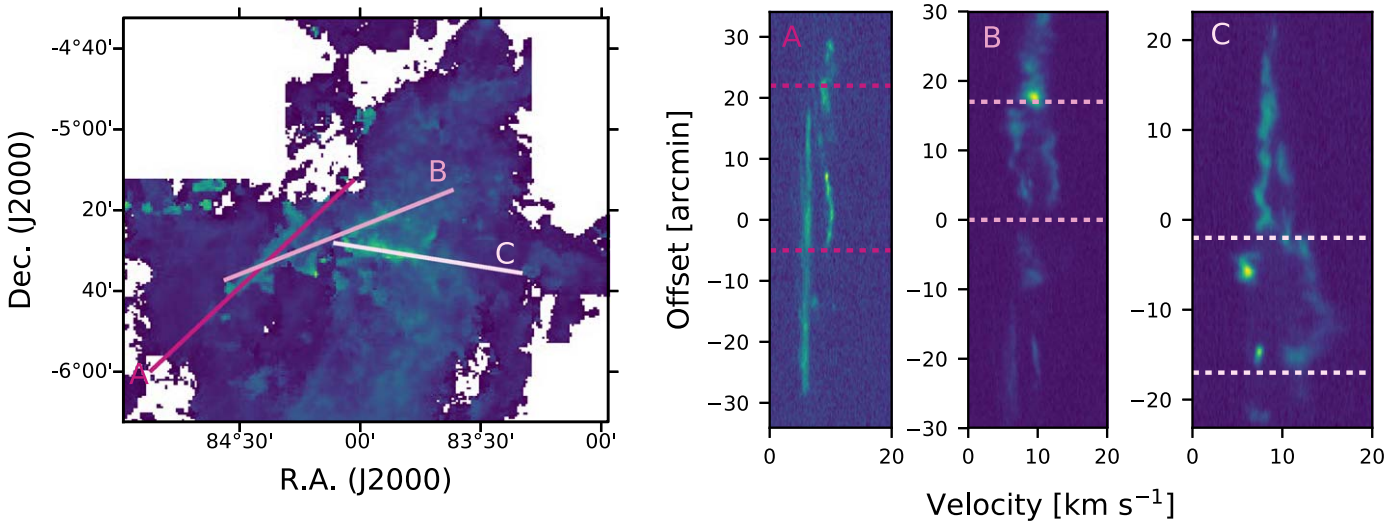

Figure C1. PV diagrams for the high-σ_V regions in the ISF. The positions where the PV diagrams are extracted are presented with the solid lines on the σ_V map of ^{13}CO (the first panel). The PV diagrams along the solid lines (A, B, and C) are presented in the second, third, and fourth panels. The dotted horizontal lines in each PV diagram represent the position of the high-σ_V regions on each line. The offset on the y-axis of the PV diagrams indicates a displacement from east to west on the line.

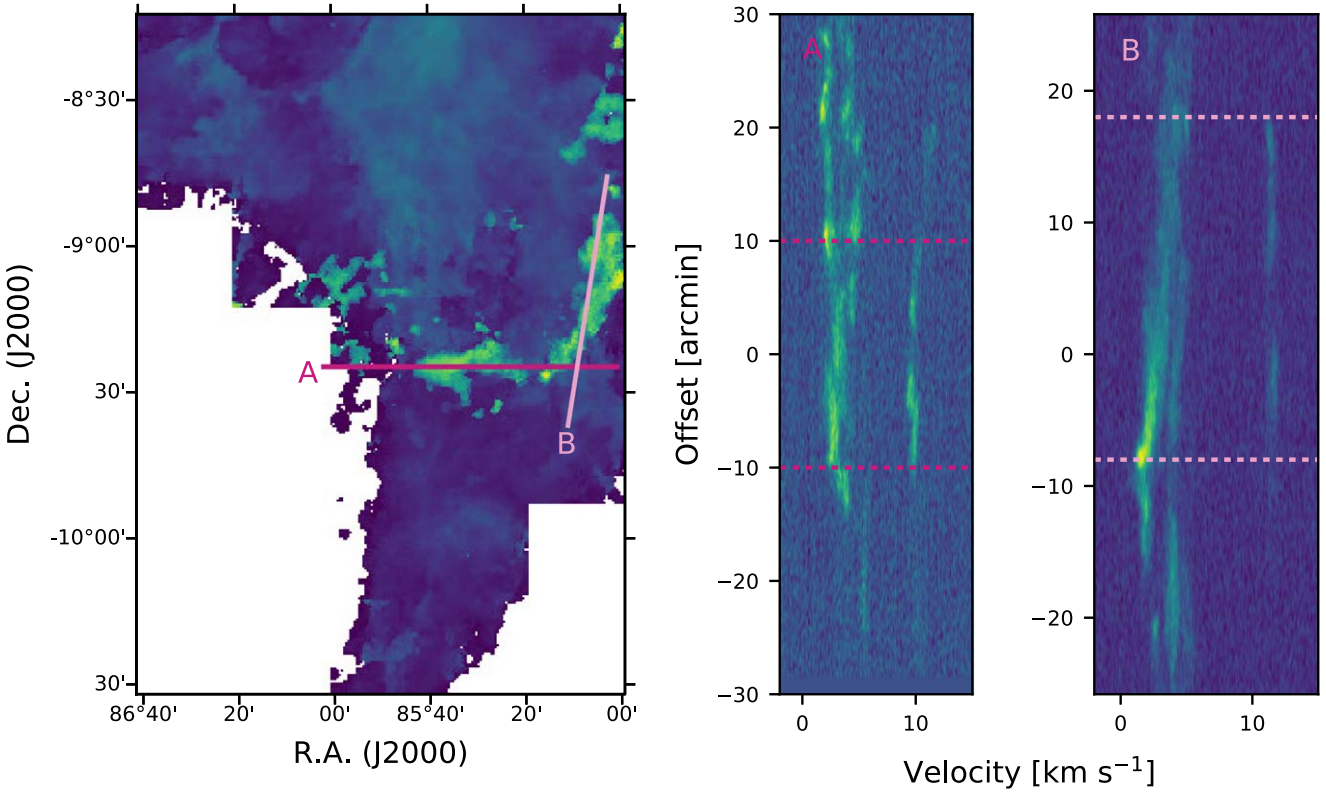

Figure C2. Same as Figure C1, but for the high-σ_V regions in L1709.

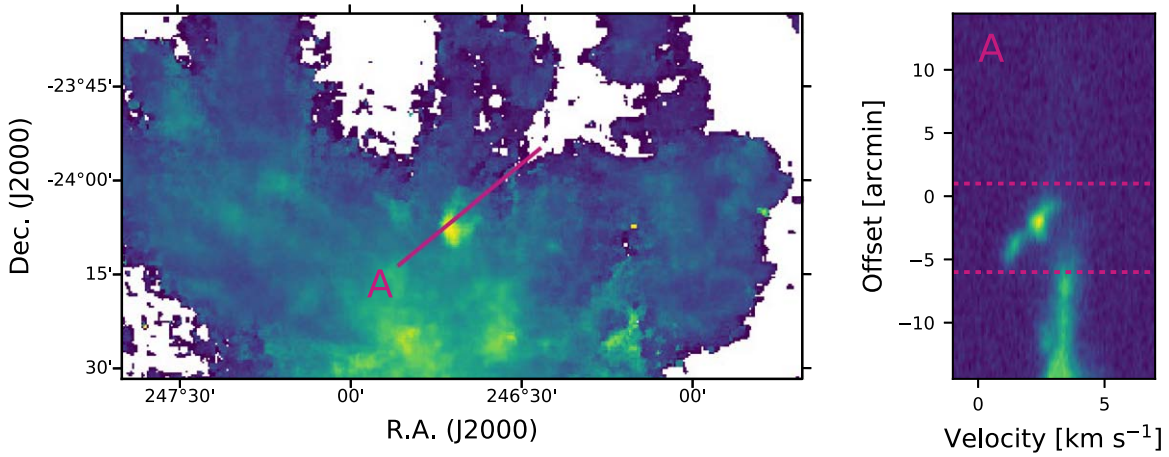

Figure C3. Same as Figure C1, but for the high-σ_V region in L1688.

Appendix D
Random Motion of the L1688 Cloud

Because the observed ^{13}CO line can be optically thick toward the dense part of L1688, the $V_{\rm lsr}$ map for ^{13}CO (Figure 6) cannot exactly present the global motion of the cloud. Therefore, the optically thinner lines, such as the C^{18}O and CS lines, should be used to trace the global motion. However, the $V_{\rm lsr}$ maps of the C^{18}O and CS lines do not present any large-scale motions of the L1688 cloud (Figures B6 and B10). Loren (1989b) also suggested that the gas motion in the L1688 cloud is more complex than simple rotation. They measured $V_{\rm lsr}$ of the Ophiuchus cores using the ^{13}CO and DCO$^+$ lines and found that the velocity variation for the DCO$^+$ lines is larger than that for the ^{13}CO lines. Therefore, we assume that there is no global motion in L1688.

ORCID iDs

Hyeong-Sik Yun https://orcid.org/0000-0001-6842-1555
Jeong-Eun Lee https://orcid.org/0000-0003-3119-2087
Yunhee Choi https://orcid.org/0000-0002-3895-6169
Neal J. Evans, II https://orcid.org/0000-0001-5175-1777
Stella S. R. Offner https://orcid.org/0000-0003-1252-9916
Mark H. Heyer https://orcid.org/0000-0002-3871-010X
Brandt A. L. Gaches https://orcid.org/0000-0003-4224-6829
Yong-Hee Lee https://orcid.org/0000-0001-6047-701X
Giseon Baek https://orcid.org/0000-0002-2814-1978
Hyunwoo Kang https://orcid.org/0000-0001-9317-7646
Seokho Lee https://orcid.org/0000-0002-0226-9295
Ken'ichi Tatematsu https://orcid.org/0000-0002-8149-8546
Yao-Lun Yang https://orcid.org/0000-0001-8227-2816
How-Huan Chen https://orcid.org/0000-0001-6222-1712
Youngung Lee https://orcid.org/0000-0003-0916-9905
Jungyeon Cho https://orcid.org/0000-0003-1725-4376

References

Aikawa, Y., Ohashi, N., Inutsuka, S.-i., Herbst, E., & Takakuwa, S. 2001, ApJ, 552, 639
Allen, L. E., & Davis, C. J. 2008, in Handbook of Star Forming Regions, Volume I: The Northern Sky, ed. B. Reipurth, Vol. 4 (San Francisco, CA: ASP), 621
André, P., Men'shchikov, A., Bontemps, S., et al. 2010, A&A, 518, L102
Bally, J., Langer, W. D., Stark, A. A., & Wilson, R. W. 1987, ApJL, 312, L45
Bergin, E. A., & Langer, W. D. 1997, ApJ, 486, 316
Bergin, E. A., & Tafalla, M. 2007, ARA&A, 45, 339
Bianchi, S. 2013, A&A, 552, A89
Brunt, C. M., & Heyer, M. H. 2013, MNRAS, 433, 117
Brunt, C. M., Heyer, M. H., & Mac Low, M. M. 2009, A&A, 504, 883
Burkhart, B., Falceta-Gonçalves, D., Kowal, G., & Lazarian, A. 2009, ApJ, 693, 250
Caselli, P., Walmsley, C. M., Tafalla, M., Dore, L., & Myers, P. C. 1999, ApJL, 523, L165
Chen, H. H.-H., Offner, S. S. R., Pineda, J. E., et al. 2020, arXiv:2006.07325
Chen, H. H.-H., Pineda, J. E., Goodman, A. A., et al. 2019, ApJ, 877, 93
Dame, T. M. 2011, arXiv:1101.1499
Davis, C. J., Froebrich, D., Stanke, T., et al. 2009, A&A, 496, 153
Dobashi, K. 2011, PASJ, 63, S1
Dunham, M. M., Allen, L. E., Evans, N. J., II, et al. 2015, ApJS, 220, 11
Elmegreen, B. G., & Scalo, J. 2004, ARA&A, 42, 211
Emerson, D. T., & Graeve, R. 1988, A&A, 190, 353
Evans, N. J., II 1999, ARA&A, 37, 311
Evans, N. J., II, Kim, K.-T., Wu, J., et al. 2020, ApJ, 894, 103
Friesen, R. K., Pineda, J. E., Rosolowsky, E., et al. 2017, ApJ, 843, 63
Furlan, E., Fischer, W. J., Ali, B., et al. 2016, ApJS, 224, 5
Gaches, B. A. L., Offner, S. S. R., Rosolowsky, E. W., & Bisbas, T. G. 2015, ApJ, 799, 235
Gill, A. G., & Henriksen, R. N. 1990, ApJL, 365, L27
Goodman, A. A., Barranco, J. A., Wilner, D. J., & Heyer, M. H. 1998, ApJ, 504, 223
Goodman, A. A., Pineda, J. E., & Schnee, S. L. 2009, ApJ, 692, 91
Großschedl, J. E., Alves, J., Meingast, S., et al. 2018, A&A, 619, A106
Hartmann, L., & Burkert, A. 2007, ApJ, 654, 988
Hasegawa, T., Kaifu, N., Inatani, J., et al. 1984, ApJ, 283, 117
Heyer, M. H., & Brunt, C. M. 2004, ApJL, 615, L45
Heyer, M. H., Morgan, J., Schloerb, F. P., Snell, R. L., & Goldsmith, P. F. 1992, ApJL, 395, L99
Heyer, M. H., & Schloerb, F. P. 1997, ApJ, 475, 173
Hildebrand, R. H. 1983, QJRAS, 24, 267
Ikeda, N., Sunada, K., & Kitamura, Y. 2007, ApJ, 665, 1194
Jeong, I.-G., Kang, H., Jung, J., et al. 2019, JKAS, 52, 227
Jiménez-Donaire, M. J., Cormier, D., Bigiel, F., et al. 2017, ApJL, 836, L29
Johansson, L. E. B., Andersson, C., Ellder, J., et al. 1984, A&A, 130, 227
Johnstone, D., Di Francesco, J., & Kirk, H. 2004, ApJL, 611, L45
Kauffmann, J., Goldsmith, P. F., Melnick, G., et al. 2017, A&A, 605, L5
Kirk, H., Friesen, R. K., Pineda, J. E., et al. 2017, ApJ, 846, 144
Klessen, R. S. 2000, ApJ, 535, 869
Koch, E. W., Ward, C. G., Offner, S., Loeppky, J. L., & Rosolowsky, E. W. 2017, MNRAS, 471, 1506
Kong, S., Arce, H. G., Feddersen, J. R., et al. 2018, ApJS, 236, 25
Kounkel, M., Covey, K., Suárez, G., et al. 2018, AJ, 156, 84
Kowal, G., Lazarian, A., & Beresnyak, A. 2007, ApJ, 658, 423
Krips, M., Neri, R., García-Burillo, S., et al. 2008, ApJ, 677, 262
Kuiper, T. B. H., Kuiper, E. N. R., Zuckerman, B., et al. 1980, in IAU Symp. 87, Interstellar Molecules, ed. B. H. Andrew (Dordrecht: D. Reidel), 31
Kutner, M. L., Tucker, K. D., Chin, G., & Thaddeus, P. 1977, ApJ, 215, 521
Lada, C. J., & Wilking, B. A. 1980, ApJ, 238, 620
Larson, R. B. 1981, MNRAS, 194, 809
Lee, J.-E., Bergin, E. A., & Evans, N. J. I. 2004, ApJ, 617, 360

Lee, J.-E., Evans, N. J. I., Shirley, Y. L., & Tatematsu, K. 2003, ApJ, 583, 789
Loren, R. B. 1989a, ApJ, 338, 902
Loren, R. B. 1989b, ApJ, 338, 925
Loren, R. B., Wootten, A., & Wilking, B. A. 1990, ApJ, 365, 269
Lynds, B. T. 1962, ApJS, 7, 1
Mac Low, M.-M., & Klessen, R. S. 2004, RvMP, 76, 125
Maddalena, R. J., Morris, M., Moscowitz, J., & Thaddeus, P. 1986, ApJ, 303, 375
Mairs, S., Johnstone, D., Kirk, H., et al. 2016, MNRAS, 461, 4022
Megeath, S. T., Gutermuth, R., Muzerolle, J., et al. 2012, AJ, 144, 192
Meingast, S., Alves, J., Mardones, D., et al. 2016, A&A, 587, A153
Méndez-Hernández, H., Ibar, E., Knudsen, K. K., et al. 2020, MNRAS, 497, 2771
Monsch, K., Pineda, J. E., Liu, H. B., et al. 2018, ApJ, 861, 77
Motte, F., Andre, P., & Neri, R. 1998, A&A, 336, 150
Nagahama, T., Mizuno, A., Ogawa, H., & Fukui, Y. 1998, AJ, 116, 336
Nakamura, F., Ishii, S., Dobashi, K., et al. 2019, PASJ, 71, S3
Nakamura, F., Miura, T., Kitamura, Y., et al. 2012, ApJ, 746, 25
Olofsson, H., Ellder, J., Hjalmarson, A., & Rydbeck, G. 1982, A&A, 113, L18
Ortiz-León, G. N., Loinard, L., Kounkel, M. A., et al. 2017, ApJ, 834, 141
Ossenkopf, V., & Mac Low, M. M. 2002, A&A, 390, 307
Padoan, P., Bally, J., Billawala, Y., Juvela, M., & Nordlund, Å. 1999, ApJ, 525, 318
Padoan, P., Juvela, M., Goodman, A. A., & Nordlund, Å. 2001, ApJ, 553, 227
Padoan, P., Juvela, M., Kritsuk, A., & Norman, M. L. 2006, ApJL, 653, L125
Padoan, P., Juvela, M., Kritsuk, A., & Norman, M. L. 2009, ApJL, 707, L153
Pan, Z., Li, D., Chang, Q., et al. 2017, ApJ, 836, 194
Pattle, K., Ward-Thompson, D., Kirk, J. M., et al. 2015, MNRAS, 450, 1094
Pety, J., Guzmán, V. V., Orkisz, J. H., et al. 2017, A&A, 599, A98
Punanova, A., Caselli, P., Pon, A., Belloche, A., & André, P. 2016, A&A, 587, A118
Ridge, N. A., Di Francesco, J., Kirk, H., et al. 2006, AJ, 131, 2921
Ripple, F., Heyer, M. H., Gutermuth, R., Snell, R. L., & Brunt, C. M. 2013, MNRAS, 431, 1296
Roh, D.-G., & Jung, J. H. 1999, PKAS, 14, 123
Roy, A., Martin, P. G., Polychroni, D., et al. 2013, ApJ, 763, 55
Rydbeck, O. E. H., Hjalmarson, A., Rydbeck, G., et al. 1981, ApJL, 243, L41
Shimajiri, Y., André, P., Braine, J., et al. 2017, A&A, 604, A74
Shimajiri, Y., Kawabe, R., Takakuwa, S., et al. 2011, PASJ, 63, 105
Shimajiri, Y., Kitamura, Y., Saito, M., et al. 2014, A&A, 564, A68
Solomon, P. M., Rivolo, A. R., Barrett, J., & Yahil, A. 1987, ApJ, 319, 730
Storm, S., Mundy, L. G., Fernández-López, M., et al. 2014, ApJ, 794, 165
Storm, S., Mundy, L. G., Lee, K. I., et al. 2016, ApJ, 830, 127
Tatematsu, K., Kandori, R., Umemoto, T., & Sekimoto, Y. 2008, PASJ, 60, 407
Tatematsu, K., Umemoto, T., Kameya, O., et al. 1993, ApJ, 404, 643
Ungerechts, H., Bergin, E. A., Goldsmith, P. F., et al. 1997, ApJ, 482, 245
van Dishoeck, E. F., Blake, G. A., Jansen, D. J., & Groesbeck, T. D. 1995, ApJ, 447, 760
Wannier, P. G., & Phillips, T. G. 1977, ApJ, 215, 796
Wilking, B. A., Gagné, M., & Allen, L. E. 2008, in Handbook of Star Forming Regions, Volume II: The Southern Sky, ed. B. Reipurth (San Francisco, CA: ASP), 351
Wilson, T. L., & Rood, R. 1994, ARA&A, 32, 191
Yun, H.-S., Lee, J.-E., Evans, N. J., II, et al. 2021, ApJ, in press, arXiv:2107.13323
Zhang, M., & Wang, H. 2009, AJ, 138, 1830